ANALYSIS AND IMPLEMENTATION OF A BIDIRECTIONAL DC-DC CONVERTER WITH COUPLED INDUCTOR FOR AN ELECTRIC VEHICLE POWERTRAIN

Catalina González Castaño

UNIVERSITAT ROVIRA I VIRGILI

Analysis and implementation of a bidirectional dc-dc converter with coupled inductor for an electric vehicle powertrain

Catalina González Castaño

Department of Electronics, Electric and Automatic Engineering
Tarragona, Spain
2019

UNIVERSITAT ROVIRA I VIRGILI
ANALYSIS AND IMPLEMENTATION OF A BIDIRECTIONAL DC-DC CONVERTER WITH COUPLED INDUCTOR FOR AN ELECTRIC VEHICLE POWERTRAIN
Catalina González Castaño

UNIVERSITAT ROVIRA I VIRGILI
ANALYSIS AND IMPLEMENTATION OF A BIDIRECTIONAL DC-DC CONVERTER WITH COUPLED INDUCTOR FOR AN ELECTRIC VEHICLE POWERTRAIN
Catalina González Castaño

UNIVERSITAT ROVIRA I VIRGILI
ANALYSIS AND IMPLEMENTATION OF A BIDIRECTIONAL DC-DC CONVERTER WITH COUPLED INDUCTOR FOR AN ELECTRIC VEHICLE POWERTRAIN
Catalina González Castaño

Analysis and implementation of a bidirectional dc-dc converter with coupled inductor for an electric vehicle powertrain

Catalina González Castaño

Doctoral Thesis

Supervised by
Ph.D. Enric Vidal and Ph.D. Javier Calvente

Research group:
Group of automatic control and indutrial electronic

Universitat Rovira i Virgili
Department of Electronics, Electric and Automatic Engineering
Tarragona, Spain
2019

UNIVERSITAT ROVIRA I VIRGILI
ANALYSIS AND IMPLEMENTATION OF A BIDIRECTIONAL DC-DC CONVERTER WITH COUPLED INDUCTOR FOR AN ELECTRIC VEHICLE POWERTRAIN
Catalina González Castaño

UNIVERSITAT ROVIRA i VIRGILI

FAIG CONSTAR que aquest treball, titulat "Analysis and implementation of a bidirectional dc-dc converter with coupled inductor for an electric vehicle powertrain", que presenta Catalina González Castaño per a l'obtenció del títol de Doctor, ha estat realitzat sota la meva direcció al Departament d'Enginyeria Electrònica, Elèctrica i Automàtica d'aquesta universitat.

HAGO CONSTAR que el presente trabajo, titulado "Analysis and implementation of a bidirectional dc-dc converter with coupled inductor for an electric vehicle powertrain", que presenta Catalina González Castaño para la obtención del título de Doctor, ha sido realizado bajo mi dirección en el Departamento de Ingeniería Eléctrica, Electrónica y Automática de esta universidad.

I STATE that the present study, entitled "Analysis and implementation of a bidirectional dc-dc converter with coupled inductor for an electric vehicle powertrain", presented by Catalina González for the award of the degree of Doctor, has been carried out under my supervision at the Department of Electronics, Electric and Automatic Engineering of this university.

Tarragona, April 26th 2019

El/s director/s de la tesi doctoral
El/los director/es de la tesis doctoral
Doctoral Thesis Supervisor/s

Enric Vidal Idiarte, PhD

Javier Calvente, PhD

Acknowledgment

Through my work I've experienced the most variated interactions with many different sort of people, most of them good people whom had helped me in different ways. It's because of that, mainly, that I'd like to thank those whom had been the most influential in myself -as well as those whom I ca'n't recall at the moment. My parents, Jaime González and Gloria Castaño, for obvious reasons and those that may not be that obvious. They've helped me a in large range of ways, they deserve to be acknowledged in the first place. My parents among with my siblings -Juliana and Santiago- have been next to me for pretty much my entire life. Thank you for supporting me and stand me as well.

My thesis tutors, Professor Dr. Enric Vidal and Professor Dr. Javier Calvente for guiding me in my learning journey. This research had'n't been the same without your wise help and your opportune corrections. Professor Dr. Samir Kouro, head for my Doctoral Stay, for allowing me to keep going with my research as well as experiencing a rich environment for the same. Professor Dr. Roberto Giral whom helped me big time with my thesis. A big thank you goes to Professor Dr. Carlos Restrepo for taking the time -sometimes more time than I actually asked for- to read and fix some of the flaws on my work, I've learned lots out of your guidance. The GAEI group, for their support and collaboration. Especially thanks to Josep Guasch for being the photographer, Juan Miguel Salmerón, Albert Teixidó, Joseph Ma. Bosque, Sylvia Méndez and Reham Haroun for guiding me in the laboratory.

On the other hand my new family Nicole, Kiara and Bianca. My Stay in Chile woul'n't have been the same without you. Also Juan David and Blanca, my new friends for most of the time.

To Amelia

UNIVERSITAT ROVIRA I VIRGILI
ANALYSIS AND IMPLEMENTATION OF A BIDIRECTIONAL DC-DC CONVERTER WITH COUPLED INDUCTOR FOR AN ELECTRIC VEHICLE POWERTRAIN
Catalina González Castaño

Abstract

The electric vehicles powertrain configuration have a common system that is formed by the battery, the power converter and the electric motor. Each one of these components has been the subject of an extensive research in recent years and a high level of development, with the aim of improving the performance of the automotive traction systems. However, these three components represent a great research challenge given the complexity of the integration of these elements in electric vehicles application. There are two basic configurations to implement the power converter in electric vehicles powertrain: first, the power converter is directly connected to the battery and, second configuration uses a bidirectional dc-dc converter between the battery pack and the traction inverter. In the literature the most commonly used converter for this application has been based on the bidirectional dc-dc boost converter. Nevertheless, design of electric vehicles powertrain based in boost converter is challenging because electric vehicle applications require efficiency optimization in a wide range of speeds instead of optimizing efficiency at the maximum power of the inverter traction.

In this work the noninverting bidirectional buck-boost converter is proposed to regulate the dc voltage in an electric vehicle powertrain. The converter is based on the versatile buck-boost converter, which has been used as a building block in several fuel-cell applications, it has shown a great performance in low voltage and hard-switching applications. Two bidirectional noninverting buck-boost converter prototypes are presented, with an input voltage range of 200 V to 400 V, output voltage between 100 V and 400 V and 1.6 kW rated power. They validate that the pair of coupled inductors of the power stage that operates with the higher efficiency has the proposed coils arrangement that uses only one toroidal core, with a very low parasitic winding-to-winding capacitance and loose magnetic coupling. Adapting the power stage damping network to the new parameters of the loosely coupled inductors is straightforward.

To regulate the ouput voltage of the converter, a two-loop is programmed controller using the digital signal controller TMS320F28377S. Two different inner current programmed controllers were proposed which corresponds to a discrete-time sliding-mode current control and a multisampled average current control. A hardware emulation system is used to taste the strategy control under realistic operation which imitates the actual vehicle dynamics for city driving conditions.

Keywords

Noninverting buck-boost converter, high efficiency, wide bandwidth control, discrete-time sliding-mode current control (DSMCC), multisampled average current control (MACC), electric vehicle (EV), coupled inductor.

UNIVERSITAT ROVIRA I VIRGILI
ANALYSIS AND IMPLEMENTATION OF A BIDIRECTIONAL DC-DC CONVERTER WITH COUPLED INDUCTOR FOR AN ELECTRIC VEHICLE POWERTRAIN
Catalina González Castaño

Contents

List of Figures

List of Tables

Acronyms and shorthand notations

Term	Description
DSMCC	Discrete-time sliding-mode current control
MACC	Multisampled average current control
EV	Electric vehicle
FCs	Full cells
SCs	Supercapacitors
SAZZ	Snubber-assisted zero-voltage transition/zero-current transition
DCX	DC transformer
TLC	Three level converter
BIC	Bidirectional buck-boost converter
CBC	Two-level buck-boost converter
GHG	Global greenhouse gas
ICE	Internal combustion engine
HEVs	Hybrid electric vehicles
PHEVs	Plug-in hybrid electric vehicles
EM	Electric motor
SoC	low state of charge
IM	Induction machine
DPWM	Digital controlled pulse width modulation
MI	Modulation index
QIP	Quantization-induced perturbations
ePWM	Enhanced pulse width modulator
DSC	Digital signal control
ZCS	Zero-current-switching
CCM	Continuous conduction mode
SSA	State space averaging
2D-FEM	2-dimensional finite element method
PS1	Power stage 1
PS2	Power stage 2
SW	Ideal switch
CF	Crossover frequency
PM	Phase margin

SR	Slew rate
PMSMs	Permanent-magnet synchronous motors
LCO	Limit-cycle oscillations
SIC	Silicon carbide

1 Introduction

In the field of automobile industry, the general concept of Electric Vehicle (EV) refers to an electric drive vehicle that uses batteries, fuel cells (FCs), and supercapacitors (SCs) or combinations between the past mentioned to convert from electric to mechanical energy. In most cases automobile manufacturers use a high-voltage dc bus to deliver power to the motor [2]. The mentioned energy sources can be connected in many ways for EV powertrain configurations. The basic connection consists of directly connect two sources (FC/battery, FC/SC, or battery/SC) to the inverter drive. In general, the energy consumption of the powertrain cannot be controlled through the sources, but the power requirements can be determined by the parameters such as temperature of the motor, states of charge of the battery, and the operating point of the whole system [3]. Therefore, if the sources do not have any control over the powertrain consumption, then the inverter drive connected to the high-voltage dc bus could provide negative impacts on the inverter and motor's performance. For this reason, a dc-dc converter can be connected between the sources and the inverter drive to regulate its output voltage archiving a better operation performance [4]. The dc-dc converter ensures the energy management between the sources and the inverter drive through a dc bus voltage regulation which results in high power conversion efficiency of the whole system [5].

The design of the dc-dc converter depends on the characteristic of the powertrain system, principally on the power requirements system. The principal function of converter in EV application is to direction the power delivered by the source devices. Indeed, the conversion stage is important to improve the performance of the powertrain [6].

A bidirectional dc-dc converter allows power flow in both directions, reason why it is useful in regenerative braking operation. Most of the conventional converter topologies can be made bidirectional. Therefore, many studies have been investigating dc-dc converter topologies in powertrain applications. There are EV applications using a conventional boost converter topology [7–9]. This topology is modified to increase the boost converter efficiency in powertrain applications, achieving methods to reduce switching loss via soft switching, like the snubber-assisted zero-voltage transition/zero-current transition (SAZZ) approach, and a dc-dc boost composite converter architecture, which is composed by three modules: buck, boost and DC transformer (DCX) [10, 11]. In [12] a boost converter with output filter is studied to reduce the EMI level. In virtue of the above, the reduction of the EMI is important in the operation of the energy sources for EV applications. Other works propose to minimize

the switching loss of the parasitic capacitance MOSFETs for hard switching using a three level converter (TLC), where the voltage applied across the switch is half of the output voltage, and TLC is compared with interleaved a bidirectional buck-boost converter(BIC), and a two-level buck-boost converter (CBC) [13]. In boost converter topologies, with soft switching, losses are high due to copper losses in the inductor. To reduce the inductance value and improve the efficiency, the operation of the four-level dc-dc converter at three discrete voltage ratios is studied in [14].

1.1 Motivation and problem statement

The global warming and climate change are the result of human activities, mainly due to emissions of carbon dioxide (CO_2) from fossil fuel combustion in several sectors which include electricity generation, transportation, agriculture, and commercial and residential activities [15]. However, the reduction of the road transport carbon emissions is considered currently one of the biggest challenges of our society and the situation could worsen in the future if immediate and decisive actions are not taken. The transportation sector is responsible for 24% of global greenhouse gas (GHG) emissions and in a large extent also blameable for the air quality degradation which threatens population's health and the oil dependence [16]. Additionally the population is growing, especially in developing countries, therefore the required energy needs will increase and so will the oil prices. Compounding the oil situation, the large reserves are in politically unstable countries and this may worsen the situation even more. With this background, it is understandable that the great powers are making large investments to search for transport alternatives to internal combustion engine (ICE) vehicles [17].

Against this background, different efforts are being undertaken to reduce the GHG emissions and to improve the performance of the transportation sector, by means of the development of new fuels and the electrification of transport [18]. The latter is a promising approach with potential benefits in improving the energy security by the diversification of the energy sources, fostering economic growth by creating new advanced industries focused on the Electric Vehicles (EVs) and most importantly, its technology is environment friendly which allows the integration of renewable energy into the power system [18, 19]. Nowadays, commercial EVs can be categorized into three types based on the vehicle hybridization ratio, which are hybrid electric vehicles (HEVs), plug-in hybrid electric vehicles (PHEVs) and battery electric vehicles (BEVs) [18] as shown in Figure **1-1**. The HEVs and PHEVs are driven through a combination of an ICE and an electric motor (EM) but the small HEV's battery can only be charged by the ICE or the regenerative braking. There are different powertrain configurations (series, parallel and series-parallel) developed for HEVs and PHEVs in order to achieve different objectives such as improve fuel economy, increase power and minimize cost [18].

All the EVs power train configuration shown in Figure **1-1** have a common system that

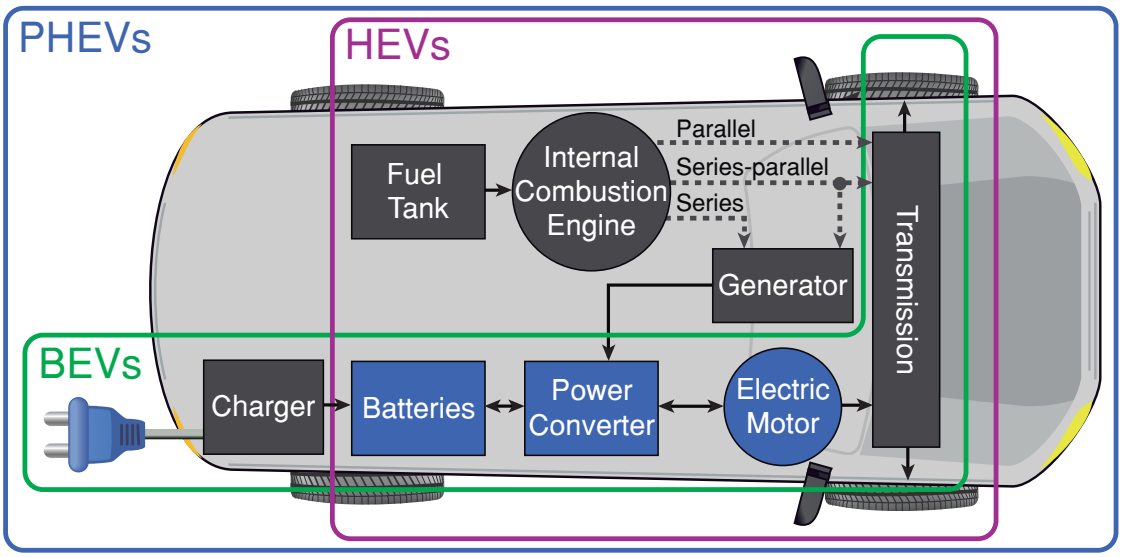

Figure **1-1**: EVs powertrain configurations.

is formed by the battery, the power converter and the electric motor. Each one of these components has been the subject of an extensive research in recent years and a high level of development, with the aim of improving the performance of the automotive traction systems. However, these three components represent a great research challenge given the complexity of the integration of these elements in EVs application, as it is summarized below:

- *Battery system*: In the case of EVs, the battery is generally sized by the energy requirements to allow a certain range to be reached, but there is not a linear relationship between car range and battery capacity, due the fact that adding the weight of the battery reduces the efficiency on the road [19, 20]. Advantages such as a high energy density, high efficiency, long lifespan and high potential to improve, make the lithium-ion batteries the most promising storage technology for the near EVs future [20]. The battery cells for EVs are usually connected in series to meet the voltage requirements of the power converter (inverter). However, during the normal battery system operation multiple charges and discharges are made. This produces voltage imbalance between the cells due its difference in leakage currents and chemical characteristics, which causes progressive damage and a reduction of its lifespan [21, 22]. In addition, the connection of cells in series exponentially increases the probability of failure of the battery pack. The performance of the whole pack is limited by the weakest cell thus implying an oversizing of the power inverter and the electric motor in order to ensure peak power delivery at low state of charge (SoC) of a battery pack with a wide voltage variation at different SoC [23, 24]. Also there is a limitation of the maximum number of battery cells that could be connected in series and a step-up dc-dc power converter is required to reach the requirements of the inverter converter. Therefore,

the power converter shown in Figure **1-1** should be formed by a dc-dc power converter (with a step-up characteristic) in cascade with a dc-ac traction inverter to solve the aforementioned problems [21].

- *Electric motor*: Considering the development and the applications of different traction motors available in commercial EVs, the induction machine (IM) and the permanent magnet synchronous machine (PMSM) are the most used [25,26]. All these machines in the EV applications have been designed to exhibit torque/power-speed characteristics as shown in Figure **1-2** [25]. This characteristic represents a demanding challenge both for industry and research on EV motors and drive systems. Figure **1-2** shows three different regions, the first one corresponds to the constant torque operation, where the maximum torque capability is determined by the current rating of the inverter [25, 27]. In this region, the maximum torque at base speed (point A in Figure **1-2**) determines the vehicle performance at starting or climbing hills [26]. The second region corresponds to the constant power operation which guarantees not to exceed the maximum current or voltage limits in the inverter [25]. In this region the available torque at maximum speed (point B in Figure **1-2**) limits the vehicle speed at the highways. In the third region, the torque and power reduce due to the increasing influence of the back-electromotive force [25,27]. Thus, the motor dynamic is governed by the input voltage and current of the inverter, but if the inverter is directly connected to a battery its input voltage will be variable and not controlled. In addition, with a dc-dc converter between the battery and the inverter, the dc voltage in the inverter input could be optimized based on the loading conditions in order to maximize the electric motor efficiency [28]. With this dc-dc power converter, the power capability and the maximum speed can be improved without sacrificing the low-speed torque capability [26].

- *Power converter*: The power converter represents an important share of the total cost of the EVs and it has a high potential for cost reduction [20]. However, this important component of EVs is less covered in literature on electric vehicles applications [20]. Two basic configurations are used to implement the power converter in Figure **1-1**. The first one corresponds to a power inverter directly connected to the battery system and the second configuration uses a bidirectional dc-dc converter between the battery pack and the traction inverter. In the case of the first configuration, the inverter does not have the same performance at all modulation index (MI) and it is more efficient and produces better waveforms at higher MI values. Therefore, for values below the base speed the inverter MI is less than 1 and the phase voltage of the motor is increased proportionally to the speed as shown in Figure **1-2** (see dc-ac block) and the inverter is operating in low efficiency zones. Once the base speed is reached, the phase voltage remains constant at the rated phase voltage by means of a $MI = 1$ with an efficient operation of the inverter [29]. With the goal of extending this efficient

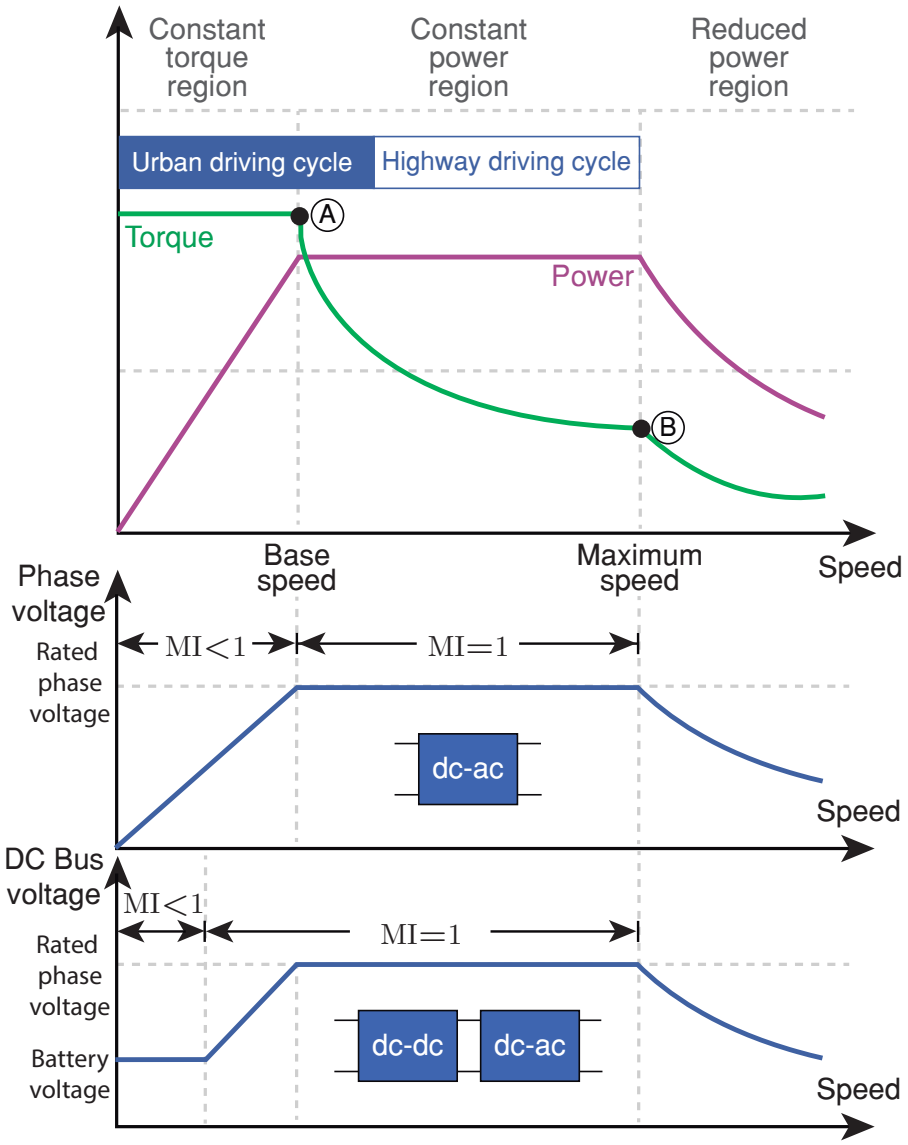

Figure **1-2**: Torque and power requirements for the EV drive systems.

inverter operation, a bidirectional dc-dc converter, typically a boost converter, is used to control the voltage at the input of the inverter according with the motor speed and optimize the efficiency of the inverter ($MI = 1$) in a wider rage of operating speeds as can be seen in Figure **1-2** (see dc-dc + dc-ac block). Nevertheless, the inverter efficiency can not be guaranteed under low speeds since the boost converter can not reduce the dc bus voltage below the battery voltage as shown in Figure **1-2** [29].

From the point of view of the battery the motor and the traction inverter, and from the previous discussion, the importance of including a bidirectional dc-dc converter in the EV powertrain is evident. In the literature, the most commonly used converter for this applica-

tion has been the based on the bidirectional dc-dc boost converter [7,11,14,30–32]. Therefore, these traction electric drive topologies are more suitable for highway driving cycle (see Figure **1-2**) reason why the efficiency system under an urban driving cycle is lower [21]. After an extensive literature review, it is concluded that bidirectional step-up/step-down dc-dc converters in the EV context are most commonly used for other applications as vehicle-to-grid (V2G) [33], battery charger [34], integrate two or more storage devices [35–37], among other.

The advantages of a dc-dc converter to adjust the dc-link voltage were presented in [6]. Where measurements of the traction motor and the inverter efficiency were realized while varying the dc-link voltage in the powertrain, the measurements show efficiency performance for some dc-link voltage. Therefore, a bidirectional dc-dc converter with wide voltage conversion range is required to get a wide conversion power for different operating points of the EV drive. Topologies with a wide voltage conversion range in a buck-boost bidirectional dc-dc converter for high voltage, hard switching and keeping high efficiency are difficult to obtain. Recently, a buck-boost converter with coupled inductor has been widely studied for charge and discharge backup batteries in space, fuel cell, photovoltaic and telecom power systems applications [1,38–40]. However, the design of a buck-boost converter with coupled inductor for powertrain application achieving a suitable efficiency system under an urban driving cycle is still an open issue.

This thesis presents the design and implementation of a bidirectional buck-boost converter with coupled inductor for regulating the voltage in a dc-link bus of an EV. This converter has been previously studied in [1,39] for low voltage applications and hard-switching applications. The selected topology has many advantages such as a noninverting voltage step–up and step–down characteristic, high efficiency, wide bandwidth [1], and the regulation of input or output currents because of their low ripple values [41]. All these features can be extended for an application at higher voltage converter with a bidirectional power flow control and this is the main goal of this work.

1.2 Objectives

1.2.1 General objective

Design a buck-boost dc-dc converter with coupled inductor prototype for an EV powertrain application.

1.2.2 Specific objectives

- Design and simulate a bidirectional noninverting buck-boost converter with coupled inductor suitable for EV application, in order to achieve overall efficiency measurements with a wide voltage conversion range.

- Analyze and design of digital control approaches for the dc-dc converter able to regulate the output voltage.

- Implement a dc-dc converter prototype to verify the design and control strategies by experimental results.

- Verify the converter performance connected to a PMSM motor emulating an EV powertrain.

1.3 Contributions of this thesis

This thesis was done with the aim of designing a bidirectional noninvertig buck-boost converter for EVs powertrain configuration, Therefore the following main contributions on this field are:

- A novel high-voltage bidirectional converter with a step-up and step-down characteristic to extend the EV traction inverter efficiency under a wide range of speeds. This converter guarantees a high power conversion efficiency due to the use of silicon carbide (SiC) devices and the design with a low winding-to-winding parasitic capacitance of the coupled inductor. It can operate in boost or buck mode.

- A design rule implementation of the coupled inductors for high-voltage applications in order to achieve a very low-winding-to-winding parasitic capacitance and, consequently, improving the efficiency of the system. The pair of coupled inductors of the bidirectional buck-boost converter uses only one toroidal core, with a very low parasitic winding-to-winding capacitance and loose magnetic coupling.

- A fair comparison between two different digital current programmed controllers, sliding-mode current control (DSMCC) and multisampled average current control (MACC), which corresponds to the inner current control loop of the voltage feedback outer loop. These digital controllers included a dead zone avoidance technique that effectively suppressed undesirable non-linear phenomena in the buck-boost mode transitions such as subharmonics or other undesirable nonlinear phenomen.

- The design of two nested control loops with a current (inner loop) controller and a voltage (outer loop) controller that allow to regulate the dc bus during motoring and regeneration (regenerative brake) conditions. Each of the proposed controllers ensure fast tracking of the control set-points and low steady state error under demanding tests that include system start-up, dc bus voltage reference with small and large variations.

- A hardware emulation system is used to test the proposed bidirectional converter and its digital control under realistic operation which imitates the actual vehicle dynamics for city driving conditions.

Also, this work achieved other additional contributions on related topics, which are not among the main topics but still important in the field of digital control in dc-dc converters.

- A novel simple scheme alternative to the conventional scheme to compute the voltage error without any additional hardware is introduced to achieve significantly improved dynamic responses, reduce the quantization-induced perturbations, and increase the voltage loop bandwidth with a similar phase margin in a two-loop control to regulate output voltage in a dc-dc buck-boost converter with a MACC inner loop and using a low-resolution pulse width modulation (PWM).

1.4 Manuscript organization

The manuscript is composed by five main chapters, which are organized as follows:

Chapter 2 presents the bidirectional noninvergting buck-boost converter for the EVs powertrain application. Two different power-stages have been built. The first power stage is based on the versatile buck-boost converter, which in low voltage and hard-switching applications has presented many advantages in different topologies of fuel cell hybrid and photovoltaic systems. Nevertheless, for this application low efficiency is demonstrated. Therefore, the second power stage is built with a design modification of the coupled inductor, carrying on the use of the converter to higher voltage applications with high efficiency.

In chapter 3, the digitally bidirectional buck-boost converter is presented, aimed to regulate the dc bus during motoring and regeneration (regenerative brake) conditions. Here the MACC and DSMCC inner loop are compared.

In chapter 4, the description of the undesired quantization-induced perturbations (QIP) in a voltage regulated dc-dc buck-boost converter using a two-loop digital control is presented. Also a simple method to reduce the QIP is introduced.

In chapter 5, the conclusions and future work are presented.

2 Design of a bidirectional dc-dc converter with coupled inductor for EV application

2.1 Abstract

This chapter proposes a bidirectional noninverting buck-boost converter for EV application design. A first power stage design is based on hard-switching low-voltage versions of the also known as the versatile buck-boost converter, which have presented many advantages in different configurations of photovoltaic and fuel cell hybrid systems. Therefore, carrying on the use of the converter to higher voltage applications, a second power stage is developed with a design modification of the coupled inductors that adapts the converter for high voltage applications. High efficiency experimental results from a 400 V 1.6 kW prototype have been achieved over a wide operating voltage range, thanks to the use of SiC devices and the design with low winding-to-winding parasitic capacitance of the coupled inductors, confirming in this way its good potential as a buildick block also in high-voltage wide-gain-range applications.

2.2 Introduction

The noninverting dc-dc buck-boost converter with coupled inductors [1] could be a good candidate to optimize global efficiency for EV applications because it is able to step-up or step-down voltage with high efficiency with smooth transitions between both modes provided that a histeretic PWM control strategy is used to activate its switches [42]. This converter has the same wide conversion ratio than a single inductor noninverting buck-boost converter with better efficiency because of reduced switches stress, in addition, the placement of their coupled inductors eliminate the pulsating nature of input and output currents and reduce the associated noise levels. Moreover, the combination of coupled inductors with an RC damping network in parallel with the intermediate capacitor eliminates the right-half-plane (RHP) zero usually exhibited by conventional continuous conduction dc-dc converters in step-up voltage mode [1]. The topology has been used as a building block in several fuel-cell applications such as the serial-paralell hybrid system reported in [40]. An even more versatile

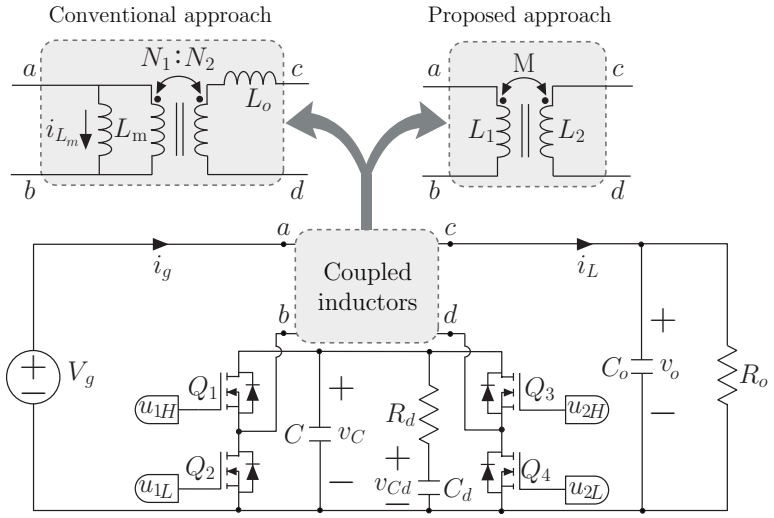

Figure **2-1**: Structure of the bidirectional noninverting buck-boost converter.

bidirectional version was introduced in [39, 43] where digital and analog controls have been studied for low voltage applications.

The coupled inductors for the conventional approach power stage can be designed following the transformer model shown at the top left of Figure **2-1**, where L_m is the magnetized inductance, L_o is the leakage inductance, and the coupled coefficient k is determined by $k = L_m/\sqrt{L_m(L_o + L_m)}$ [38]. In [1] a coupled inductor with a ratio turns $N1/N2 = 1$ and $k = 0.5$ was built. This topology and its parameter values allow transfer functions of the system to be identical for both operation modes (buck and boost mode). Accordingly, the dynamic characteristics of the output voltage and output current are continuous between the boost and buck modes. Coupled inductors can be defined and constructed in different ways. In the photovoltaic application reported in [44] the coupling coefficient is defined as $k = M/\sqrt{L_1 L_2}$, M is the mutual inductance, and L_1 and L_2 are the self inductance values for the primary and the secondary coils of the coupled inductors, respectively. In both [44] and [39], a 1:1 transformer was constructed with a pair of tightly coupled inductors of turns ratio $N1/N2 = 1$ with a magnetizing inductance L_m, and two identical non-coupled inductors $L_a = L_b = L$ were connected in series with the primary and the secondary of the transformer, where $L_m = M$, $L_1 = L_a + M$ and $L_2 = L_b + M$, and therefore $L_1 = L_2$. The unusual symmetrical arrangement of three different magnetic elements was the form of mimicking two loosely coupled inductors with equal number of turns coiled around a single core such as the proposed approach at the top right of Figure **2-1**. It is composed of a pair of loosely coupled inductors with unitary turns ratio and magnetic coupling coefficient $k = 0.5$. Therefore, primary self-inductance L_1 is equal to secondary self-inductance L_2 ($L_1 = L_2 = L$), and their mutual inductance is $M = L/2$.

In this chapter, the design of two different power stage are detailed using the topologies depicted in Figure. **2-1** for EVs powertrain application. Then the coupled inductor design

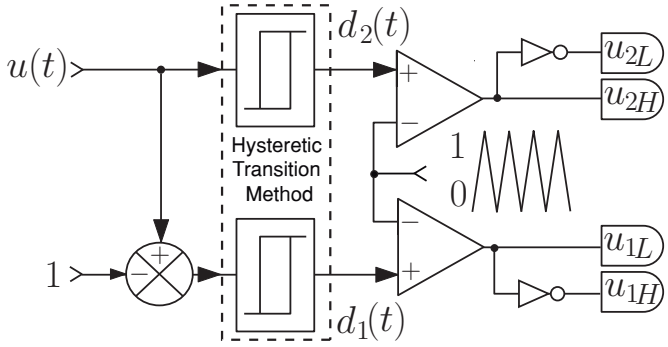

Figure **2-2**: Diagram of switch signals generation.

for each approach is presented, modification of its parameters and design are realized in order to obtain the same advantages of the noninverting buck-boot studied for low voltage applications.

2.3 Buck-boost cell operation

The bidirectional noninverting buck-boost converter in Figure **2-1** is composed by a buck-boost cell, which is made up of two half bridge MOSFET, an R_dC_d damping network connected in parallel with the intermediate capacitor C, and a coupled inductor connected at the input and the output of the converter. In the scheme of Figure **2-2**, the duty cycle $d_1(t)$ is used to activate the switch Q_1 and Q_2 for boost mode. Q_3 and Q_4 are switched with the duty cycle $d_2(t)$ for buck mode. Activation signals u_{1H} and u_{1L} are activated in complementary manner while u_{2H} is set at 1 and u_{2L} is set at 0, in boost mode. Otherwise, u_{2H} and u_{2L} are activated in complementary manner while u_{1H} is set at 1 and u_{1L} is set at 0, in buck mode. The duty cycles are computed considering a variable control $u(t)$, where $u(t) = 1 + d_1(t)$ in boost mode and $u(t) = d_2(t)$ for buck mode [1]. In addition, the digital controller allows a simple incorporation of the operational dead-zone avoidance technique [42] as shown in the switch signals generation of Figure **2-2**.

2.3.1 Computing duty cycles

The method utilized in this work is a hysteretic buck-boost transition method, introduced in [42], in order to get a smooth transition between modes and adequate duty cycles values according to the operating point. This method has been employed to mitigate present phenomenons during the buck-boost mode operation, the variable $u \in [0, 2]$ is associated with the duty cycles $d_1(t)$ and $d_2(t)$ of the MOSFETs switches. Figure **2-3** depicts the transition method. This technique has an overlapping of the boost and buck modes with a maximum buck and a minimum boost duty cycles, showing three operation modes: buck, buck-boost and boost mode. Hysteresis windows (h_1, h_2) are used to get smooth operating

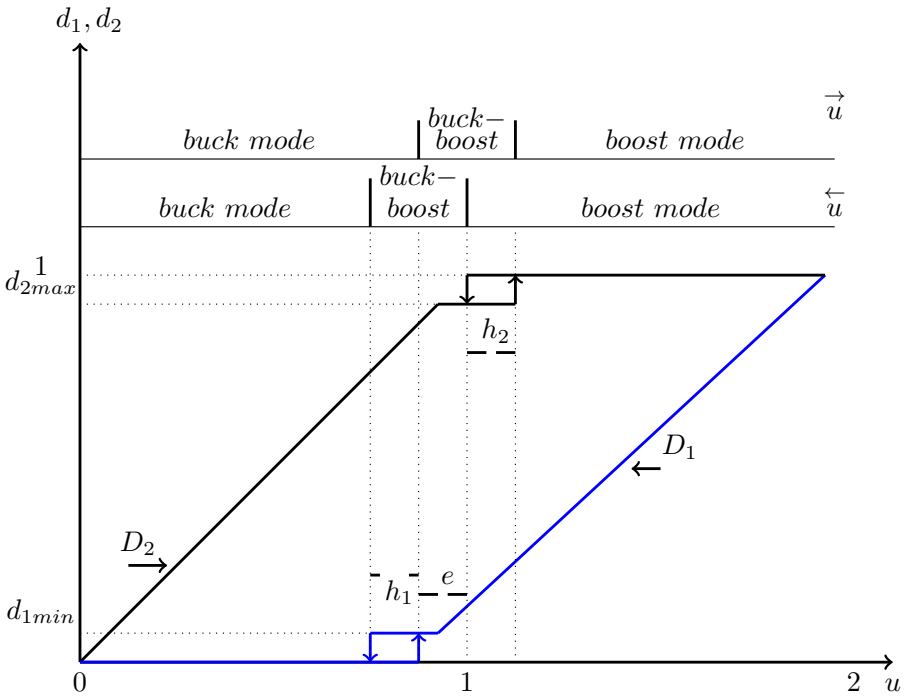

Figure **2-3**: Hysteresis transition method.

mode transitions. In order to operate the converter in steady-state, the duty cycles can be defined as $d_1(t) = D_1$ and $d_2(t) = D_2$.

The operation modes are obtained varying u. When u is increased, the converter operates in buck mode for $0 \leq u < 1 - e$, in buck-boost mode for $1 - e \leq u < 1 + h_2$, in boost mode for $1 + h_2 \leq u < 2$. Following the same process when u is decremented, the converter operates in boost mode for $1 \leq u < 2$, in buck-boost mode for $1 - e - h_1 \leq u < 1$ and buck mode for $0 \leq u < 1 - e - h_1$.

The following conditions should be fulfilled to set the hysteresis window widths:

$$h_1 > d_{1min} \tag{2-1a}$$

$$h_2 > 1 - d_{2max} \tag{2-1b}$$

$$e_{min} = d_{1min} + (1 - d_{2max}) \tag{2-1c}$$

where d_{1min} is the minimum boost duty cycle, d_{2max} is the maximum buck duty cycle and e_{min} is the minimum value of the overlapping coefficient e.

2.4 Conventional noninverting bidirectional buck-boost converter design for EVs application

The conventional noninverting bidirectional dc-dc converter approach from Figure **2-1** is designed to regulate the power flow between the battery and the dc input of the inverter drive. Hence the design has been realized taking into account the requirements from a powertrain used in this work, that emulates an EV, this requirements are listed in Table **2-1**.

Component	Voltage	Power rating
Unidrive SP2202	200 Vac	4/5.5 kW
LSRPM100L motor traction	390 Vdc	4.5 kW
LSRPM90SL motor load	390 Vdc	3 kW

Table **2-1**: System specifications.

The value of peak to peak current ripples for input and output converter are calculated taking into account the nominal power of the traction system, its values correspond to 100 percent of the mean current values. The value of i_{Lm} is the difference between i_g and i_L in Figure **2-1**. The specifications of the buck-boost converter's parameters are given in Table **2-2**, where the rated power is half of the powertrain load power rating. The maximum output current of the converter design is 4 A. The input voltage V_g range goes from 200 V to 400 V, and the conversion ratio is between 1 and 2 in boost mode with a maximum output voltage of 400 V. The switching frequency is 100 kHz.
The components R_d and C_d from Figure **2-1** can be calculated as in [1]:

$$R_d = 0.65\sqrt{\frac{L_m}{C}}, C_d \geq 8C \tag{2-2}$$

An important aspect affecting efficiency but required to obtain the minimum-phase desired dynamics is the power loss in R_d (P_{Rd}) that is analyzed in [38]. Dissipated power P_{Rd} depends on the amplitude of the voltage ripple, Δv_c, at the intermediate capacitor, assuming a ripple of triangular shape so that its rms value can be estimated easily, as follows:

$$P_{Rd} = \frac{\Delta v_c^2}{12R_d}, \tag{2-3}$$

Table **2-3** lists the expressions to calculate currents and voltages peak-to-peak ripples, where $T = 1/f_s$, f_s is the switching frequency.

Parameter	Value
Input voltage V_g	200-400 V
Output voltage V_o	100-400 V
Rated Power P_n	1.6 kW
Δi_L	4 A
Δi_g	7 A
Δi_{Lm}	3 A
Δv_c	15 V
f_s	100 kHz
P_{Rd}	2 W

Table **2-2**: Buck-boost converter design criteria with ouput filter.

Ripple	Buck mode	Boost mode
Δi_L	$\frac{(V_g - V_o)V_o T}{V_g L_o}$	$\frac{V_g(V_o - V_g)T}{V_o L_o}$
Δi_{Lm}	0	$\frac{V_g(V_o - V_g)T}{V_o L_m}$
Δv_c	$\frac{(V_g - V_o)V_o^2 T}{V_g^2 R_o C}$	$\frac{(V_o - V_g)T}{R_o C}$

Table **2-3**: Peak-to-peak ripples of the buck-boost converter [1].

The converter is designed for boost mode to regulate 350 V in the dc-link voltage, with $V_g = 200$ V. The steps to calculate the component values of the buck-boost converter are explained in Algorithm 1.

Algorithm 1 Buck-boost cell design

1: **Input:** Δi_{Lm}, P_{Rd}, V_o, V_g, f_s, Δv_c value
2: Find L_m from Δi_{Lm} equation from Table **2-3** in boost mode.
3: Find R_d,from Eq. 2-3.
4: Compute C and C_d using Eq. 2-2 .
5: **Output:** L_m, C, R_d and C_d values.

The value of the inductor L_o is calculated following the equation for Δi_L from Table 2-3 in boost mode and its value is 216 μH. Table **2-4** shows the description and values for each buck-boost converter components for its implementation.

Component	Description	Reference
Q_1, Q_2, Q_3, Q_4	Silicon Carbide Power MOSFET	C2M0080120D
C	Polypropylene Capacitor, 4 x 0.33 μF	R76PN33304030J
R_d	Damping resistor, $10\Omega, 10W, 500V$	BPR10100J
C_d	Damping Capacitor Polypropylene, 10 μF, $700V$	MKP1848S61070JP2C
L_m	Coupled inductors, 285 μH Number turns:93	Core:77908 Magnetics Wire size: $18AWG$,
MOSFET Driver	High side and Low side, 10V-18V	UCC27714D
Converter dc-dc	1500 VDC Isolation, to feed the high side of MOSFET driver	ISE1515A

Table **2-4**: Conventional bidirectional noninverting buck-Boost Converter Components.

2.4.1 Coupled inductor design

The transformer model parameters of the non symmetrical coupled inductors for the conventional noninverting buck-boost converter are $L_1 = L_m$, $L_2 = L_o + L_m$ and $M = L_m$. As shown in Figure **2-4**, a tightly coupled inductors pair (coupling coefficient $k_1 \approx 1$) have been built by coiling around a toroidal core in uniform interleaved arrangement an equal number of turns (93) of 18 AWG cooper wire for the primary and the secondary windings. The core is a Magnetics 77908 toroid with a relative permeability coefficient of $\mu_r = 26$. A noncoupled inductor $L_o = 216$ μH (shown in Figure **2-4** but not in Fig. **2-5**), built by winding 65 turns of 18 AWG cooper wire around a Magnetics 77191 core, has been associated in series with the secondary winding. The equivalent transformer model of the arrangement has a global coupling coefficient $k_2 = M/\sqrt{L_1 L_2} = L_m/\sqrt{L_m(L_o + L_m)} = 0.75$.

To verify the coupling coefficient value a 2-dimensional finite element method (2D-FEM) software is used. The software is FEMM 4.2. The flux linkages in the primary and secondary windings for a primary current $I_1 = 4$ A and keeping the secondary in open circuit, were $\phi_1 = 1.13074$ mWb, $\phi_2 = 1.12359$ mWb, respectively. Therefore, the primary self inductance is $L_1 = \phi_1/I_1 = 282$ μH and the mutual inductance is $M = \phi_2/I_1 = 280$ μH. Similar steps were used to find the self inductance of the secondary, $L_2 = 280$ μH. Hence the simulated results of the coupling coefficient were $k \approx 1$. As expected from the interleaved arrangement,

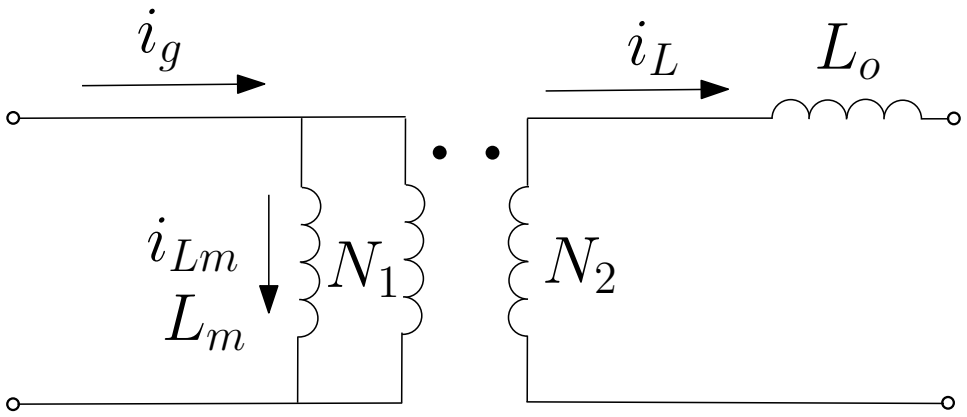

Figure **2-4**: Coupled inductor with output inductor.

the distribution of the flux density in Figure **2-5** core is uniform.

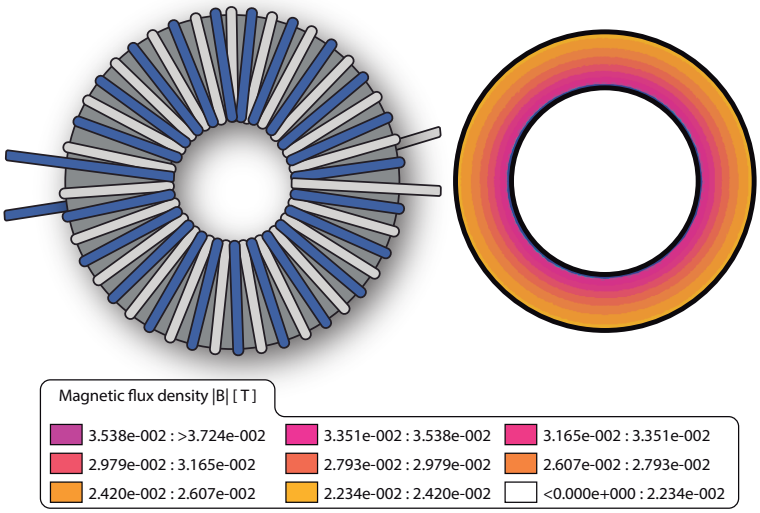

Figure **2-5**: Flux density map of coupled inductor model using FEMM with $k_1 = 1$.

2.4.2 Simulation with a Constant Power Load (CPL)

A PSIM simulation is developed using a simplified model of the traction part of the system. The simplified model consists of a Constant Power Load (CPL), and is presented in [45], where the authors expose that when a converter-inverter regulates its output, it operates as a CPL. The product of speed by torque is the power in a motor, since it is constant, the electrical power at the input of the motor will also be constant [46].

In Figure **2-6**, the converter schematic and the CPL can be appreciated, which is modelled as voltage controlled current source and limited by the maximum current consumption.

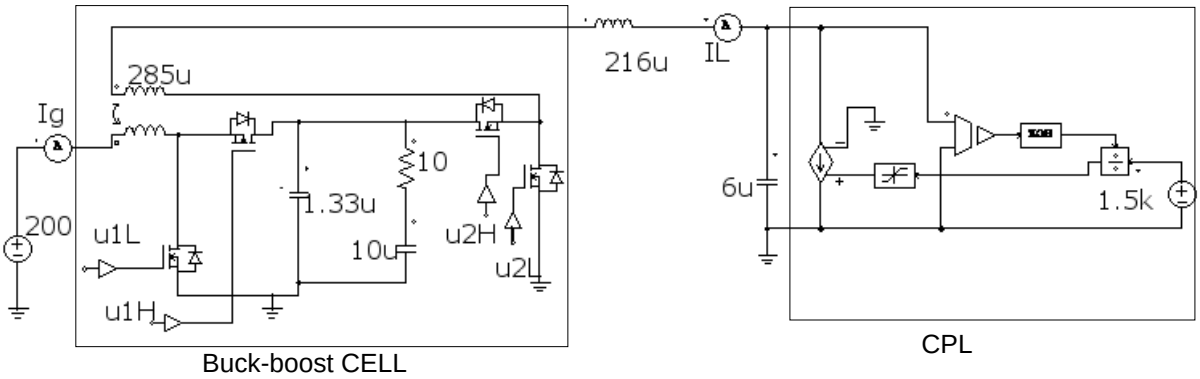

Figure **2-6**: Buck-boost converter with CPL schematic using PSIM.

The buck and boost mode has been simulated with a reference power source $P = 1.5$ kW. The dc link capacitor $C_o = 6$ uF is selected with the criteria proposed in [47].
To generate the start-up transient in open loop, the values of the transition parameters are defined, as follows: $d_{2max} = 0.99$, $d_{1min} = 0.01$, $e = 0.05$, $h_1 = 0.02$ and $h_2 = 0.02$. The variable control $u(t)$ is used to calculate the values for $d_1(t)$ and $d_2(t)$. To do so, $u(t)$ is linearly increased and update each switch cycle, until these duty cycles have obtained their corresponding values (D_1,D_2) at the desired operating point.

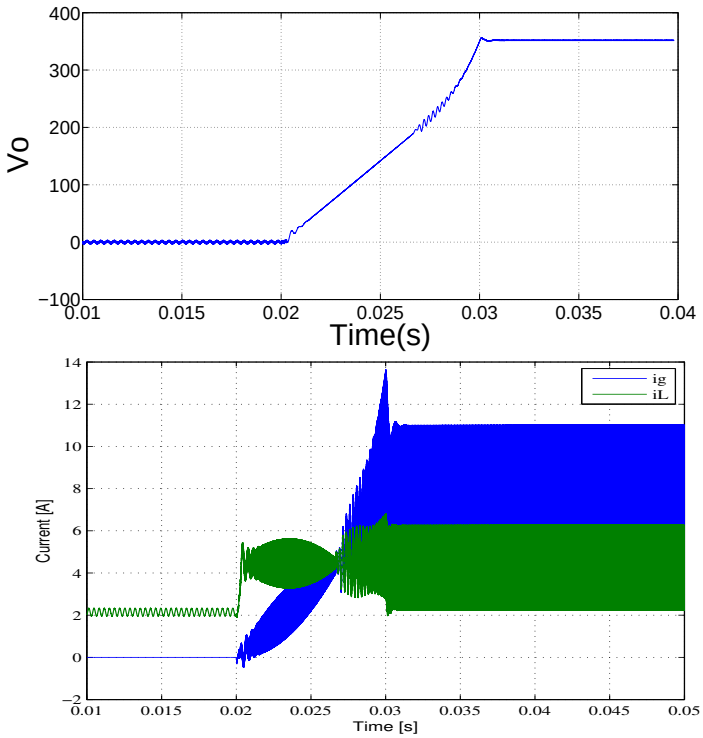

Figure **2-7**: PSIM simulation of the start-up transient with final output voltage in boost mode.

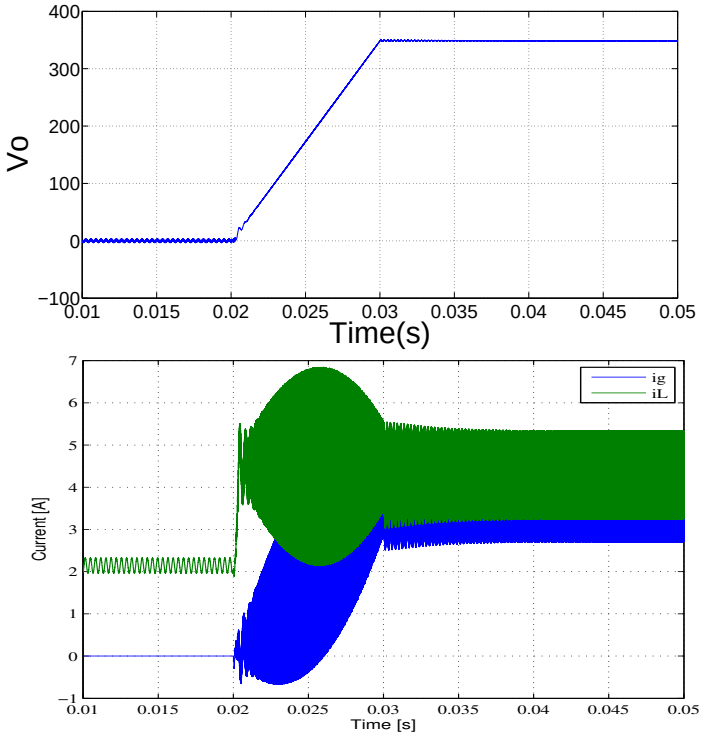

Figure **2-8**: PSIM simulation of the start-up transient with final output voltage in buck mode.

Overall results for boost mode and buck mode are showed in Figures **2-7**, and **2-8**, respectively. The input voltage V_g is set at 200 V for boost mode and 400 V for buck mode. The duty cycles (D_1,D_2) are selected taking into account the rated voltage (350 V).

After the start-up transient the converter output voltage is established in 350 V. This is accorded with the design criteria. The input and output current ripple values are 7 A and 4 A, respectively, according with the values in Table **2-2**. The current ripples change in function of the voltage values, and are in agreement with the equations from the Table **2-3** for boost and buck mode. The voltage and current oscillations are present because start-up test is operating in open loop. The value of switching frequency also satisfies the design.

2.4.3 Experimental results

In order to verify the dc-dc converter with the output filter, the conventional 1.6-kW converter prototype described in Figure **2-1** is implemented with the component values showed in Table **2-4** and is operated in open loop. A direct voltage source is used as power supply for the buck-boost converter. The Enhanced Pulse Width Modulator (ePWM) module from Texas Instruments TMS320F28377S Digital Signal Control (DSC) has been used to generate the activation signals for the MOSFETs switch. The parameters of the transition method

used to initialize the start-up transient in open loop are adjusted with the same values described in Section 2.3.2.

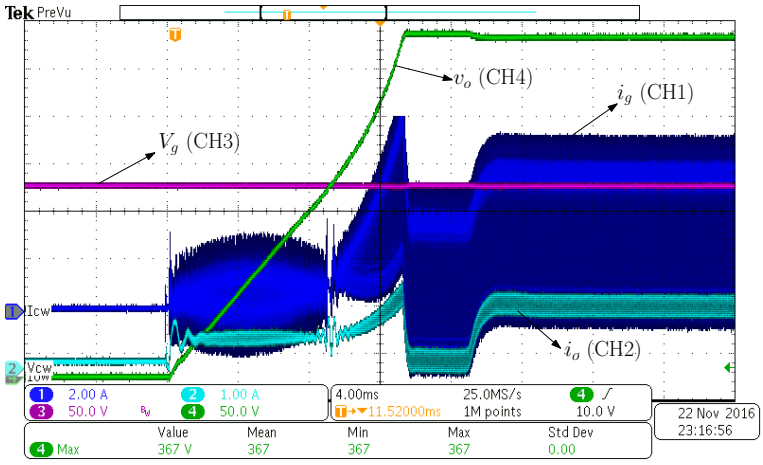

Figure **2-9**: Experimental results with an active load of 300 Ω and final output voltage in boost mode. CH1: input current i_g (2 A/div); CH2: current in the load i_o (1 A/div); CH3: input voltage $V_g = 200$ V (50 V/div); CH4: output voltage v_o (50 V/div); time base 4 ms.

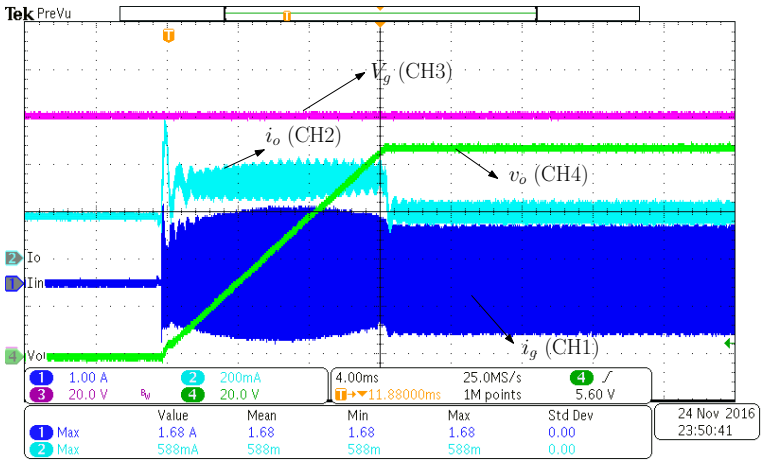

Figure **2-10**: Experimental results with an active load of 300 Ω and final output voltage in buck mode. CH1: input current i_g (1 A/div); CH2: current in the load i_o (200 mA/div); CH3: input voltage $V_g = 100$ V (20 V/div); CH4: output voltage v_o (20 V/div); time base 4 ms.

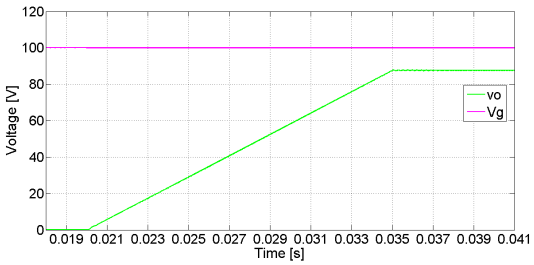

(a)

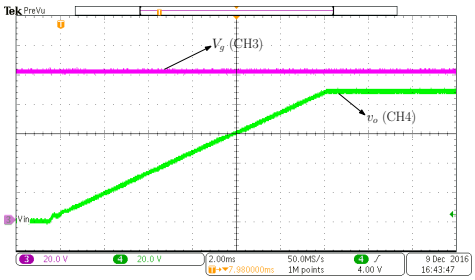

(b)

Figure **2-11**: Results with a power resistor load of 300 Ω with v_o set in buck mode: (a) PSIM simulation (b) experimental results. CH1: V_g (20 V/div); CH2: v_o (20 V/div); time base 2 ms.

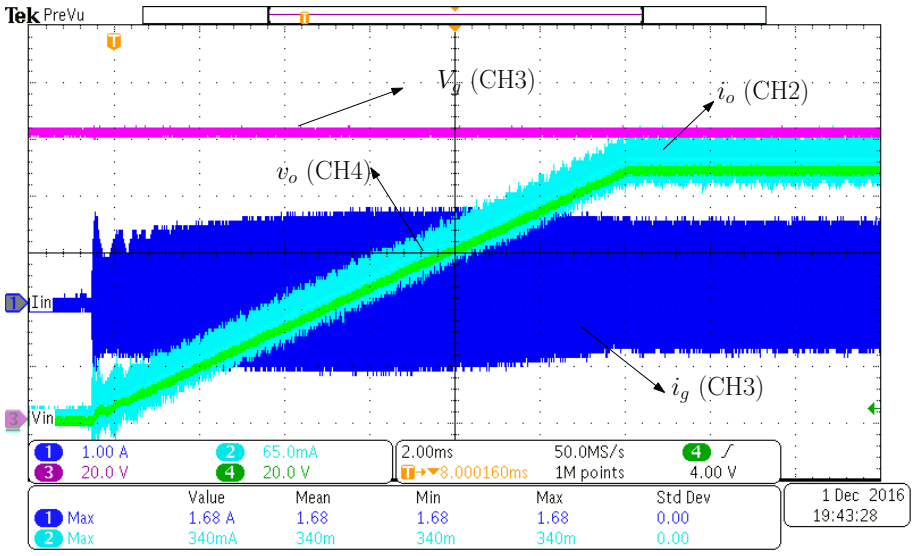

Figure **2-12**: Experimental results with a power resistor load of 300 Ω with v_o set in buck mode. CH1: input current i_g (1 A/div); CH2: current in the load i_o (65 mA/div); CH3: input voltage $V_g = 100$ V (20 V/div); CH4: output voltage v_o (20 V/div); time base 2 ms.

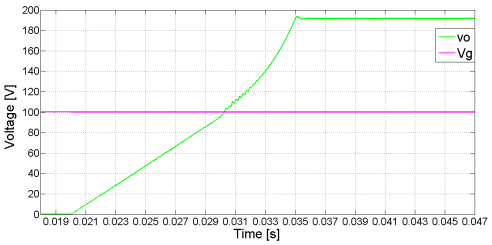

(a)

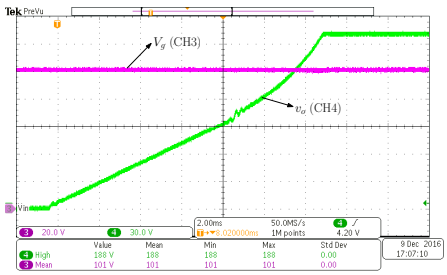

(b)

Figure **2-13**: Results with a power resistor load of 300 Ω and V_g = 100 V with v_o set in boost mode. (a) PSIM simulation (b) experimental results. CH1: V_g (20 V/div); CH2: v_o (30 V/div); time base 4 ms.

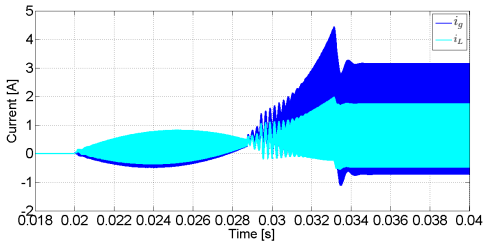

(a)

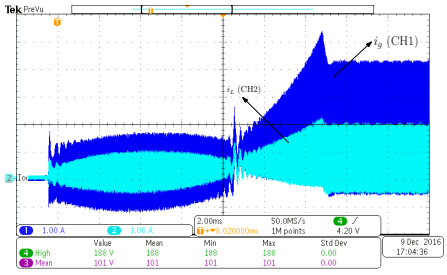

(b)

Figure **2-14**: Results with a power resistor load of 300 Ω with v_o set in boost mode. (a) PSIM simulation (b) experimental results. CH1: i_g (1 A/div); CH2: i_L (1 A/div); time base 4 ms.

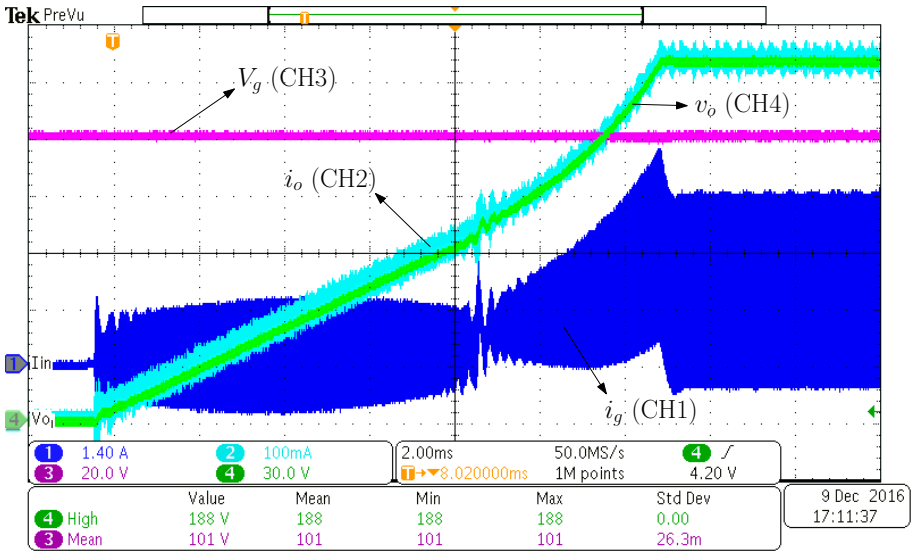

Figure **2-15**: Experimental results with a power resistor load of 300 Ω with v_o set in boost mode. CH1: input current i_g (1.4 A/div); CH2: current in the load i_o (100 mA/div); CH3: input voltage $V_g = 100$ V (20 V/div); CH4: output voltage v_o (30 V/div); time base 2 ms.

The prototype is tested in boost and buck mode. Two experiments are performed, the first experiment is composed by an active load (AMREL PLA4K-600-200-I) in constant resistance mode of 300 Ω with $V_g = 100$ V and V_o is set at 87.6V in buck mode. In this way for boost mode, V_g is set at 200 V, the value of duty cycles D_1 and D_2 are selected to set $V_o = 350$ V.

The second experiment consists in a power resistor load of 300 Ω with $V_g = 100$ V. The value of duty cycles D_1 and D_2 are selected to set $V_o = 87.6$ V for buck mode and $V_o = 191$ V for boost mode. Experimental results for active load in boost and buck mode are showed in Figures **2-9** and **2-10**, respectively. The experimental results in boost mode, with a value of $V_o = 367$ V after a start-up transient with $V_g = 200$ V. In this mode, it is possible to see the buck-boost transition when V_g and V_o are equal to 100 V, as shown in Figure **2-9**.
For buck mode the output voltage is established in 88 V with $V_g = 100$ V. i_o is the current at the resistor, the waveform of the current i_o using an active load in constant resistance mode is not able to rightly represent the behavior in a resistance as seen in Figures **2-9** and **2-10**, where the current in the load i_o does not follow the output voltage waveform. For that reason experiments with a power resistor are described in this section. The simulation and experimental results in buck mode using a power resistor load (300 Ω - 500 W) are shown in Figures **2-11** and **2-12**. Figure **2-11**(a) shows simulated start-up behavior of input and output voltage. Figure **2-11**(b) represents experimental corresponding results, which are in good agreement with the simulated ones. In Figure **2-12** it is possible to see that the output current is proportional to the output voltage waveform as it is using a resistance

load. Results in boost mode for the second experiment are detailed in Figures **2-13**, **2-14** and **2-15**. The experimental value of V_o after the start-up transient is 188 V. Experimental results agree with the simulated ones and again validate the converter design. Although the tests were realized in open loop, the effect of oscillation in the transition was not significant. In Figure **2-16** the converter operates in boost mode with an input voltage $V_g = 200$ V, the output voltage is 382.8 V, in this experiment, it is possible see the switching frequency of 100 kHz, and the current ripples are $\Delta i_L = 4$ A, and $\Delta i_g = 7$ A, this values correspond to the prediction accuracy of the theoretical values as was summarized in Table **2-2**.

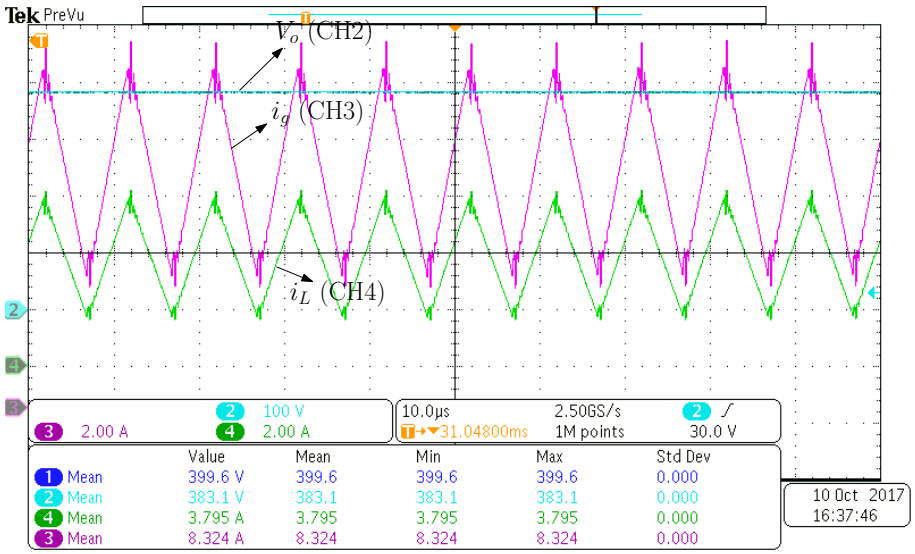

Figure **2-16**: Experimental results with a power resistor active load of 100 Ω with V_o set in boost mode. CH3: input current i_g (2 A/div); CH4: output current i_L (2A/div); CH2: output voltage V_o (100 V/div); time base 10 us. Set input voltage 200 V.

2.4.4 Efficiency analysis of the conventional bidirectional noninverting buck-boost converter

Figure **2-17** shows the converter efficiency with coupled inductor, the structure of the coupled inductor was described in Figure **2-4** with a global coefficient $k_2 = 0.75$. In this work the efficiency was measured using a Yokogawa WT 3000 precision power analyzer connected at the input and the output of the converter, and was taken with the converter working with $I_L = 4$ A. Overall measurements of efficiency respect to the power output of the converter show significant power loss. Part of this power loss have relation to the effect of winding-to-winding parasitic capacitance of the coupled inductor in the switching loss.

Frequency [Hz]	Capacitance Wind1-Wind2 [nF]
63095.7	14.52
89125.1	14.50
125892.5	14.51
177827.9	14.52
251188.6	14.56

Table **2-5**: Winding-to-winding capacitance value for the structure of coupled inductor seen in Figure **2-5**.

Measurements of the winding-to-winding parasitic capacitances of the coupled inductors were performed using a QuadTech 1910 LCR meter. The measurements taken between the primary and secondary windings at different frequencies are listed in Table **2-5**. For all the frequencies, the value of the parasitic capacitor is $C_p \approx 15$ nF for the coupled inductor with k_1, a quite large value explained by the highly interleaved winding arrangement required to have tight magnetic coupling.

Considering boost mode, in each switching cycle the parasitic capacitor is charged to the output voltage and discharged completely to zero volts. When the converter works in buck mode, the parasitic capacitor voltage evolves between the input voltage and zero volts. For that reason the power loss associated with the winding-to-winding parasitic capacitance are contanst in buck mode. Assuming that all the energy stored in the parasitic capacitor $W = CV^2/2$ is lost, when the voltage applied across the switch is 400 V at 100 kHz the power loss reaches 120 W. Simulations in LTspice have been developed to roughly predict the power loss associated to the winding-to-winding parasitic capacitance of the coupled inductors. In addition to the previous capacitance values, the simulation uses the parameters in Table **2-4**, an almost ideal switch (SW) with only on-resistance ($R_{on} = 100$ mΩ, $T_{on} = 5$ μs) represents the switch Q_2 in Figure **2-1**, and $R_o = 50$ Ω. Figure **2-18** shows the circuit diagrams used to simulate the coupled inductor when the converter is working in boost and buck modes. For boost mode (Figure **2-18** (a)) with $V_o = 400$ V and $V_g = 200$ V. The parameters for the simulation in buck mode (Figure **2-18** (b)) are the same that for boost mode. The parameters that change here are the input voltage $V_g = 400$ V and the pulse source which has a time on $T_{on} = 7$ μs, and SW represents Q_3 in Figure **2-1**. The voltage output in this mode is $V_o = 192$ V.

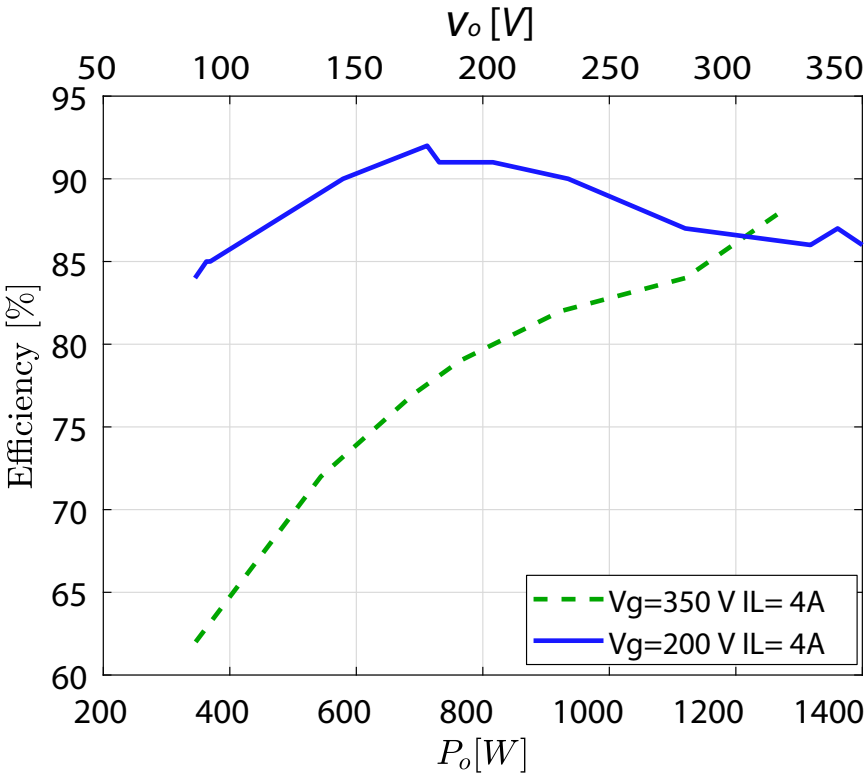

Figure **2-17**: Results of the efficiency measurements fixed at 200 V and 350 V values of the input voltage V_g for the conventional bidirectional noninverting buck-boost converter.

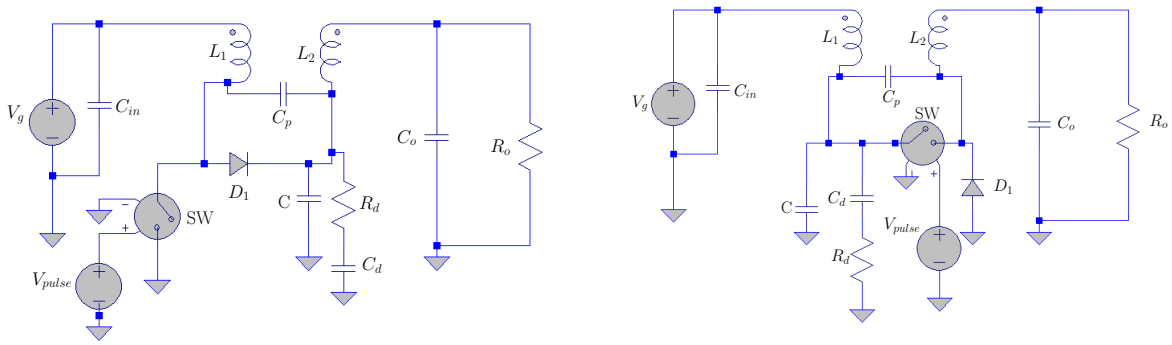

(a) (b)

Figure **2-18**: Circuit diagram corresponding to the LTspice simulation. (a) in boost mode (b) in buck mode.

Figure **2-19** shows the power deliver by the input voltage P_{in} and the output power P_o for each operation mode. The value of C_p is 15 nF. For boost mode (see Figure **2-19** (a)) the

average value of input power is -3.4418 kW and for the output power is 3.2392 kW, the general power loss in this case is $P_{loss} \approx 202$ W. In buck mode (see Figure **2-19** (b)) the average power input is -1.8466 kW and the output power is 1.714 kW, the P_{loss} in this mode is 132 W.

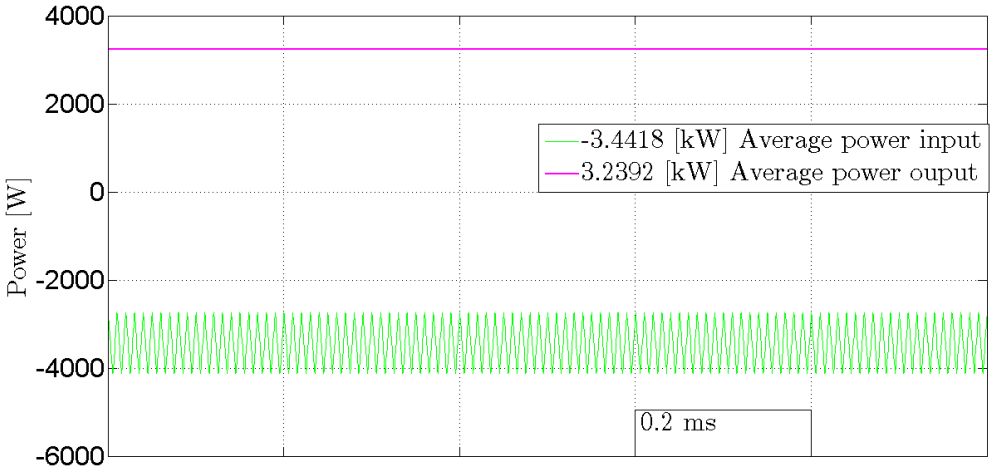

(a)

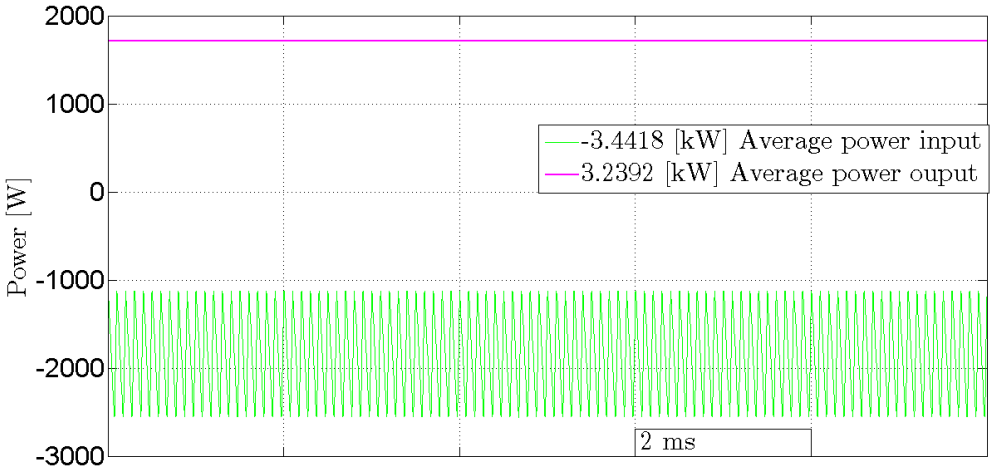

(b)

Figure **2-19**: Simulated results of power measurements using LTspice. (a) in boost mode (b) in buck mode.

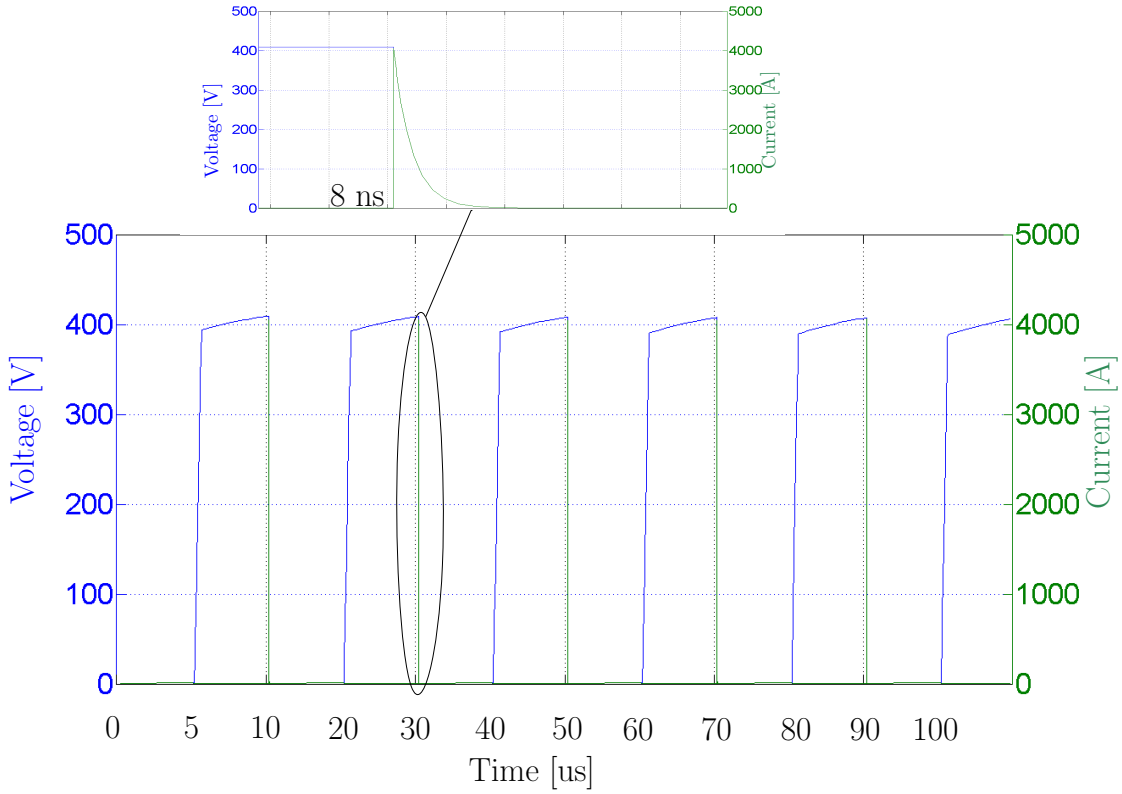

Figure **2-20**: Simulated results of current and voltage in SW Q_2 for boost mode using LTspice.

Figure **2-20** shows the simulated results of current and voltage across SW when the converter is working in boost mode. With a parasitic capacitance of 15 nF connected between the b and d nodes (see Fig. **2-1**). Each switching period, the 15 nF capacitor is discharged exponentially through the switch (R_{on} = 100 mΩ, T_{on} = 5 μs) with a peak current near to 4 kA (400 V/R_{on}) in about 8 ns. Note that other switching losses have not been modelled.

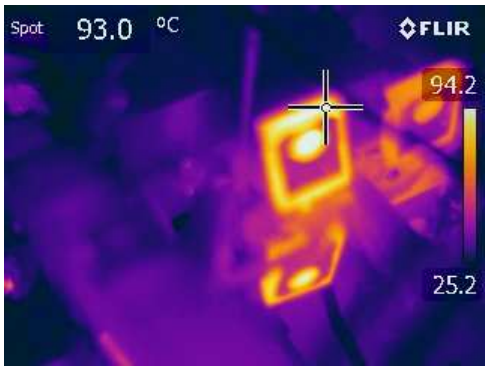

Figure **2-21**: Thermal image of the half bridge MOSFET boost side.

The temperature in the half bridge MOSFET boost side is shown in Figure **2-21** when the converter is working in boost mode. The MOSFET on the left (Q_2) has a significant warming as a result of higher switching loss than (Q_1) from Figure **2-1**. This is an issue at the discharge of the parasitic capacitance that can increase switching loss among the devices. Thermal imaging confirmed that this power is mainly dissipated by the $R_{ds(on)}$ of the low-side MOSFET of the switching half-bridge.

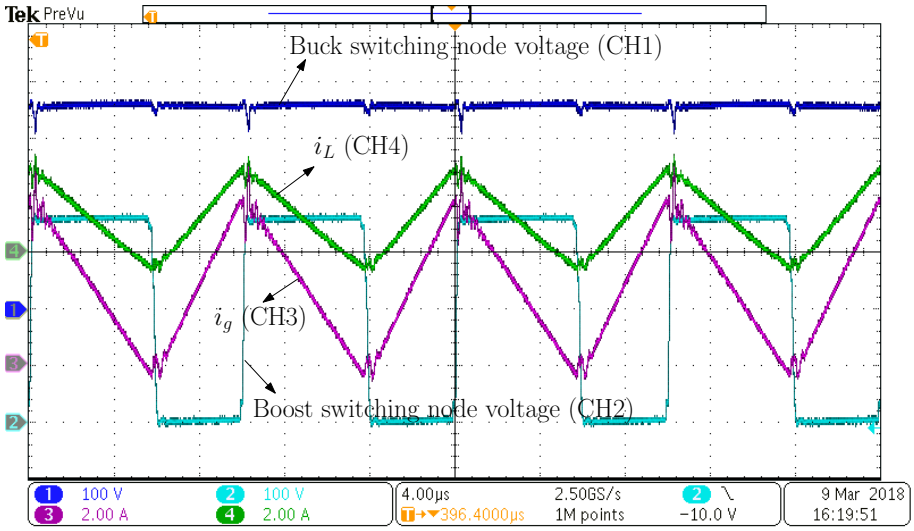

Figure **2-22**: waveforms of the conventional bidirectional noninverting buck-boost operating in ZCS point.

Although, the operating point has a zero-current-switching (ZCS), as is shown in Figure **2-22**, the buck switching node voltage is the node d and the boost switching node voltage is the node b in Figure **2-1**, for this results the efficiency is low (70 %). In this case $V_g = 200$ V and $V_o = 344$ V. The output power in this operating point is $P_o = 382$ W. This efficiency is because the device Q_2 dispels the voltage charge in the parasitic capacitor. Figure **2-23** shows that with ZCS, the gate-to-source voltage of Q_2 (see CH4 in Figure **2-23**) presents significant oscillations in virtue of the parasitic capacitor while the discharge in the switching period has not been finished.

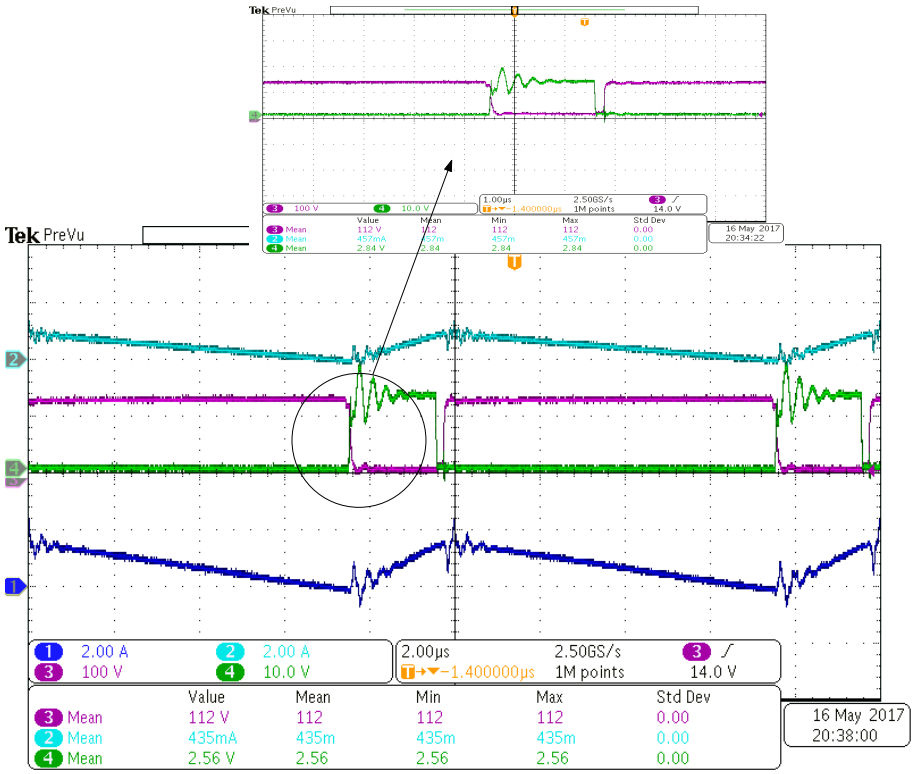

Figure **2-23**: Waveform in ZCS operating point. CH1; input current i_g (2A/div) CH2: output current i_L (2A/div);CH3: v_s (100 V/div); CH4: v_{gsQ_2} (10 V/div); time base 2 us. input voltage 200 V.

2.5 Proposed noninverting bidirectional buck-boost converter design for EV application

In this section the proposed converter approach analysis from Figure **2-1** is presented, where the converter has been implemented with just two loosely coupled inductors (coupling coefficient k = 0.5) without output filter. The component values for the proposed buck-boost converter from Figure **2-1** have been selected following the parameters of the converter's specification given in Table **2-6** and according to the requirements of the system described in Table **2-1**. The value of peak to peak current ripples for input and output converter are calculated taking into account the nominal power of the traction system. To study the stability of the converter in open loop, the transfer functions from the input signals to the output voltage are found, in order to ensure that the internal system dynamic is sufficiently damped, and the polynomials from the transfer functions are tested for different operating points of the converter. Therefore, the damping coefficients of the complex zeros have to be grater than 0.5 ($\zeta > 0.5$).

The small signal state-state vector $\bar{x}$ is defined as $\bar{x} = [\bar{i_g}, \bar{i_L}, \bar{v_c}, \bar{v_{cd}}, \bar{v_o}]^T$, where $\bar{i_g}$ and $\bar{i_L}$

Parameter	Value
Input voltage V_g	200-400 V
Output voltage V_o	100-400 V
Rated Power P_n	1.6 kW
f_s	100 kHz
P_{Rd}	4 W

Table **2-6**: Design criteria for proposed buck-boost converter.

are the averaged input and output current, respectively, $\bar{v_c}$ is the averaged voltage in the intermediate capacitor, $\bar{v_{cd}}$ is the averaged voltage in the damping capacitor and $\bar{v_o}$ is the averaged output voltage. The input vector is $\bar{d} = [\bar{d_1}, \bar{d_2}]$. A continuous conduction mode (CCM) operation for the converter is considered in the analysis. $L = L_1 = L_2$, where L_1 and L_2 are the self inductance value for the first and the second coil of the coupled inductor, respectively. And M is the mutual inductance of the coupled inductor. Finally R_d and C_d represent the components of the damping network. Using the differential equations of the state variables expressed in [44] and the use the sate-space averaging (SSA) method to the following expressions for the state variables of the proposed converter from Figure **2-1**:

$$\begin{aligned}
\frac{d\bar{i_g}}{dt}(t) &= \frac{L(\bar{v_g} - \bar{v_c}(1-\bar{d_1})) - M(\bar{v_o} - \bar{v_c}\bar{d_2})}{L^2 - M^2} \\
\frac{d\bar{i_L}}{dt}(t) &= \frac{M(\bar{v_g} - \bar{v_c}(1-\bar{d_1})) - L(\bar{v_o} - \bar{v_c}\bar{d_2})}{L^2 - M^2} \\
\frac{d\bar{v_c}}{dt}(t) &= \frac{1}{C}\left(-\bar{i_L}\bar{d_2} + i_g\left(-\bar{d_1}+1\right) - \frac{1}{R_d}\left(\bar{v_c} - \bar{v_{cd}}\right)\right) \\
\frac{d\bar{v_{cd}}}{dt}(t) &= \frac{\bar{v_c} - \bar{v_{cd}}}{C_d R_d}. \\
\frac{d\bar{v_o}}{dt}(t) &= \frac{\bar{i_L}}{C_o} - \frac{\bar{v_o}}{R_o C_o}
\end{aligned} \tag{2-4}$$

Now, the DC components of the state variables are defined as $X = [I_g, I_L, V_c, V_{cd}, V_o]$, and the input signals control $D = [D_1, D_2]$, where D_1 and D_2 are the duty cycles in steady state for boost and buck mode, respectively. And with $v_g = V_g$.
Equating the differential equations (2-4) to zero and solving to determine the DC components of currents and voltages, the steady-state expressions for currents and voltages of the converter are:

$$I_L = -\frac{V_g D_2}{(D_1 - 1)R_o} \tag{2-5}$$

$$V_C = -\frac{V_g}{(D_1 - 1)} \tag{2-6}$$

$$V_{Cd} = -\frac{V_g}{(D_1 - 1)} \tag{2-7}$$

$$V_o = -\frac{D_2 V_g}{(D_1 - 1)} \tag{2-8}$$

$$I_g = -\frac{D_2 I_L}{(D_1 - 1)} \tag{2-9}$$

The duty cycles can be calculated from the output and input voltage, as follows:

$$\begin{aligned} D_1 &= \frac{1}{V_o}\left(-V_g + V_o\right) \\ D_2 &= \frac{V_o}{V_g} \end{aligned} \tag{2-10}$$

The expressions for obtaining peak-to-peak ripples of currents and voltages, are shown in Table **2-7**, where $T = 1/f_s$, f_s is the switching frequency.

Ripple	Buck mode	Boost mode
Δi_L	$\frac{V_o T}{V_g(L^2 - M^2)}(V_g - V_o)L$	$\frac{V_g T}{V_o(L^2 - M^2)}(V_o - V_g)M$
Δi_g	$\frac{V_o T}{V_g(L^2 - M^2)}(V_g - V_o)M$	$\frac{V_g T}{V_o(L^2 - M^2)}(V_o - V_g)L$
Δv_c	$\frac{D_2 I_L}{C} T\left(D_2 - 1\right)$	$\frac{D_1 I_L}{C} T$

Table **2-7**: Peak-to-peak ripples of the proposed bidirectional noninverting buck-boost converter.

2.5.1 Analysis of the noninverting bidirectional buck-boost converter

The analysis of the converter when the load is a constant current source, as is show in Figure **2-24**, where the converter operates with positive output current for the traction mode in EV application and with negative output current when the powertrain operates in regenerative braking mode. The state variables are defined in the small signal state vector $\bar{x} = [\bar{i_g}, \bar{v_c}, \bar{v_{cd}}]^T$, and the output variables are $\bar{y} = [\bar{v_o}, \bar{i_c}]^T$, being $\bar{v_o} = \bar{v_c}d_2 + M(\bar{v_g} - \bar{v_c}(1-d_1))/L$, $\bar{i_c} = \bar{i_g}(1-d_1) - \bar{i_L}d_2 - (\bar{v_c} - \bar{v_{cd}})/R_d$, and the input vector is $\bar{d} = [\bar{d_1}, \bar{d_2}]$.

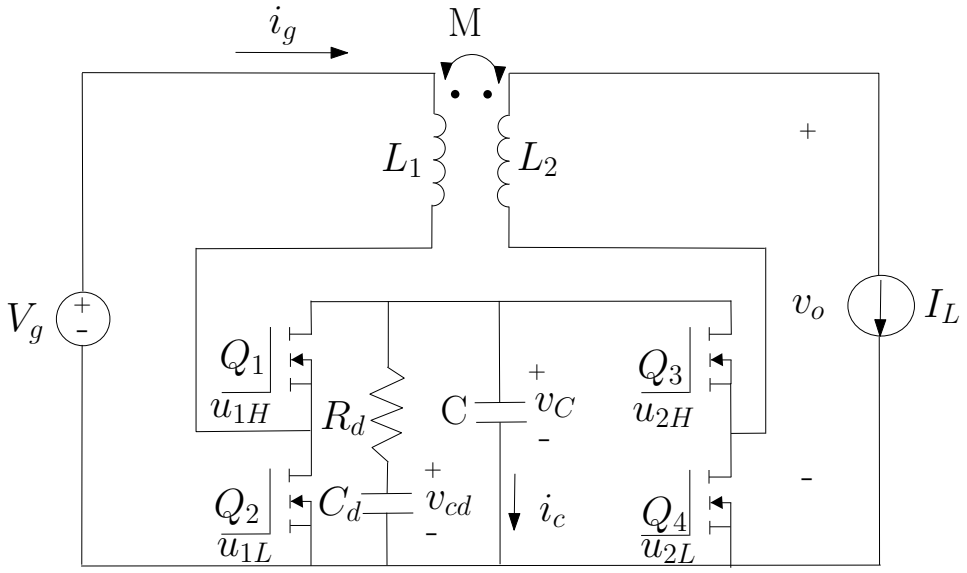

Figure **2-24**: Buck-boost converter with coupled inductor and current source at the output in traction operation.

In [1], a linearization of the differential equations around the operating point is introduced. Doing so, the small-signal model is obtained (2-11),

$$\begin{aligned} \frac{d\bar{x}}{dt} &= A\bar{x} + B\bar{d} \\ \bar{y} &= C\bar{x} + D\bar{d} \end{aligned} \tag{2-11}$$

where the input vector of the system are the control signals, and the values of matrices A, B, C and D are given by:

$$A = \begin{pmatrix} 0 & \frac{L(D_1-1)-\frac{M^2(D_1-1)}{L}}{L^2-M^2} & 0 \\ -\frac{D_1-1}{C} & -\frac{1}{CR_d} & \frac{1}{CR_d} \\ 0 & \frac{1}{C_dR_d} & -\frac{1}{\mathrm{Cd}R_d} \end{pmatrix}$$

$$B = \begin{pmatrix} -\frac{\frac{LV_g}{D_1-1}-\frac{M^2V_g}{L(D_1-1)}}{L^2-M^2} & 0 \\ \frac{D_2I_L}{C(D_1-1)} & -\frac{I_L}{C} \\ 0 & 0 \end{pmatrix} \tag{2-12}$$

$$C = \begin{pmatrix} 0 & D_2+\frac{M(D_1-1)}{L} & 0 \\ 1-D_1 & -\frac{1}{R_d} & \frac{1}{R_d} \end{pmatrix}$$

$$D = \begin{pmatrix} -\frac{MV_g}{L(D_1-1)} & -\frac{V_g}{D_1-1} \\ \frac{D_2I_L}{D_1-1} & -I_L \end{pmatrix}$$

The buck-boost converter is designed to regulate the power flow between the battery and the dc input of an inverter in a powertrain. Therefore, the transfer function from the input signals to the output voltage are found, as follows:

$$G_{v_od_1} = \frac{\bar{v_o}(s)}{\bar{d_1}(s)} \quad \text{when } D_2 = 1 \text{ in boost mode}$$
$$G_{v_od_2} = \frac{\bar{v_o}(s)}{\bar{d_2}(s)} \quad \text{when } D_1 = 0 \text{ in buck mode}$$

The component values are evaluated testing the transfer functions $G_{v_od_1}$ and $G_{v_od_2}$, taking into account that the zeros must be sufficiently damped. In boost mode, the numerator of $G_{v_od_1}(s)$ is a third-degree polynomial (2-13)

$$s^3 + \sigma_2 s^2 + \sigma_1 s + \sigma_0 \tag{2-13}$$

where:

$$\begin{aligned}
\sigma_0 &= -\frac{1}{CC_dR_dM}\left(D_1-1\right)\\
\sigma_1 &= \frac{I_L}{CC_dR_dV_g}\left(\frac{-L}{M}+(1-D_1)\right)+(1-D_1)\frac{1}{MC}\\
\sigma_2 &= \frac{1}{R_d}\left(\frac{1}{C_d}+\frac{1}{C}\right)+\frac{I_L}{CV_g}
\end{aligned} \tag{2-14}$$

and for buck mode, the numerator of $G_{v_od2}(s)$ is

$$s^3+\rho_2 s^2+\rho_1 s+\rho_0 \tag{2-15}$$

where:

$$\begin{aligned}
\rho_0 &= \frac{1}{CC_dLR_d}\\
\rho_1 &= \frac{1}{CL}+\frac{I_L}{V_gR_dC_dC}\left(\frac{M}{L}-D_2\right)\\
\rho_2 &= \frac{1}{R_d}\left(\frac{1}{C_d}+\frac{1}{C}\right)+\frac{I_L}{CV_g}\left(\frac{M}{L}-D_2\right)
\end{aligned} \tag{2-16}$$

2.5.2 Circuit design

The component values for the proposed bidirectional noninverting buck-boost converter have been selected taking into account the parameters of converter's specification given in Table **2-7** and according to the requirements of the system described in Table **2-1**. The value of peak-to-peak ripple for input and output currents of the converter are calculated for the nominal current output (4 A), this current is the third part of the power rating for the motor traction as can be seen in Table **2-1**. The components of the damping network can be selected according to the expressions given in (2-2), replacing L_m by M and keeping the same relation for the capacitors, as follows $R_d = 0.65\sqrt{(M/C)}$, $C_d \geq 8C$ [39].

Component	Description	Reference
Q_1, Q_2, Q_3, Q_4	Silicon Carbide Power MOSFET	SCT2450KEC
C	Polipropylene, Capacitor 4 x 0.33 μF	R76PN33304030J
R_d	Damping resistor, 2 X 10 Ω in parallel, 10 W, 500 V	BPR10100J
C_d	Damping Capacitor Polypropylene, 20 μF, 700 V	MKP1848S62070JP2F
M and L	Coupled inductor, 135 μH and 270 μH	Core:77908 Magnetics Wire size: $18AWG$, Number turns:80
MOSFET Driver	High side and Low side, 10V-18V	UCC27714D
Converter dc-dc	1500 VDC Isolation, to feed the high side of MOSFET driver	ISE1515A

Table **2-8**: Proposed bidirectional noninverting buck-boost converter components.

In order to ensure that the internal system dynamic is sufficiently damped, the polynomials from equations (2-13) and (2-15) in traction mode are tested for different operating points of the converter. Therefore, the damping coefficients of the complex zeros have to be grater than 0.5 ($\zeta > 0.5$). The parameter values listed in Table **2-8** are used to evaluate the internal dynamics of the system, the roots of the polynomial characteristic in boost mode are plotted in Figure **2-25** (a), setting $V_g = 200$ V with the output current range $I_L = [1, 8]$ A and duty cycle range $D_1 = [0, 0.5]$ with step variations of 1 A and 0.003 respectively. The testing for buck mode is realized with $V_g = 400$ V, the root values of the polynomial characteristic (2-15) for the same I_L range and duty cycle range $D_2 = [0.25, 1]$ with the same step variations, which are represented in Figure **2-25** (b) . To plot the roots values, these were normalized respect to the natural frequency $\omega_n = 1/\sqrt{MC}$, as in [39]. The normalized converter parameters are expressed as: $C_{dn} = C_d/C$ and $R_{dn} = CR_d\omega_n$.

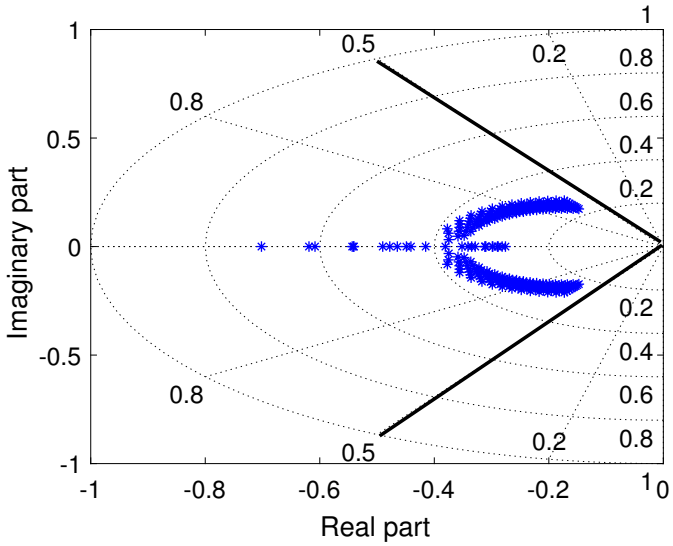

(a)

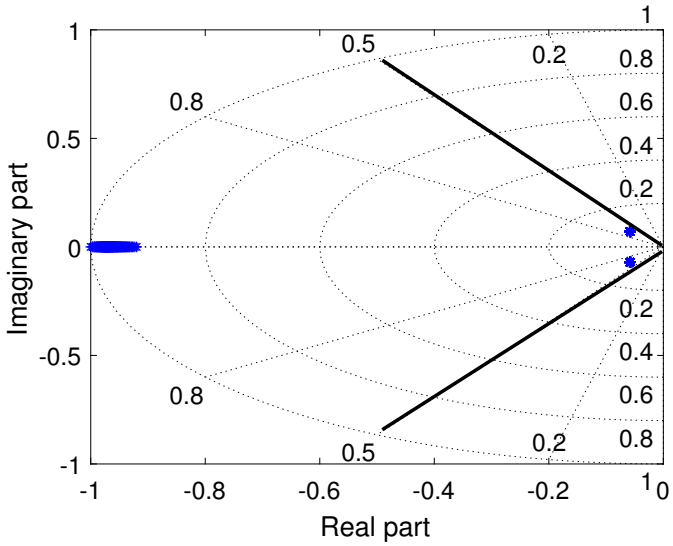

(b)

Figure **2-25**: Roots of the characteristic polynomial of the converter for traction operation: (a) boost mode (b) buck mode.

As another test to be considered, to see the internal system dynamic with the components values chosen when the EV works in regenerative braking mode, is the polynomials from (2-13) and (2-15) are evaluated following the same previous process. For regenerative braking boost mode, the polynomial (2-13) is evaluated with $V_g = 200$ V, with the ouput current range $I_L = [-8, -1]$ A and duty cycle range $D_1 = [0, 0.5]$ with step variations of 1 A and 0.003 respectively, the roots are plotted in Figure **2-26** (a). Figure **2-26** (b) shows the roots for the polynomial step-down buck mode, this was evaluated with $V_g = 400$ V, for the same

range of the output current and $D_2 = [0.25, 1]$ with the same step variations.

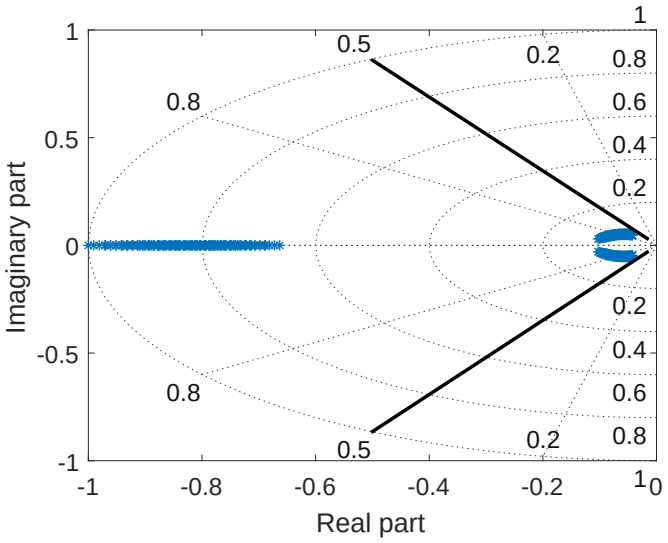

(a)

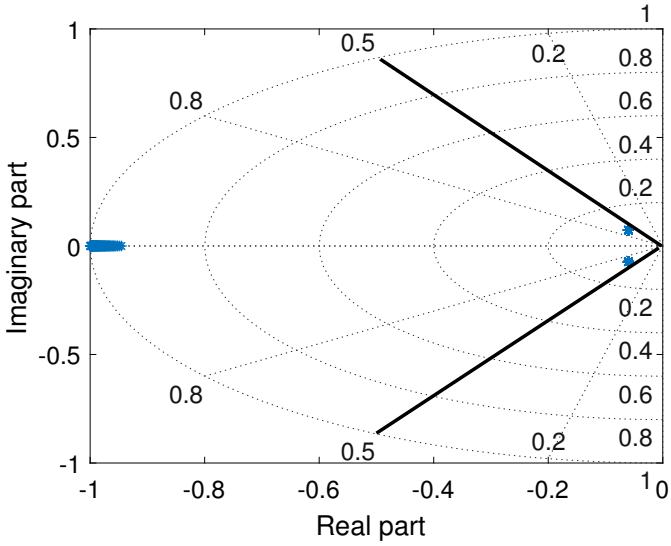

(b)

Figure **2-26**: Roots of the characteristic polynomial of the converter for regenerative braking operation: (a) boost mode (b) buck mode.

2.5.3 Coupled inductor design

The coupled inductor of the proposed bidirectional noninverting dc-dc buck-boost converter of the Figure **2-1** ($N_1/N_2 = 1$, $N_1 = N_2 = 80$ turns), was constructed as is seen in Figure **2-27**-right where each 18-AWG copper coil occupies one half of a Magnetics 77908 toroidal core. The magnetic core and coil wires are the same described in section 2.3.1. Simulation FEMM results give the flux linkage in the primary and secondary winding, which are $\phi_1 = 0.00112043$ Wb, $\phi_2 = 0.000831793$ Wb, respectively. Therefore, the self inductance is $L_1 = \phi_1/I_1 = 280$ μH and the mutual inductance is $M = \phi_2/I_1 = 208$ μH, with $I_1 = 4$, where $L_1 = L_2 = 280$ μH. The obtained coupling coefficient simulated is $k_3 = 0.74$. Figure **2-27** shows the flux density map of the coupled inductor model using the finite element solver FEMM 4.2 for each coupled inductor model in this work. It can be noticed, the distribution of the flux density is uniform in the core for the coupled inductor with $k_1 = 1$ in Figure **2-27**-left used for the conventional noninverting buck-boost converter, whereas not in the core for the coupled inductor with k_3 (Figure **2-27**-right), this verifies the leakage flux of the coupled inductor for the proposed noninverting buck-boost converter.

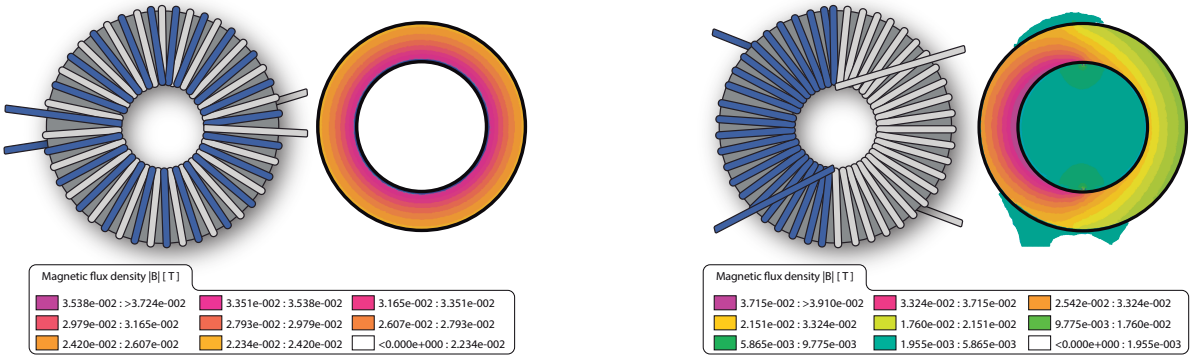

Figure **2-27**: Flux density map of the coupled inductors modeled using FEMM. Left: of Power Stage 1; Right: of Power Stage 2.

2.5.4 Experimental Results

The experiments are carried out considering the proposed buck-boost converter with coupled inductor from Figure **2-1** and the components listed in Table **2-8**. The load has been emulated by the acive load EL 9000 ELEKTRO-AUTOMATIK operating in resistance mode. The results from operating in boost mode is observed in Figure **2-28**, setting an input voltage of 200 V, a resistance value of 90 Ω, where the duty cycle (D_1, D_2) values are chosen to obtain an output voltage of 360 V, the Enhanced Pulse Width Modulator (ePWM) module from Texas Instruments TMS320F28377S Digital Signal Control (DSC) has been used to generate the activation signals for the MOSFETs switch. The steady-state is in good agreement with a switching frequency of 100 kHz, and the current ripples are $\Delta i_L = 2$ A, and $\Delta i_g = 4$ A.

Following the expression for current ripples in boost mode given in Table **2-7**, the parameters obtained from the simulations differed from those extrapolated from the slopes of the current ripples in the experiments ($L = L_1 = L_2 = 270$ uF, $M = 135$ uF and $k_3 = 0.5$) for the structure seen in Figure **2-27** right, which is a lower value than the value obtained from FEMM simulation ($k_3 = 0.74$), due possibly to the magnetic core, which has a low relative permeability coefficient ($\mu_r = 26$), that permits to stimulate leakage flux of the coupled inductor by the presence of nearby magnetic component.

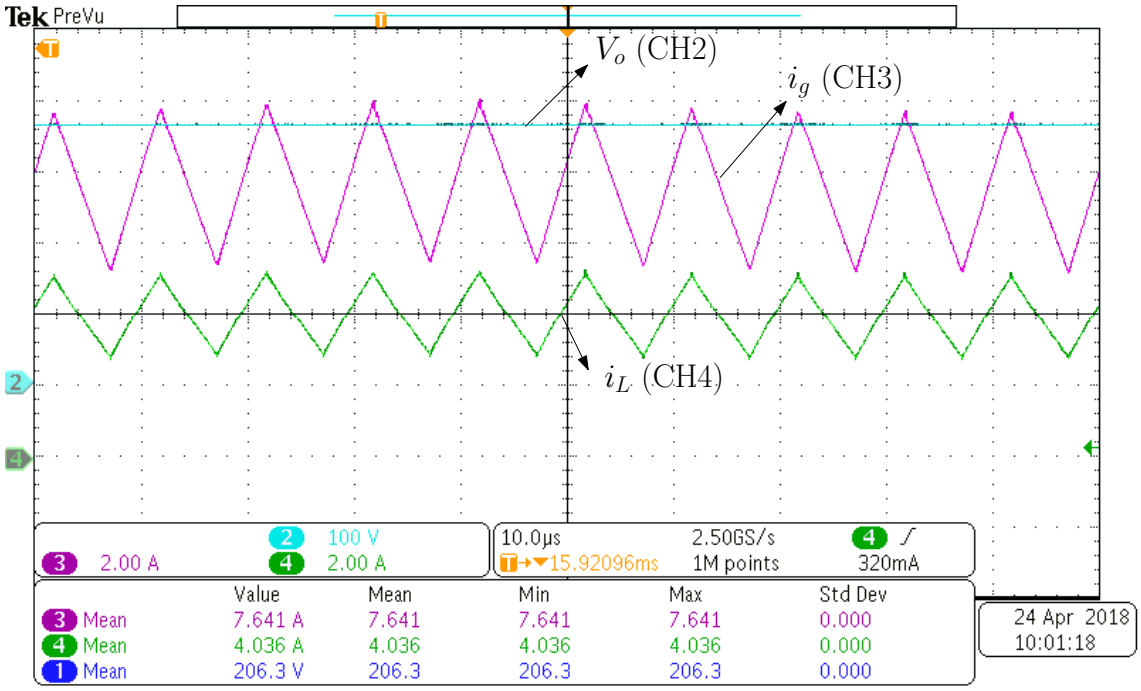

Figure **2-28**: Experimental results in boost mode with an active load of 90 Ω. CH3: input current i_g (2 A/div); CH4: output current i_L (2A/div); CH2: output voltage V_o (100 V/div); time base 10 us. Set input voltage 200 V.

Figure **2-29** shows the operation in buck mode with 350 V input and 200 V output voltage. The converter operates with 50 % duty cycle (D_2). The current ripples are according with the theoretical values, following the Table **2-7** in buck mode, the current ripple values are $\Delta i_L = 4.3$ A, and $\Delta i_g = 2.2$ A. Results of the converter operating in buck-boost mode is depicted in Figure **2-30**, where the duty cycle is of 95 % (D_2), input voltage 350 V and output voltage 330 V, the current ripples for this mode are $\Delta i_L = 0.96$ A, and $\Delta i_g = 0.5$ A, these values are similar to the theoretical values following the Table **2-7**.

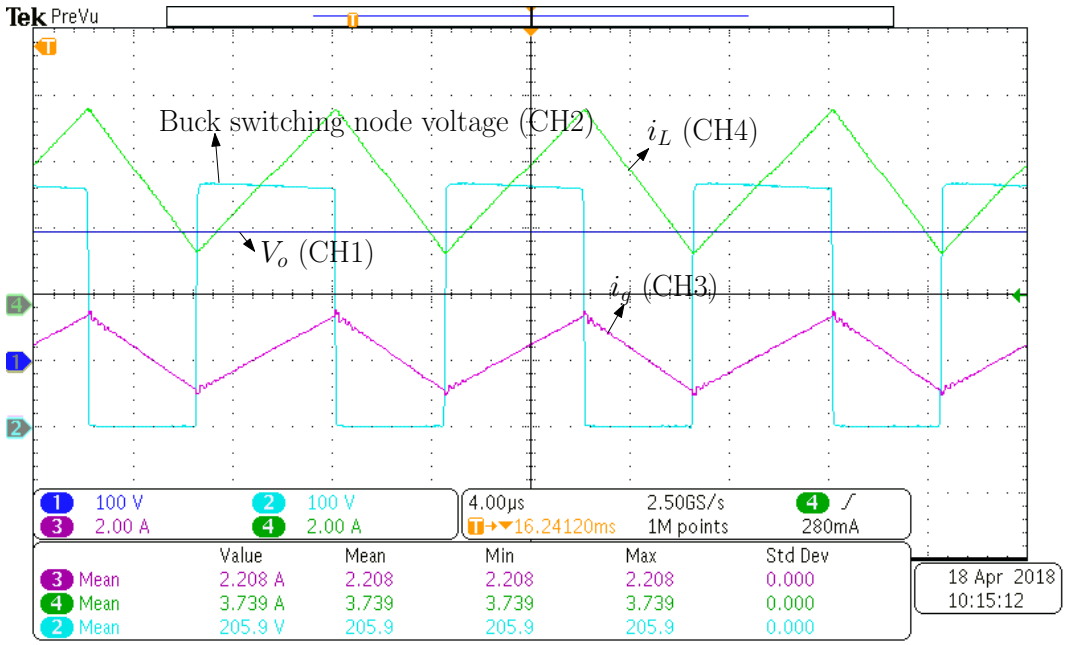

Figure **2-29**: Experimental results in buck mode with active load of 53 Ω. CH3: input current i_g (2 A/div); CH4: output current i_L (2A/div); CH2: switching node voltage (100 V/div); CH1: output voltage V_o (100 V/div). time base 4 us. Set input voltage 350 V.

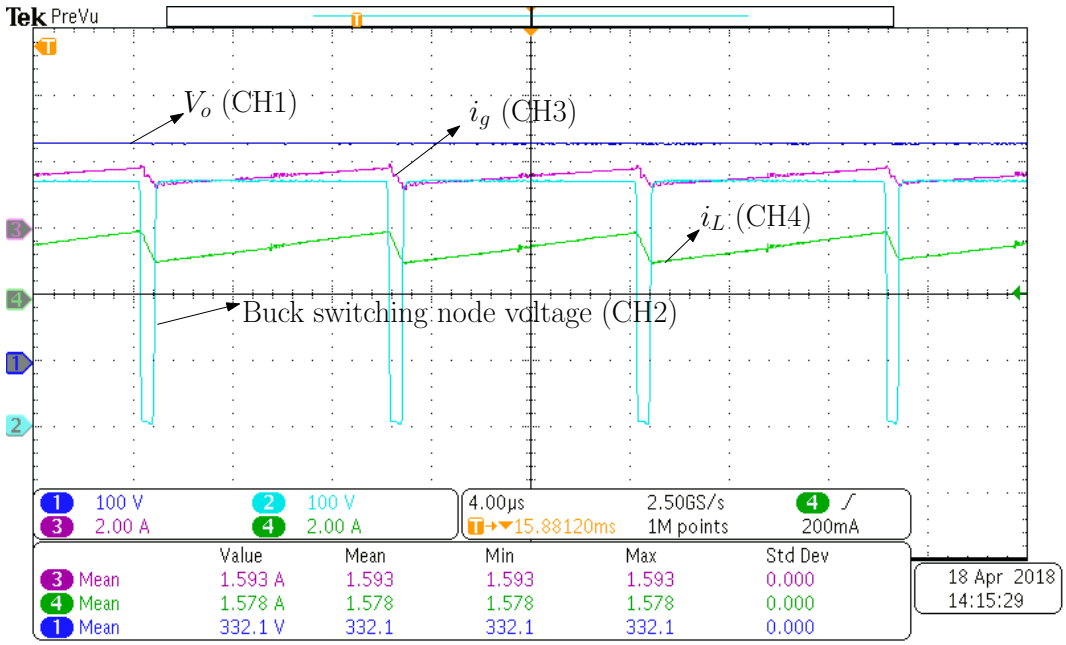

Figure **2-30**: Experimental results in buck-boost mode with active load of 210 Ω. CH3: input current I_g (2 A/div); CH4: output current I_L (2A/div); CH2: switching node voltage (100 V/div); CH1: output voltage V_o (100 V/div). time base 4 us. Set input voltage 350 V.

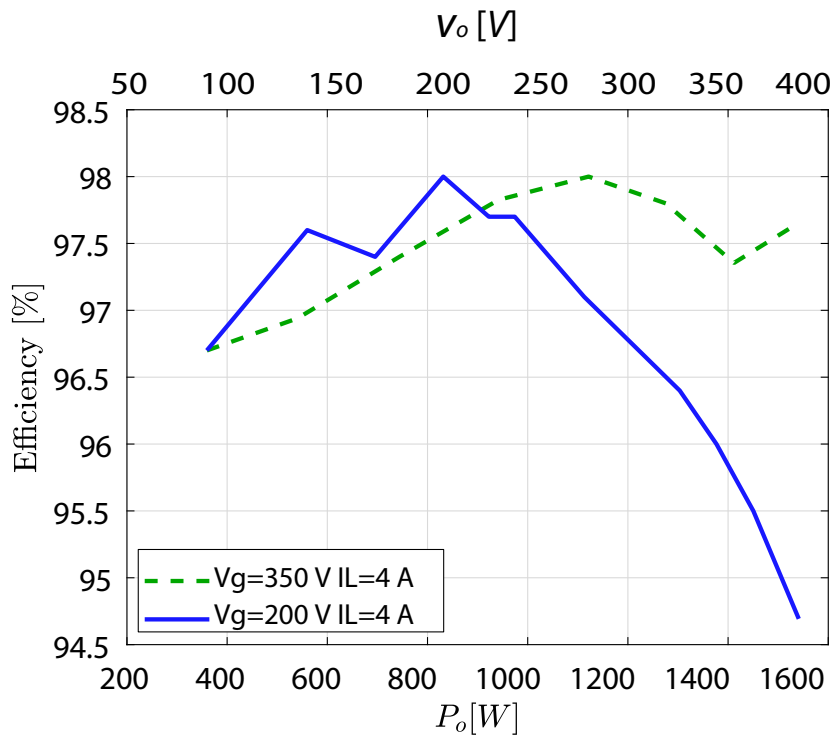

Figure **2-31**: Proposed buck-boost converter efficiency measurements with 200 V and 350 V at the input.

2.5.5 Efficiency analysis proposed bidirectional noninvertig buck-boost converter with coupled inductor.

The experimental efficiency obtained from the converter with coupled inductor ($k_3 = 0.5$, $N_1/N_2 = 1$, $N_1 = N_2 = 80$ turns) and operating at $I_L = 4$ A, for different output voltage are shown in Figure **2-31**. Where the power efficiency has been significantly increased respected to the converter buck-boost seen previously. The efficiency is compared with the results seen in the converter described in section 2.4 and this comparison is shown in Figure **2-32**. Power stage 1 (PS1) is the conventional bidirectional noninverting buck-boost and power stage 2 (PS2) is the proposed bidirectional noninverting buck-boost from Figure **2-1**, it is evident that the PS2 has less power loss than the PS1. The efficiency of PS2 is higher than 95% over all the range of power output and the maximum value is 98% near to $V_o = 220$ V when $V_g = 200$ V and near to $V_o = 300$ V when $V_g = 350$ V.

Table **2-9** shows the measurements of the winding-to-winding parasitic capacitance for different frequencies and with the structure of coupled inductor seen in Figure **2-27** right, it presents a very high reduction of its value ($C_p \approx 71$ pF) compared with the values seen in Table **2-5** for the converter seen in section 2.4. As expected, the voltage V_{gs} in the switch Q_2 (see Figure **2-1**) and the voltage in the boost switching node does not present oscillations due to the reduction of this parasitic capacitor as is shown in Figure **2-34**.

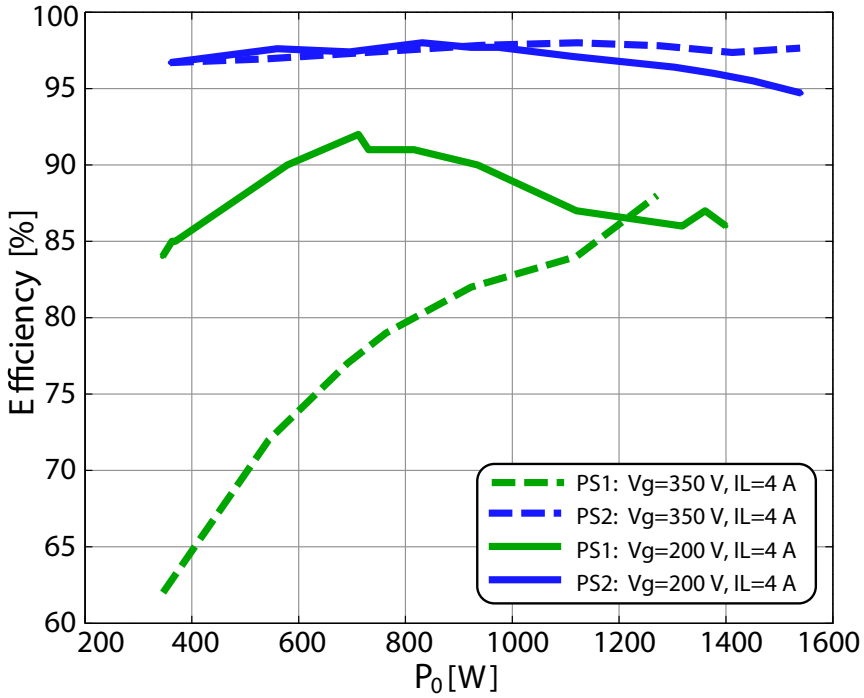

Figure **2-32**: Converter efficiency comparison of different converters with 200 V and 350 V at the input and $I_L = 4$ A.

Frequency [Hz]	Capacitance Wind1-Wind2 Value [F]
63095.7	7.6429E-11
89125.1	7.6448E-11
125892.5	7.1237E-11
177827.9	7.0040E-11
251188.6	7.2397E-11

Table **2-9**: winding-to-winding capacitance value for the structure of coupled inductor seen in Figure **2-27**.

Simulations in LTspice have been developed to roughly predict the power loss associated to the winding-to-winding parasitic capacitance of the coupled inductors. In addition to the previous capacitance values, the simulation uses the power stages with the parameters in Table **2-10**, an almost ideal switch (SW) with only on-resistance, and $V_o = 400$ V. Fig. **2-33** shows the simulated results of current and voltage across SW when the converter is working in boost mode. Fig. **2-33**(a) corresponds to PS1 with a parasitic capacitance of 15 nF connected between the b and d nodes (see Fig. **4-1**). Each switching period, the 15 nF

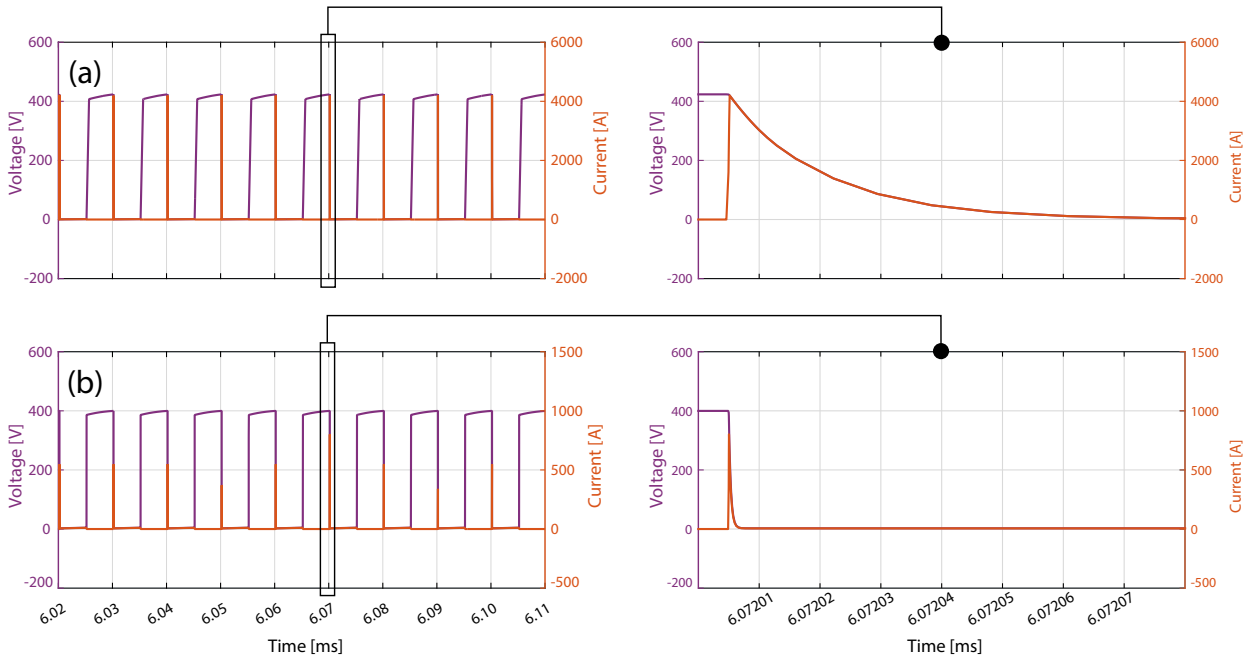

Figure **2-33**: Simulated results of current and voltage across the SW Q_2 for boost mode using LTspice. (a) Power stage 1; (b) power stage 2.

capacitor is discharged exponentially through the switch ($R_{on1} = 100$ mΩ, $T_{on} = 5$ μs) with a peak current near to 4 kA (400 V/R_{on}) in about 8 ns, with a simulated total power loss of 159 W. The switch current and voltage in Fig. **2-33**(b) correspond to PS2 with a 71 pF parasitic capacitor between the same nodes. Here, because of a larger on-resistance switch ($R_{on2} = 450$ mΩ), the current peak is reduced to 880 A. In spite of the larger on-resistance, the capacitor is discharged in just 160 ps, 50 times faster. The simulated power dissipated in PS2 is 32 W, mainly as conduction and damping resistor losses. In Figure **2-34**, the output current is 8 A, the input voltage is 200 V and the output voltage is 250 V, with the buck-boost converter with coupled inductor ($k_3 = 0.5$) it is possible to obtain a higher output current than the nominal current ($I_L = 4$ A), due to the reduction of the output current ripples in contrast to the PS1.

Common parameters	Value
Input voltage V_g	200-400 V
Output voltage V_o	100-400 V
Rated power	1.6 kW
Switching frequency $f_s = 1/T$	100 kHz
Output capacitor C_o	28 μF
Intermediate capacitor C	1.32 μF
Power Stage 1 parameters	**Value**
Magnetizing & primary self inductances $M = L_m = L_1$	285 μH
Secondary self inductance L_2	500 μH
Global coupling coefficient k_2	0.75
Damping network R_dC_d	10 Ω, 10 μF
Power Stage 2 parameters	**Value**
Mutual inductance $M = L_m$	135 μH
Self inductances $L_1 = L_2$	270 μH
Global coupling coefficient k_3	0.5
Damping network R_dC_d	5 Ω, 20 μF

Table **2-10**: Parameters for the buck-boost power stages 1 and 2.

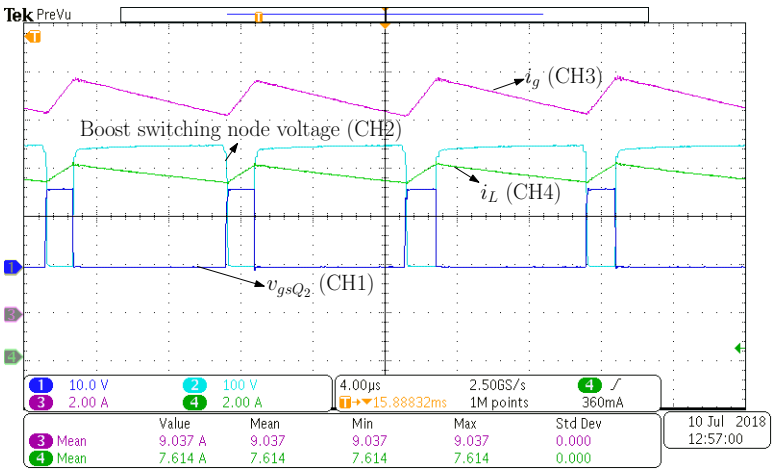

Figure **2-34**: Waveforms of the converter with coupled inductor ($k_4 = 0.5$). CH3: input current i_g (2 A/div); CH4: output current i_L (2A/div); CH2: Boost switching node voltage (100 V/div); CH1: v_{gsQ_2} (10 V/div). time base 4 us. Set input voltage 200 V, output voltage 250 V.

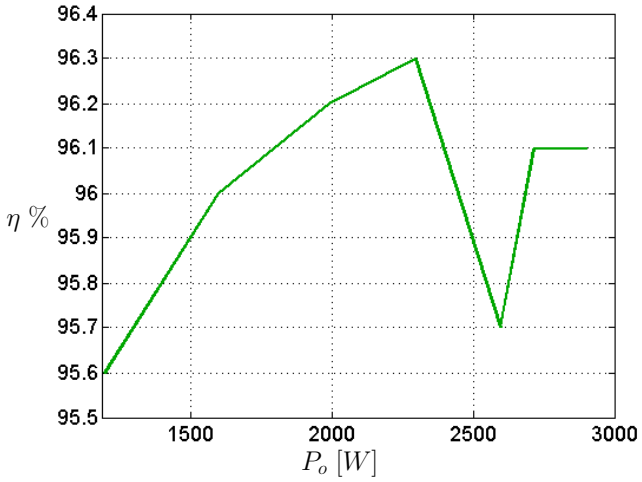

Figure **2-35**: Results of efficiency measurements for the proposed bidirectional dc-dc converter with output current 8 A, and input voltage 350 V.

The results of efficiency with respect to the power output with $I_L = 8$ A are shown in Figure **2-35** for the PS2. The measurement was made using an electronic active load (EA-EL9750-75HP), in resistance mode, setting the resistor value according with the output voltage desired to consume 8 A. With an input voltage value Vg = 350 V and testing different operating points through a sweep of output voltage from 150 V to 370 V, it can be observed that for the output voltage near to the input voltage, the percentage of efficiency has a reduction because the converter works in buck-boost mode and it has a high switching loss due that the four switches are working for this mode.

2.6 Transient voltage protection of high gate driver and MOSFETs

In order to eliminate the negative return spike in the high-side floating voltage supply of pin (HS) of the UCC27714 (high and low side) MOSFET driver, the recommendation exposed in [48] has been followed. Figure **2-36** shows input and output currents, and the intermediate node for each half-bridge MOSFETs, when the boost node is switching. Negative spike voltage can be seen. The UCC27714 driver has the ability to keep a logical operation with negative voltage up to -8 V on HS pin. Nonetheless, negative spike with values below this limit can cause erratic operation. Selecting a series gate resistor value of $R_1 = 10\ \Omega$, this value of resistor allows a high switch speed and a decrease of the amplitude of the negative spike. A fast power diode D1 is set between the HS and the COM pin, besides a resistor $R_2 = 5\ \Omega$ to limit the current across the diode. These elements are added to the basic schematic of MOSFET driver, as it is shown in Fig. **2-37** (a). On the other hand, for

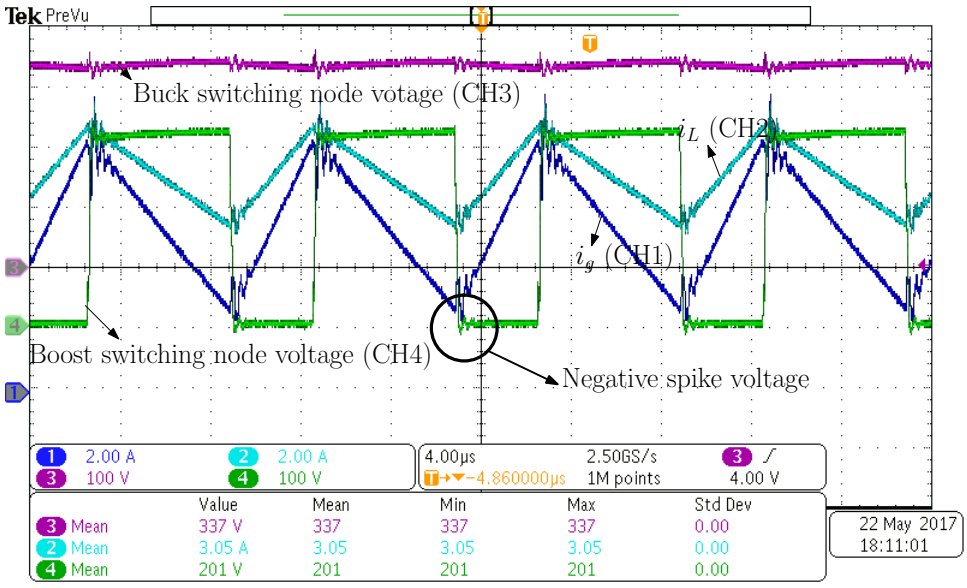

Figure **2-36**: Switching node voltage in power converter.

transient voltages on the Gate-Source MOSFET, a diode and a zener diode of 16 V are used, both connected in series to protect the MOSFET. Moreover, to limit the voltage in V_{gs}, $R = 47\ k\Omega$ was chosen. The schematic representation of this protection is shown in Fig. **2-37** (b).

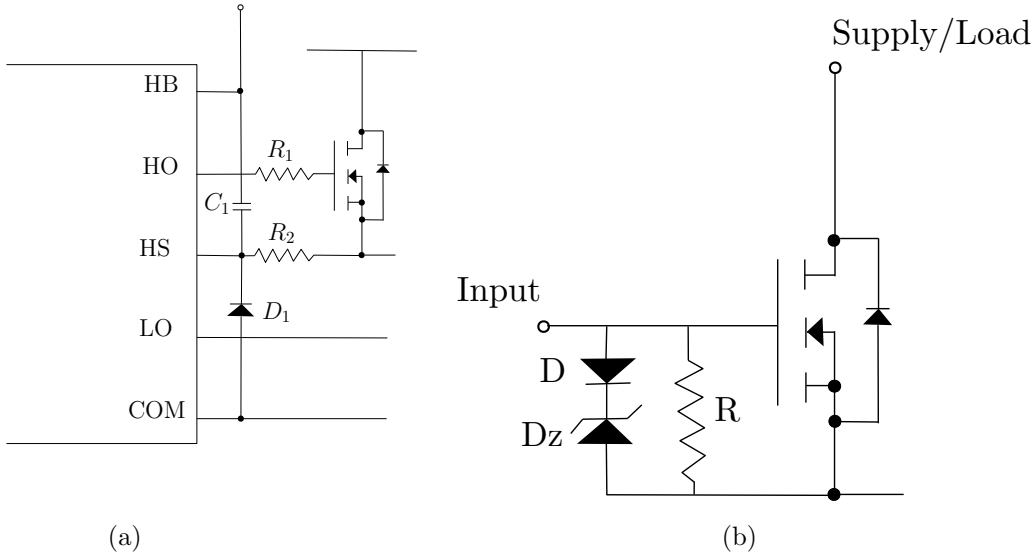

Figure **2-37**: Diagram of: (a) Circuit squematic driver (b) Transient voltage MOSFET protection.

2.7 Conclusion

In this chapter the noninverting bidirectional dc-dc converter with coupled inductor is analyzed for high voltage in which the dc-dc converter can operate in boost-mode or buck-mode with hard-switching at 100-kHz. Two 1.6-kW prototypes with an input voltage range of 200 V to 400 V, and output voltage between 100 V and 400 V at the output voltage have been built to verify that the pair of coupled inductors of the power stage that operates with the higher efficiency has the proposed coils arrangement that uses only one toroidal core, with a very low parasitic winding-to-winding capacitance and loose magnetic coupling. Adapting the power stage damping network to the new parameters of the loosely coupled inductors is straightforward. The analysis and experimental results demonstrate that the proposed converter is suitable for high efficiency, high step-up and step-down high voltage applications thanks to the use of SiC devices and the improved design of the coupled inductors.

3 Digital control for output voltage regulation of dc-dc converter

3.1 Abstract

The previous chapter verifies the efficiency and design of the proposed noninverting bidirectional buck-boost converter, this chapter presents the proposed dc-dc bidirectional buck-boost converter located between a battery pack and the inverter to regulate the dc bus in electric vehicle (EV) powertrain. The converter is based on the versatile buck-boost converter which in low voltage and hard-switching applications has shown a great performance in different topologies of fuel cell systems. Therefore, extending the use of the converter to higher voltage applications such as the EV is a challenge that will be addressed in this work. The use of a high-efficiency step-up/step-down converter, as in the case of the versatile converter, in an EV powertrain can improve the whole system efficiency for an extent range of electric motor (EM) speeds which comprises urban and highway driving cycles while allowing the operation under motoring and regeneration (regenerative brake) conditions. The proposed control corresponds to an outer voltage feedback loop and an inner current programmed controller using the digital signal controller (DSC) TMS320F28377S. Two different inner current programmed controllers where proposed which corresponds to a discrete-time sliding-mode current control (DSMCC) and a multisampled average current control (MACC). The theoretical analyses have been validated by means of simulations and experimental tests performed on a 400 V 1.6 kW purpose built-prototype.

3.2 Introduction

The control method implemented to regulate the conveter's output voltage of the Figure **3-1** is a two-loop digital control. This strategy allows smooth transitions between motoring and regenerative braking operations and also during the dc bus reference voltage changes. The control of the buck-boost converter presented in this chapter, operates according to the principles of conventional control strategies in a discrete domain time. The digital control has the advantage that it simplifies the implementation of complex functions, allows the implementation of a programmed soft start strategy of the converter, higher robustness to noise, and flexibility in design without the need to make many component or hardware changes [49].

The digital control proposed is based on an inner current programmed controller with an outer voltage feedback loop (PI compensator).

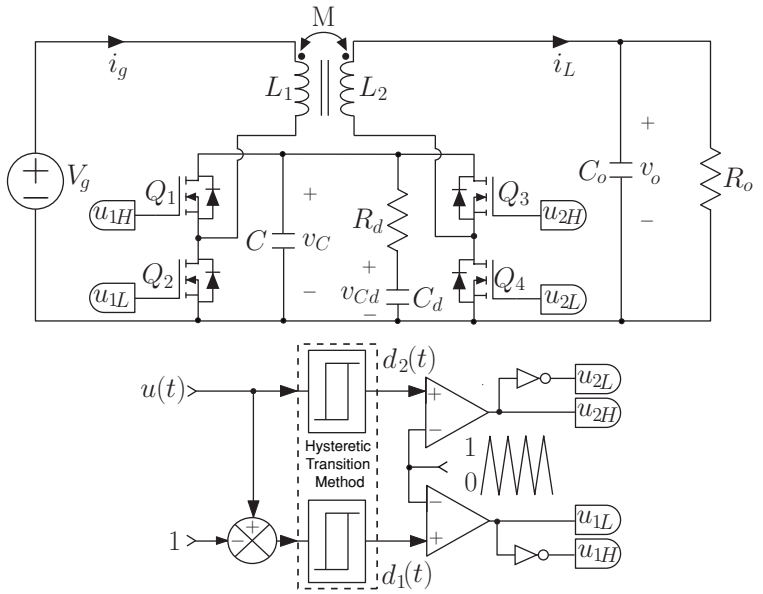

Figure **3-1**: Schemes of the buck-boost converter and its switch signals generation.

Figure **3-2** describes the converter connected to dc-link voltage with a current control loop. When a voltage loop is added in a current controlled converter, then the converter can be operated as a controlled current source, as is showed in Figure **3-3**. where the load current is equal to the reference current.

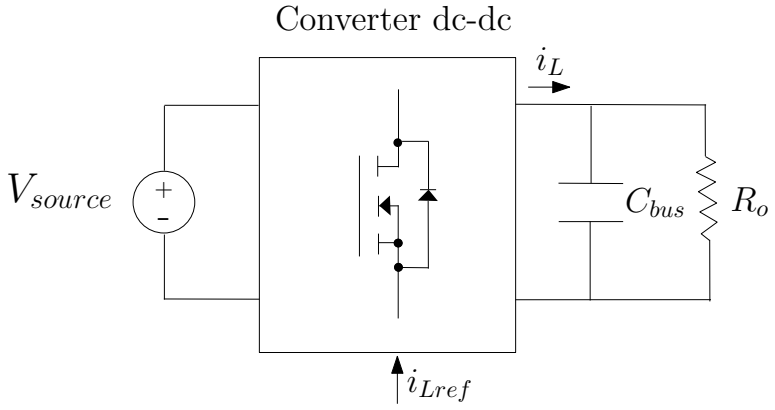

Figure **3-2**: Current controlled switching dc-dc converter connected to dc bus.

Then, the current controlled converter is operated as a current source used to driver the energy consumption of the load. From the point of view of the dc voltage control loop,

voltage variations with power constant load should be compensated by charge or discharge of bus capacitor [50].

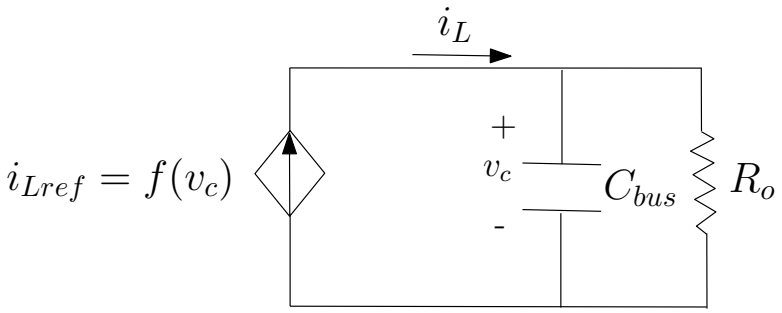

Figure **3-3**: Controlled current source converter model.

The converter scheme depicted in Figure **3-1** is composed by two half bridge MOSFETs, an R_dC_d damping network connected in parallel with the intermediate capacitor C, a constant input-voltage V_g, and a resistance load R_o. In addition, the coupled inductor has an unitary ideal turns ratio $N_1/N_2 = 1$, a coupled coefficient $k = 0.5$, a mutual inductance M and the primary self-inductance L_1 equal to the secondary self-inductance L_2 ($L = L_1 = L_2$). In the analysis, a CCM operation is considered, no parasitic effects and a switching frequency much higher than the converter's natural frequencies. The use of SSA method to model the converter leads to the following set of differential equations [44]:

$$\frac{di_g(t)}{dt} = \frac{L(V_g - v_c(1-u_{1L})) - M(v_o - v_c u_{2H})}{L^2 - M^2} \tag{3-1}$$

$$\frac{di_L(t)}{dt} = \frac{M(V_g - v_c(1-u_{1L})) - L(v_o - v_c u_{2H})}{L^2 - M^2} \tag{3-2}$$

$$\frac{dv_c(t)}{dt} = \frac{1}{C}\left(-i_L u_{2H} + i_g\left(-u_{1L}+1\right) - \frac{1}{R_d}\left(v_c - v_{cd}\right)\right) \tag{3-3}$$

$$\frac{dv_{cd}(t)}{dt} = \frac{v_c - v_{cd}}{C_d R_d} \tag{3-4}$$

$$\frac{dv_o(t)}{dt} = \frac{i_L}{C_o} - \frac{v_o}{R_o C_o} \tag{3-5}$$

The aim of this analysis is to find the converter's current output slope $\frac{di_L}{dt}$ in each operation mode (buck or boost) to design the digital inner current programmed controllers. The output current has a periodic triangular waveform where the current rises with a slope of m_1 and falls with a slope $-m_2$. Table **3-1** presents the converter output current waveform slopes based on (3-2) for the boost and buck modes.

In this chapter, the implementation and comparison of two digital control strategies for the inner loop which are the multisampled average current control (MACC) and the discrete-time

Mode	m_1	$-m_2$
Buck	$\frac{M(V_g - v_c) - L(v_o - v_c)}{L^2 - M^2}$	$\frac{M(V_g - v_c) - Lv_o}{L^2 - M^2}$
Boost	$\frac{MV_g - L(v_o - v_c)}{L^2 - M^2}$	$\frac{M(V_g - v_c) - L(v_o - v_c)}{L^2 - M^2}$

Table **3-1**: Slope of the output current waveform

sliding-mode current control (DSMCC) are presented. Both control strategies will be briefly explained in the following sections as also the voltage PI compensator. As well, simulations and experimental results of both current control techniques under startup, small and large variations and using an EV emulator are presented and discussed.

3.3 Multisampled average current control

The MACC was introduced for the low-voltage bidirectional buck-boost converter in [43]. The schematic diagram of the two-loop control using MACC method is depicted in Figure **3-4**. The aim of the controller is to obtain the variable control u for the output voltage regulation, were the external loop provides the reference of the output current using a discrete proportional-integral control transfer function $G_{vpi}(z)$. In this method, a ripple filter is used to control the samples of the output current $i_L[n]$ to their desired reference $i_{Lref}[n-1]$. The ripple filter produces the average of current error values corresponding to two samples per switching period ($f_{samp} = 2f_s$). The expression for the ripple filter in the z-domain can be represented as follows

$$G_f(z) = K_p \left(1 + \frac{K_a}{4}\frac{z+1}{z-1}\right)\left(1 - z^{-2}\right) \tag{3-6}$$

where the value of the constant K_a is 2. This value is suggested to avoid rounding error in case of use integer representation in the controller variables [51]. The resulting expression for the ripple filter replacing the value of K_a and collecting terms is

$$G_f(z) = K_p \left(\frac{3}{2} + \frac{1}{z} - \frac{1}{2z^2}\right). \tag{3-7}$$

This ripple filter transfer function can be expressed as a difference equation as

$$\hat{u}[n] = \frac{K_p}{2}\left(3e_i[n] + 2e_i[n-1] - e_i[n-2]\right). \tag{3-8}$$

The proportional gain can be written in terms of the output current waveform slopes shown in Table **3-1** as

$$K_p = \frac{K_n}{(m_1 + m_2)T} \tag{3-9}$$

where T is the switching period $(1/f_s)$ and the expression m_1+m_2 is obtained from Table **3-1** for each converter operation mode, yielding

$$m_1 + m_2 = \begin{cases} \frac{MV_c}{L^2-M^2} & \text{for boost mode} \\ \frac{LV_c}{L^2-M^2} & \text{for buck mode.} \end{cases} \tag{3-10}$$

The parameter K_n was adjusted to 0.35 to obtain a crossover frequency (CF) value of approximately 11 kHz as in [43]. A digital PI compensator in the z-domain is added to the current control loop and it is implemented using forward-Euler method as follows

$$G_{pi}(z) = 1 + \frac{K_i}{2}\frac{1}{z-1} \tag{3-11}$$

Figure **3-4** shows the previous compensator PI in the discrete-time, where the integral gain can be chosen as in [43], hence the value for $K_i = 0.16$ was selected.

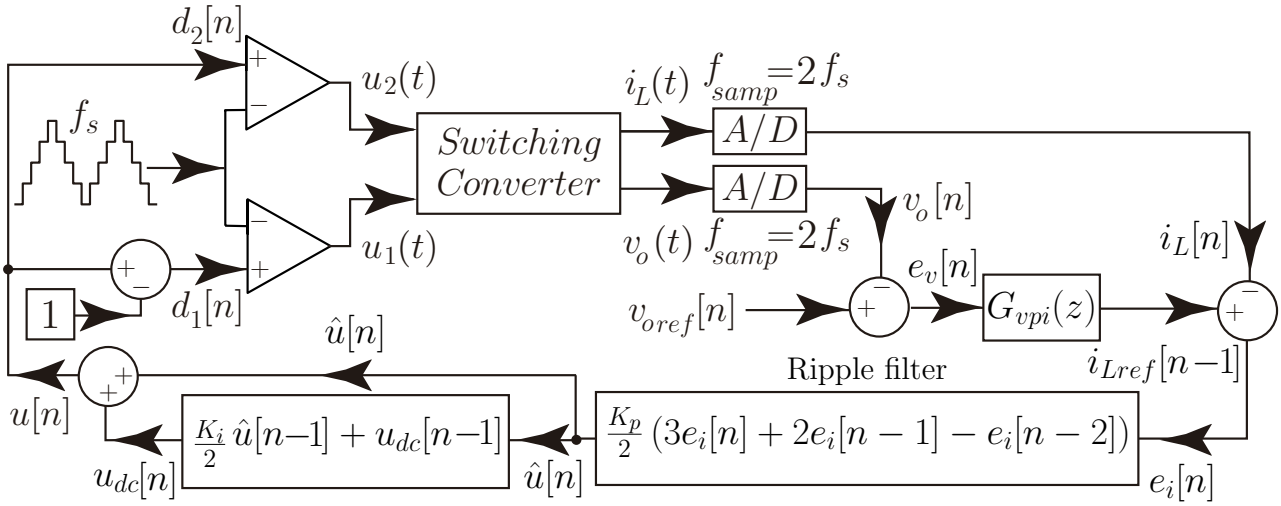

Figure **3-4**: Schematic diagram of the two-loop control using MACC method.

3.4 Discrete-time sliding-mode current control

A DSMCC was presented for a boost converter [52] and a buck converter [53] and in this work, this method is used for the bidirectional versatile buck-boost converter. The aim of the DSMCC is to compute the variable control $u[n]$ in the n-th time sample period that ensures the control surface (3-12) is reached in the next sampling period ($f_{samp} = f_s$).

$$s[n] = i_{Lref}[n-1] - i_L[n]. \tag{3-12}$$

The Euler approximation leads to the following discrete-time output current expression, assuming the averaged model that the converter's current output slope $\frac{di_L}{dt} \approx \frac{iL[n+1]-iL[n]}{T}$

$$i_L[n+1] = i_L[n] + T(m_1+m_2)d_x[n] - m_2T. \tag{3-13}$$

Hence, the resulting expression of the duty cycle is

$$d_x[n] = \frac{1}{(m_1+m_2)T}[i_{Lref}[n] - i_L[n]] + \frac{m_2}{m_1+m_2} \tag{3-14}$$

where x in (3-14) and (3-13) corresponds to the operating mode of the bidirectional buck-boost converter ($x = 1$ for boost mode, $x = 2$ for buck mode), and $i_{Lref}[n] = i_L[n+1]$, using the expressions for m_1 and $-m_2$ for the output current slopes from Table **3-1** in (3-14), the expression for $m_1 + m_2$ is seen in (3-10) and for $m_2/(m_1 + m_2)$ is given by

$$\frac{m_2}{m_1+m_2} = \begin{cases} \frac{-M(V_g - v_c[n] + L(v_o[n] - v_c[n]))}{Mv_c[n]} & \text{for boost mode} \\ \frac{-M(V_g - v_c[n]) + Lv_o[n]}{Lv_c[n]} & \text{for buck mode.} \end{cases} \tag{3-15}$$

To guarantee that the system convergence, the following conditions must be fulfilled

$$s[n+1] < 0 \textbf{ if } \Delta s[n+1] > 0 \tag{3-16}$$

$$s[n+1] > 0 \textbf{ if } \Delta s[n+1] < 0 \tag{3-17}$$

where $\Delta s[n+1] = i_L[n+1] - i_L[n] = T(m_1+m_2)d_x[n] - m_2T$. In the case when $s[n+1] < 0$, the duty cycle is saturated to 0. For boost mode the analysis must be done with $d_1[n] = 0$,

$$\Delta s[n+1] = \frac{TM(v_o[n] - V_g)}{L^2 - M^2} > 0 \tag{3-18}$$

when $v_c[n] = v_o[n]$, being $V_o > V_g$. For buck mode $d_2[n] = 0$, therefore

$$\Delta s[n+1] = \frac{TLv_o[n]}{L^2 - M^2} > 0 \textbf{ when } \mathbf{v_c[n] = V_g}. \tag{3-19}$$

For the case when $s[n+1] > 0$, the duty cycle is saturated to 1. For boost mode $d_1[n] = 1$,

$$\Delta s[n+1] = \frac{-TMV_g}{L^2 - M^2} < 0 \textbf{ when } \mathbf{v_c[n] = v_o[n]}. \tag{3-20}$$

For buck mode $d_2[n] = 1$,

$$\Delta s[n+1] = \frac{TL}{L^2 - M^2}(v_o[n] - V_g) < 0 \tag{3-21}$$

when $v_c[n] = V_g$, being $V_g > V_o$ for buck mode. The previously analysis ensures the convergence to the switching surface.
The stability of the DSMCC dynamics can be demonstrated by the internal dynamics of the zeros transfer function used to design of the damping network of proposed power stage 2 seen in chapter 2.
In this control method, the output current $i_L(t)$ and voltages are sampled at the beginning of each switching period, then at the end of the switching cycle $i_L[n] = i_{Lref}[n-1]$. The steady-state duty cycle from the equivalent control law (3-14) can be obtained by substituting the voltage of the intermediate capacitor v_c by V_g for buck mode and by $v_c = V_o$ for boost mode in (3-15). When the In steady-state the duty cycle is $U = m_2/(m_1 + m_2)$, thus the variable control $u[n]$ can be written as

$$u[n] = \frac{1}{(m_1 + m_2)T} \left(i_{Lref}[n-1] - i_L[n]\right) + U_n \tag{3-22}$$

where $U_n = U$ for buck mode and $U_n = 1 + U$ for boost mode. The schematic diagram of the DSMCC is depicted in Figure **3-5**.

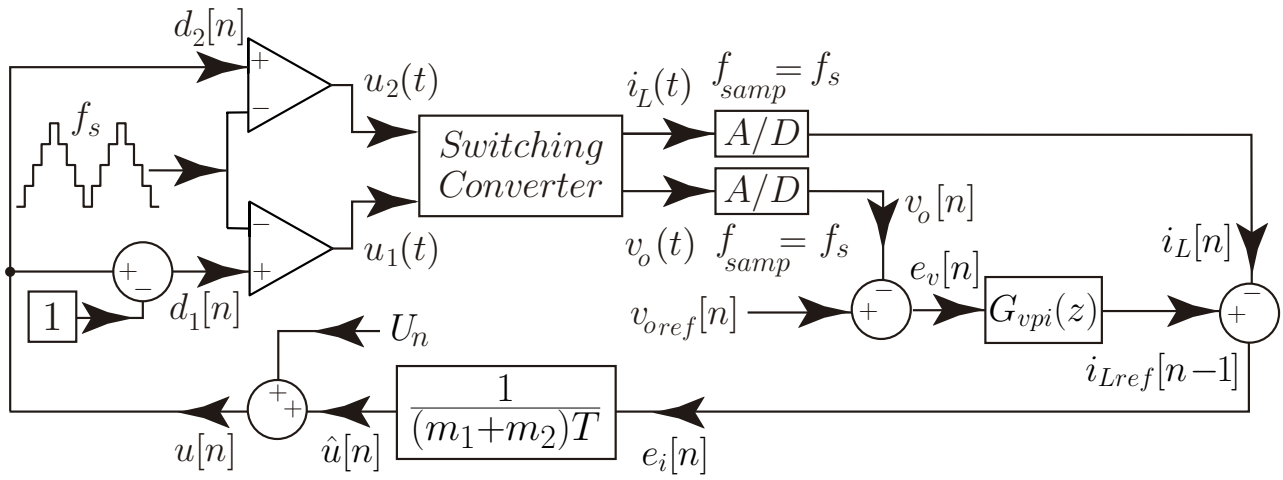

Figure **3-5**: Schematic diagram of the two-loop control using DSMCC method.

3.5 Digital Proportional-Integral voltage control

In order to satisfy the stability of the closed loop system, it is necessary to include an external and slower outer voltage loop with the inner current loop. With this new loop, the switching converter can be operated as a controlled current source when the load current follows the current reference. Therefore, the current controlled buck-boost converter is operated as a

current source that allows to drive the energy consumption of the load as is shown in Figure **3-3**. From the point of view of the dc voltage control loop, voltage variations with power constant load should be compensated charging or discharging the dc bus capacitor [50]. Hence, this PI control is designed taken into account the filter output capacitor value C_o or the capacitor in the dc-link for an EV powertrain C_{bus}. The transfer function of the PI voltage controller in the Laplace domain can be written as follows

$$G_{vpi}(s) = K_{pv} + \frac{K_{iv}}{s}. \tag{3-23}$$

To obtain the transfer function from the output current to the output voltage in the Laplace domain, the differential equation (3-5) is used, one obtains

$$H_{voiL}(s) = \frac{v_o(s)}{i_L(s)} = \frac{R_o}{R_o C_o s + 1} \tag{3-24}$$

The loop-gain of the external closed loop voltage can be written as:

$$G(s) = H_{voiL}(s) G_{vpi}(s) H_v(s) e^{-sT_m}, \tag{3-25}$$

where $H_v(s)$ is the measurement system gain, in other words, it is the gain of the closed loop for the sampled variables (v_o and i_L). The term e^{-sT_m} represents half switching cycle delay, $T_m = T/2$. Then the controller transfer function (3-23) can be expressed in the z domain using the forward Euler method, as follow

$$G_{vpi}(z) = K_{pv} + \frac{K_{iv} T_{samp}}{z - 1} z^{-1}. \tag{3-26}$$

Where $T_{samp} = 1/f_{samp}$. The forward-Euler method is used to find the recurrence equation for the discrete-time integral PI control

$$\begin{aligned} i_{Lp}[n] &= K_{pv} e_v[n] \\ i_{Li}[n] &= K_{iv} T_{samp} e_v[n] + i_{Li}[n-1] \\ i_{Lref}[n] &= i_{Lp}[n] + i_{Li}[n]. \end{aligned} \tag{3-27}$$

where

$$K_{pv} = C_o 2\pi f_c \tag{3-28}$$

$$K_{iv} = \frac{K_{pv}}{T_i} \tag{3-29}$$

The value of the crossover frequency (CF) for the voltage loop (f_c) should be lower than the CF for the current loop. Hence, a $f_c = 2500$ Hz was selected for the voltage feedback loop. The location of the PI zero should be lower than f_c ($1/(2\pi T_i) < f_c$) whereby a $T_i = 1.5 \times 10^{-4}$ s was selected.

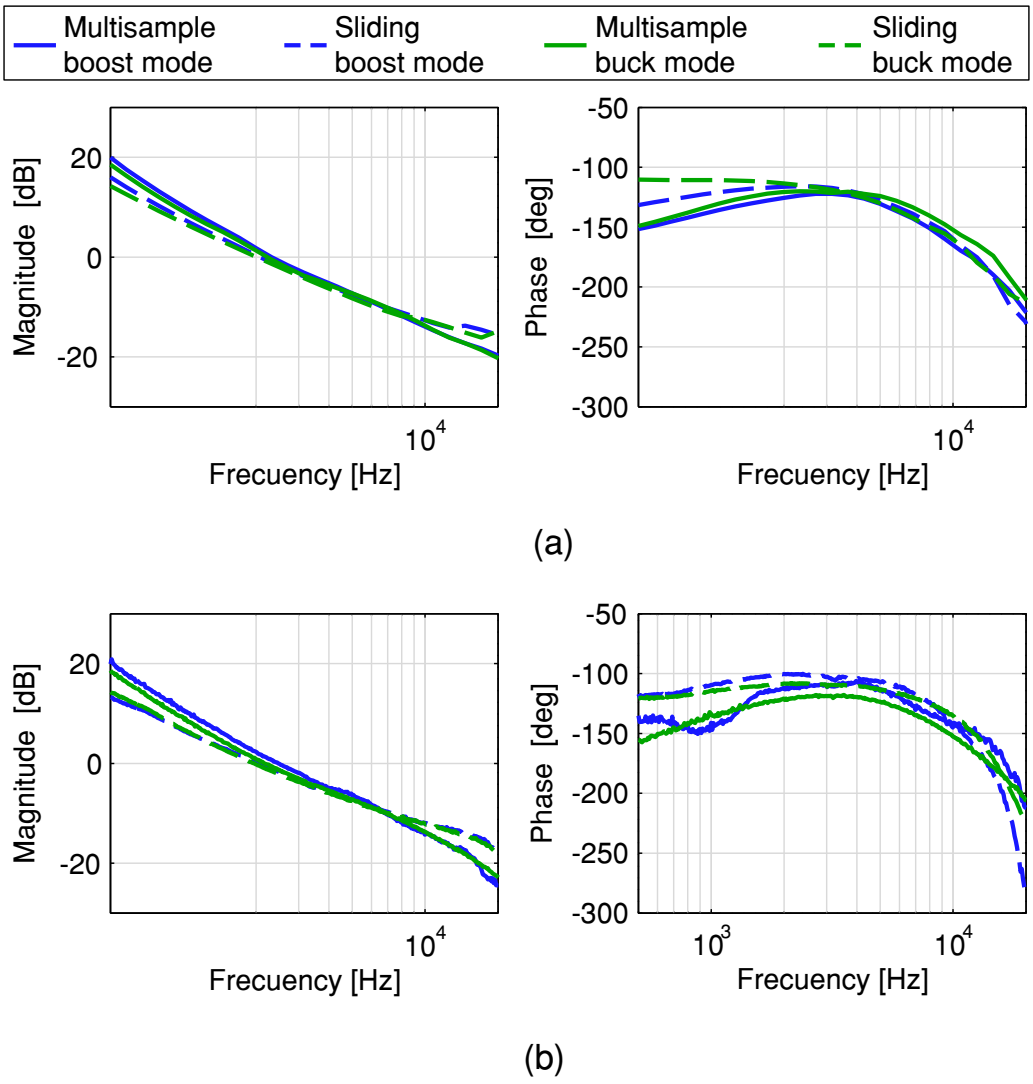

Figure **3-6**: Voltage loop gain Bode plots of the buck-boost converter: (a) Simulated, (b) Experimental.

Figure **3-6** depicts the Bode plots of simulated (PSIM) and experimental voltage loop gain under different operation modes (boost and buck) with the parameters of the converter listed in Table **3-3** and a gain of the measurement system $H_v(s) = 0.044$. These Bode plots show a similar behaviour at low frequency of the magnitude plot both for the experiment and the simulation. However, at high frequencies some differences can be seen, which can be attributed to not modeled parasitic elements in the simulation. For a quantitative evaluation of the compared inner control methods and their outer voltage loop for each converter's operation mode, the CF and the phase margin (PM) are listed in Table **3-2**. From this table it can be concluded that both inner control methods show similar results and the PMs

indicate that the closed loop system is stable for all cases with a some more phase margin and a litter less bandwidth for DSMCC method.

Inner control method		Simulated		Experimental	
		CF [kHz]	PM [deg]	CF [kHz]	PM [deg]
Multisample ($f_{samp} = 200$ kHz)					
	boost mode	2.32	56.41	2.44	69.31
	buck mode	2.32	59.95	2.16	59.58
Sliding ($f_{samp} = 100$ kHz)					
	boost mode	1.99	63.79	2.03	79.4
	buck mode	1.99	66.52	1.94	71.2

Table **3-2**: CF and PM of voltage loop gain

3.6 Simulation and experimental results

Validation of the proposed current control strategies was performed on a 1.6 kW versatile buck-boost converter. A Texas Instruments TMS320F28377S Digital Signal Controller (DSC) is used to implement the proposed control algorithms to calculate the variable control u, and the hysteretic buck-boost transition method introduced in [42], which was employed to compute the duty cycles values. These duty cycles allow the generation of the PWM by means of a symmetric triangular signal to get the activate signals of the MOSFETs switches. In addition, a direct voltage source AMREL SPS800X13-K02D is used as power supply for the input voltage of the buck-boost converter shown in Figure **3-1** and whose parameters are listed in Table **3-3**.

3.6.1 System Startup

The simulated and experimental results for the system startup in closed loop are given in Figures **3-7** and **3-8**. The voltage reference V_{oref} is increased from 0 V in each switching period during 12 ms until 293 V with an input voltage (V_g) of 200 V and 350 V for boost and buck mode, respectively. It must also be noted that during the startup in boost mode the system begins in buck mode and ends in boost mode in steady state. The experimental results demonstrate that the voltage output is well regulated in all the operation modes with both tested control strategies. In addition, a good agreement can be observed between the experimental measurement and the simulated with a fast and soft-startup.

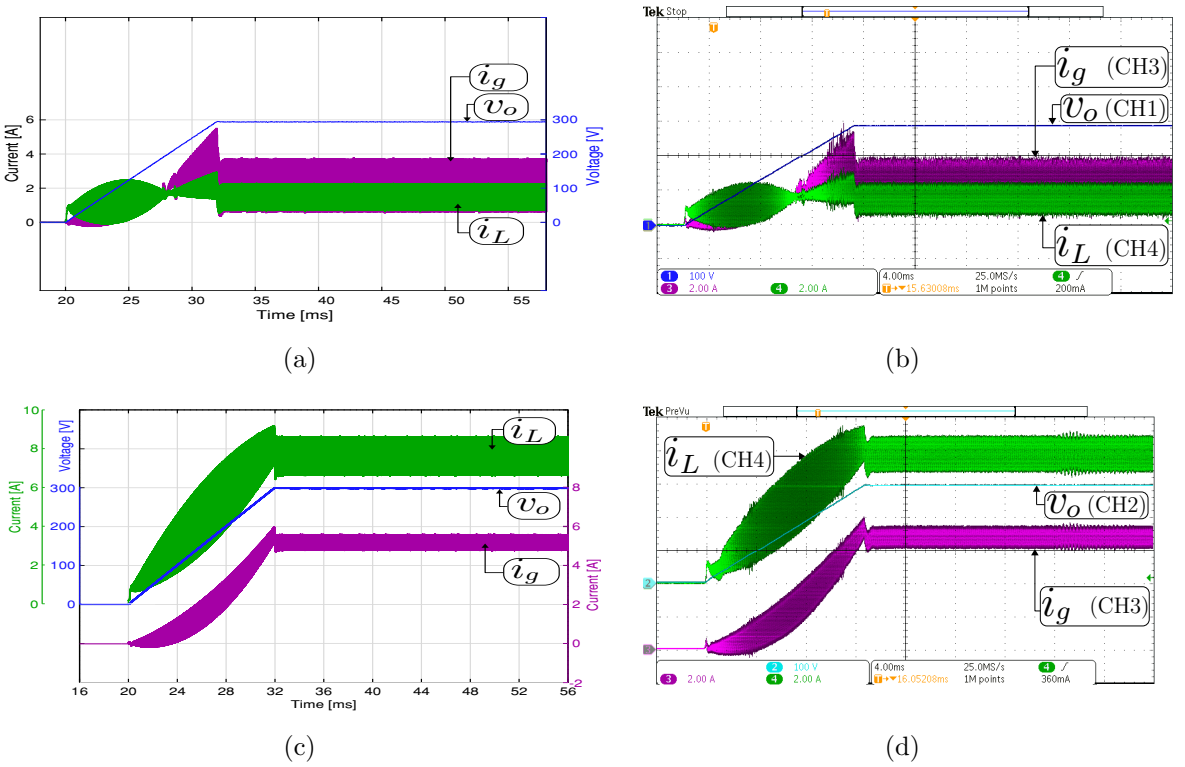

Figure **3-7**: System startup with a constant resistive load. Multisampled: Simulated (a), (c) and experimental (b), (d) Two operation modes in steady-state are shown: (a), (b) boost mode (V_g = 200 V, v_o = 293 V and and R_o = 200 Ω) and (c), (d) buck mode (V_g = 350 V, v_o = 293 V and R_o = 32.3 Ω). CH1 or CH2: v_o (100 V/div), CH3: i_g (2 A/div), CH4: i_L (2A/div), and time base of 4 ms.

3.6.2 Small-signal response to output voltage reference variation

Figures **3-9** and **3-10** show the small-signal control loop response to small output voltage reference changes during the boost and buck operation, respectively. For all the study cases the input voltage is set at 200 V with a constant resistive load R_o = 200 Ω. For boost mode (Figure **3-9**), the output voltage reference has been changed between the values of 294 V and 296 V. While in buck mode, the output voltage reference changes between the values of 98 V and 100 V as shown in Figure **3-10**. The dc component in Figure **3-9** and **3-10** has been removed to comprise the ± 2 V step change in the output voltage reference. These results show that the output voltage is well regulated to its desired reference and the output and input current are incremented or decremented when the voltage reference changes to recover the converter's operating point. The figures also demonstrate a good agreement between the experimental and simulation results with a short outer voltage transient response around of 400 μs, which validates the adequate operation of both proposed control methods.

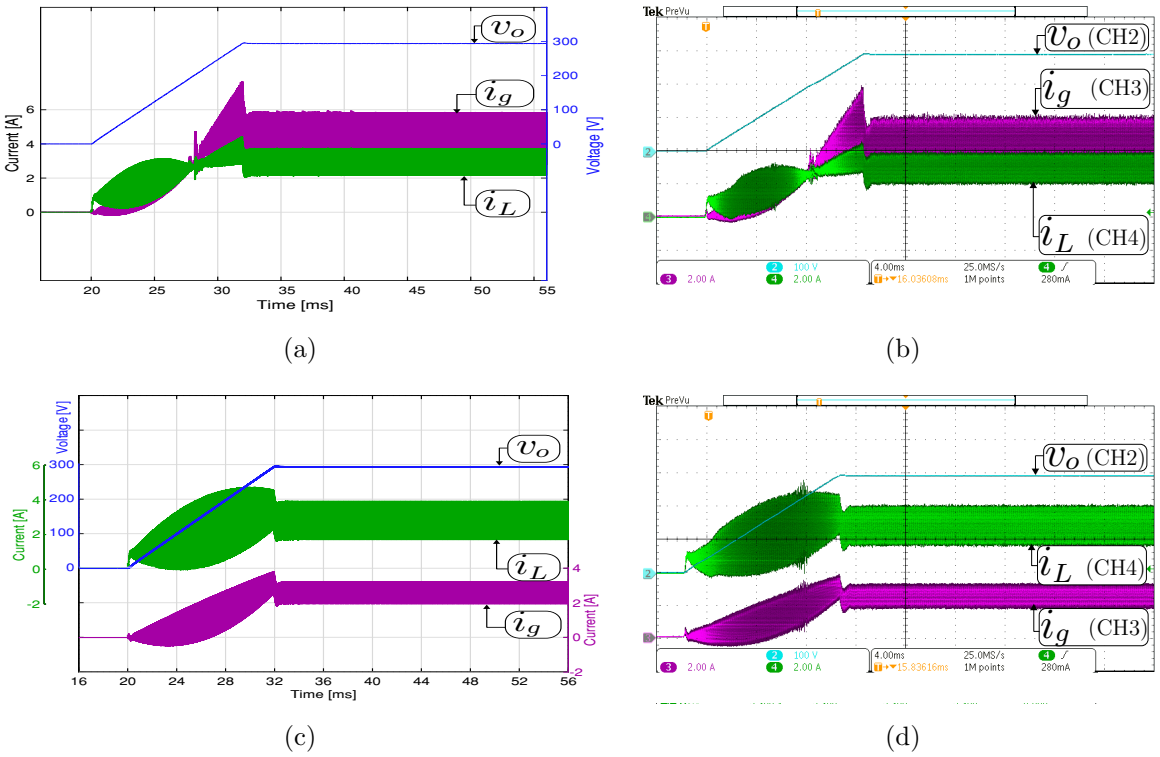

Figure **3-8**: System startup with a constant resistive load. Sliding: Simulated (a), (c) and experimental (b), (d) Two operation modes in steady-state are shown: (a), (b) boost mode ($V_g = 200$ V, $v_o = 293$ V and and $R_o = 100\ \Omega$) and (c), (d) buck mode ($V_g = 350$ V, $v_o = 293$ V and $R_o = 100\ \Omega$). CH1 or CH2: v_o (100 V/div), CH3: i_g (2 A/div), CH4: i_L (2A/div), and time base of 4 ms.

3.6.3 Large-signal response to output voltage reference variation

Figures **3-11** and **3-12** compare the large-signal response when the output voltage has a $\pm$ 20 V step change for both control strategies. The Figures show simulation and experimental waveform of the input and output current, and output voltage. Figure **3-11** depicts the response when the converter operates in boost mode and the output voltage reference has been changed between the values of 293 V and 313 V. The dc component in the experimental and simulation results have been removed to appreciate the output voltage variation in boost mode. The results for buck mode are shown in Figure **3-12** where the output voltage reference has been changed between the values of 100 V and 120 V. From these figures, for both control methods, the transient average current output value was successfully limited to $\pm$ 4 A, which is the rated output current of the converter. These results confirm the direct relation between the output voltage response time with the output filter capacitor value. It should be remembered that the slew-rate (SR) is defined in this case as $SR = i/C_o$ [V/μs] where i is the instantaneous current through the capacitor C_o. Therefore, the response time

Parameter	Value or type
Input voltage V_g	200-400 V
Output voltage V_o	100-400 V
Rated Power	1.6 kW
Output capacitor C_o	28 μF
Damping capacitor C_d	20 μF
Intermediate capacitor C	1.32 μF
Mutual inductance coupled inductor M	135 μH
Self inductance coupled inductor $L_1 = L2$	270 μH
Damping resistance	5 Ω
Switching frequency f_s	100 kHz
Power semiconductors $Q_1 - Q_4$	SCT2450KEC

Table **3-3**: Parameters for the buck-boost converter.

to step output variation depends of the SR parameter. Note that the measured current i_L follows accurately the current reference for both control methods. Some differences are presented between the simulated and experimental results with respect to the input current. These differences are because this current is not controlled by the converter and its dynamic depends on the dc power supply internal control. Again, a good agreement between the experimental and simulation results is observed. It can be also observed in figures **3-11** and **3-12** the negative value of i_L in some transient responses, thus verifying again the bidirectional behaviour of the designed converter.

3.6.4 Experiments with an EV powertrain system emulation

Nowadays, electric vehicle is of great interest for the scientific community. Principally, for their many advantages such as reduction of carbon dioxide emission, improved efficiency and performance [54]. The traction motor used in EV are mainly induction or permanent magnet synchronous machines [46]. Energy management system in auxiliary supply in EV [55, 56], EV topologies [57] and the use of dc-dc converter as interface between the main energy source in an EV powertrain [58] are some of the applications for EVs, and this applications can be studied using a powertrain system emulation or simulation. In [59] a bidirectional buck-boost converter topology is used to emulate a regenerative controllable dc load. This converter allows simulate the power required by the powertrain and speed profiles, as these are seen from the high-voltage dc bus. Taking into account the friction between the tires and the road. This emulator can be used to develop experiments in EV applications with a power controllable in the range of [-3, 3] kW. An EV Hardware-in-the-Loop (HIL) platform is introduced in [60], generally this kind of platform is based in hardware components of an

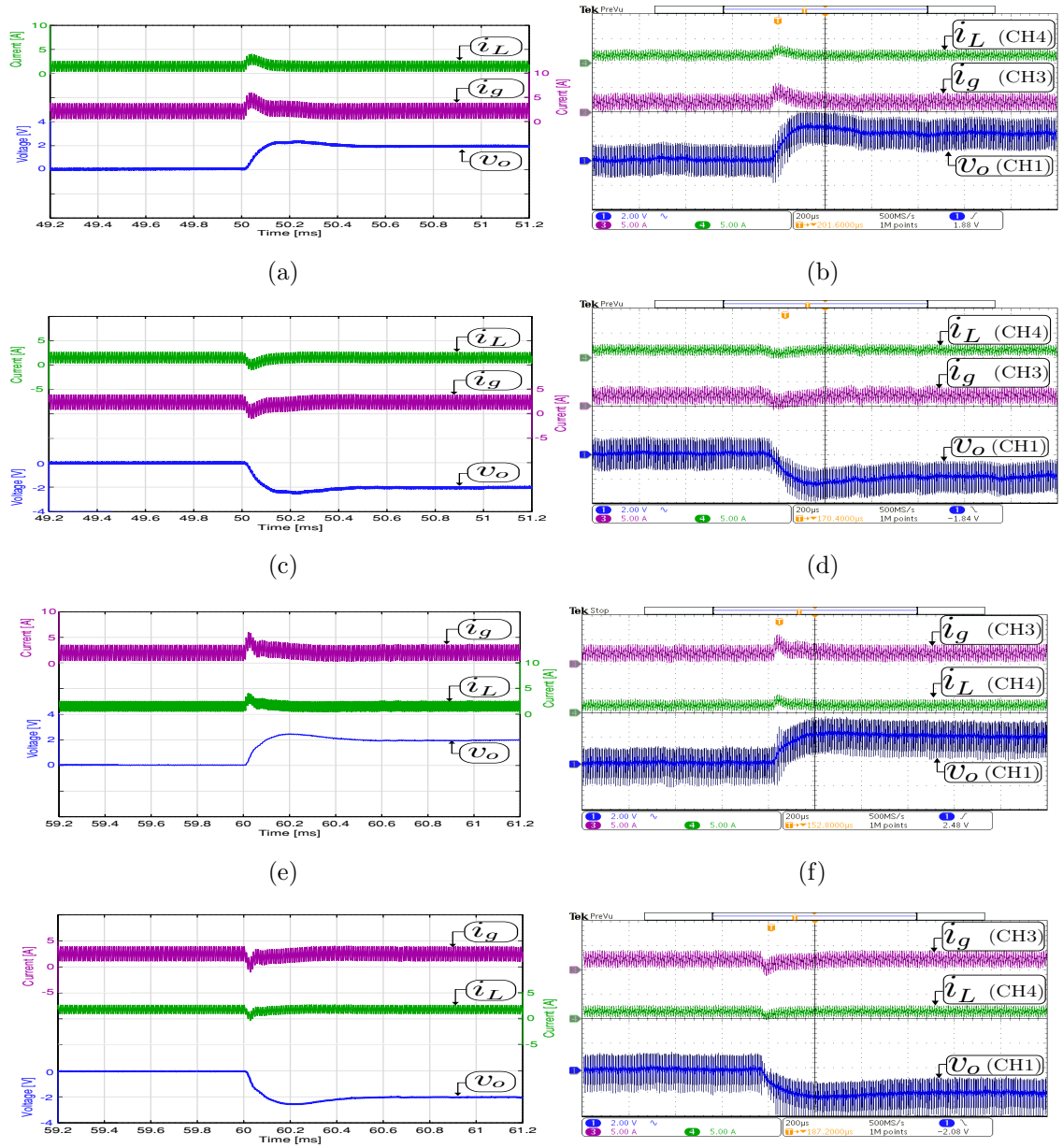

Figure **3-9**: Small signal transient response with a constant resistive load $R_o = 200\,\Omega$ in boost mode ($V_g = 200$ V). Multisample: Simulated (a), (c) and experimental (b), (d). Sliding: Simulated (e), (g) and experimental (f), (h). Transient response when the output voltage reference changes from 294 to 296 V (a), (b), (e), (f), and from 296 V to 294 V (c), (d), (g), (h). CH1: v_o (2 Vac/div), CH3: i_g (5 A/div), CH4: i_L (5 A/div), and time base of 200 μs.

EV, a real-time control and data acquisition, and a computer with software that executes some system or subsystem models to control the inverter. The components of an EV can

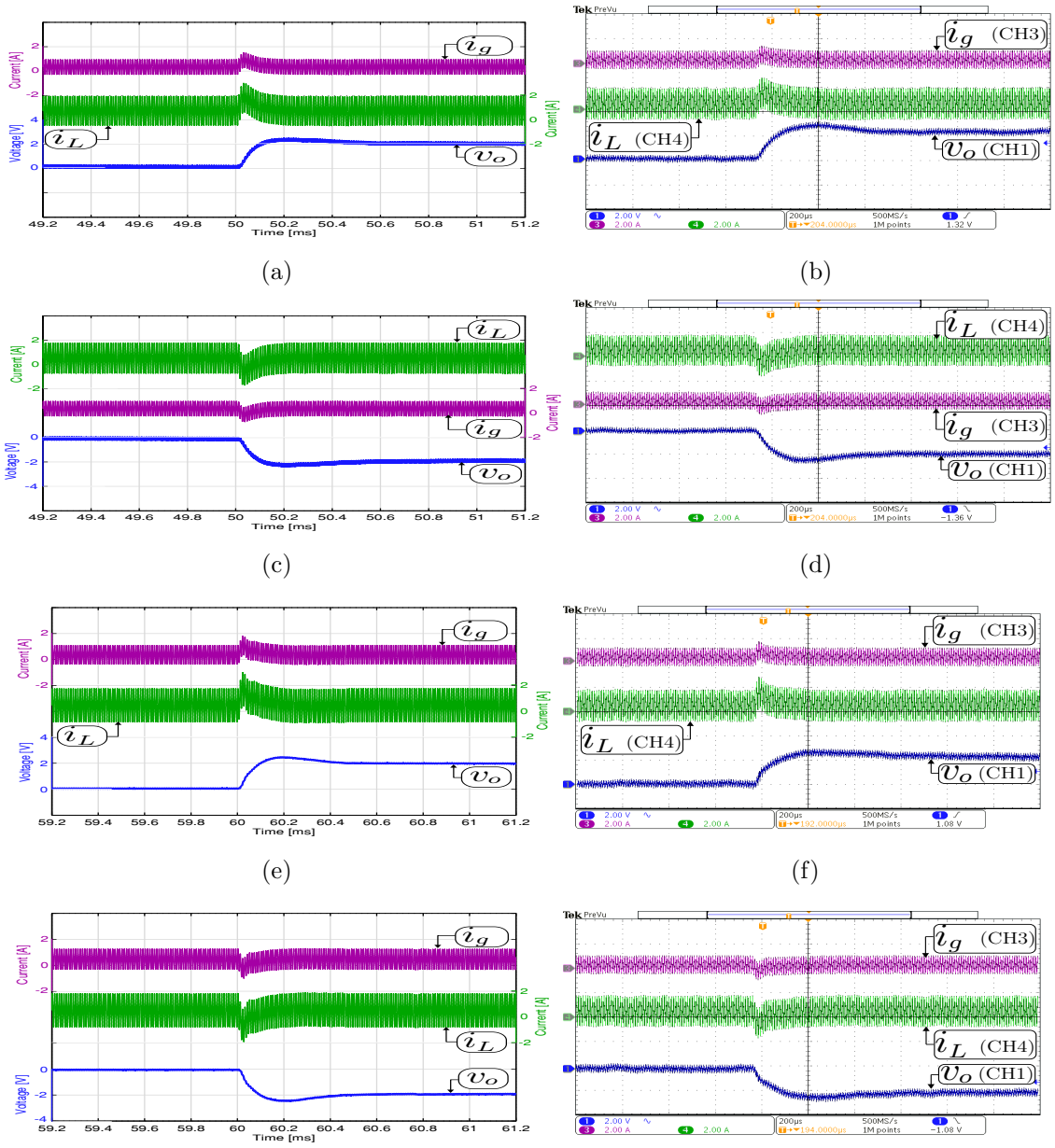

Figure **3-10**: Small signal transient response with a constant resistive load $R_o = 200\ \Omega$ in buck mode ($V_g = 200$ V). Multisample: Simulated (a), (c) and experimental (b), (d). Sliding: Simulated (e), (g) and experimental (f), (h). Transient response when the output voltage reference changes from 98 to 100 V (a), (b), (e), (f), and from 100 V to 98 V (c), (d), (g), (h). CH1: v_o (2 Vac/div), CH3: i_g (2 A/div), CH4: i_L (2 A/div), and time base of 200 μs.

be battery supplies, AC electric machine, and voltage source inverter. Different types of HIL simulation in research of EV are showed in [61], and it presents some advantages of

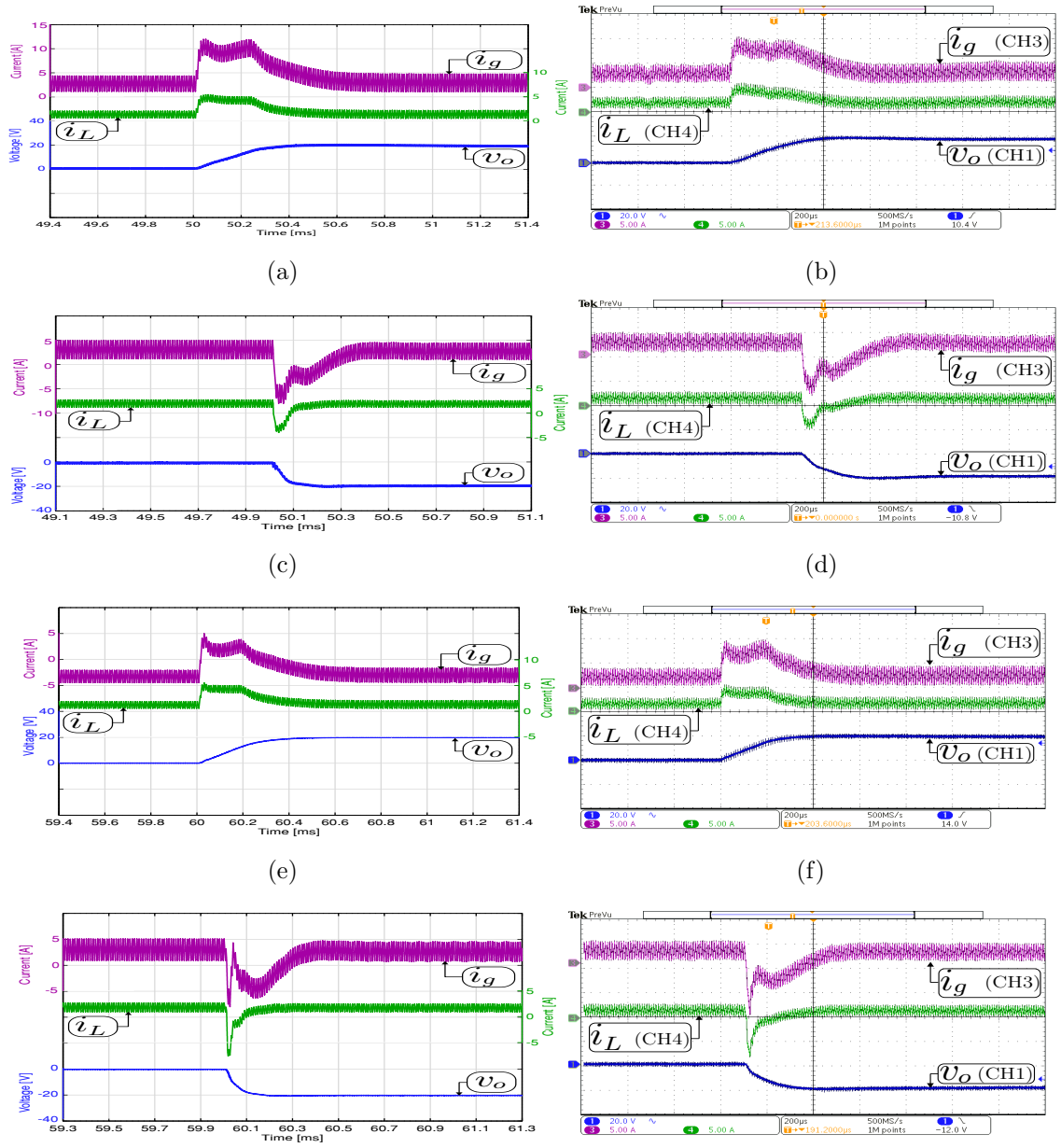

Figure **3-11**: Large signal transient response with a constant resistive load $R_o = 200\ \Omega$ in boost mode ($V_g = 200$ V). Multisample: Simulated (a), (c) and experimental (b), (d). Sliding: Simulated (e), (g) and experimental (f), (h). Transient response when the output voltage reference changes from 294 to 314 V (a), (b), (e), (f), and from 314 to 294 V (c), (d), (g), (h). CH1: v_o (20 Vac/div), CH3: i_g (5 A/div), CH4: i_L (5 A/div), and time base of 200 μs.

work with this type of platform, as studies on powertrain controller and control strategy, on battery and energy management, on regenerative braking, and on drive system.

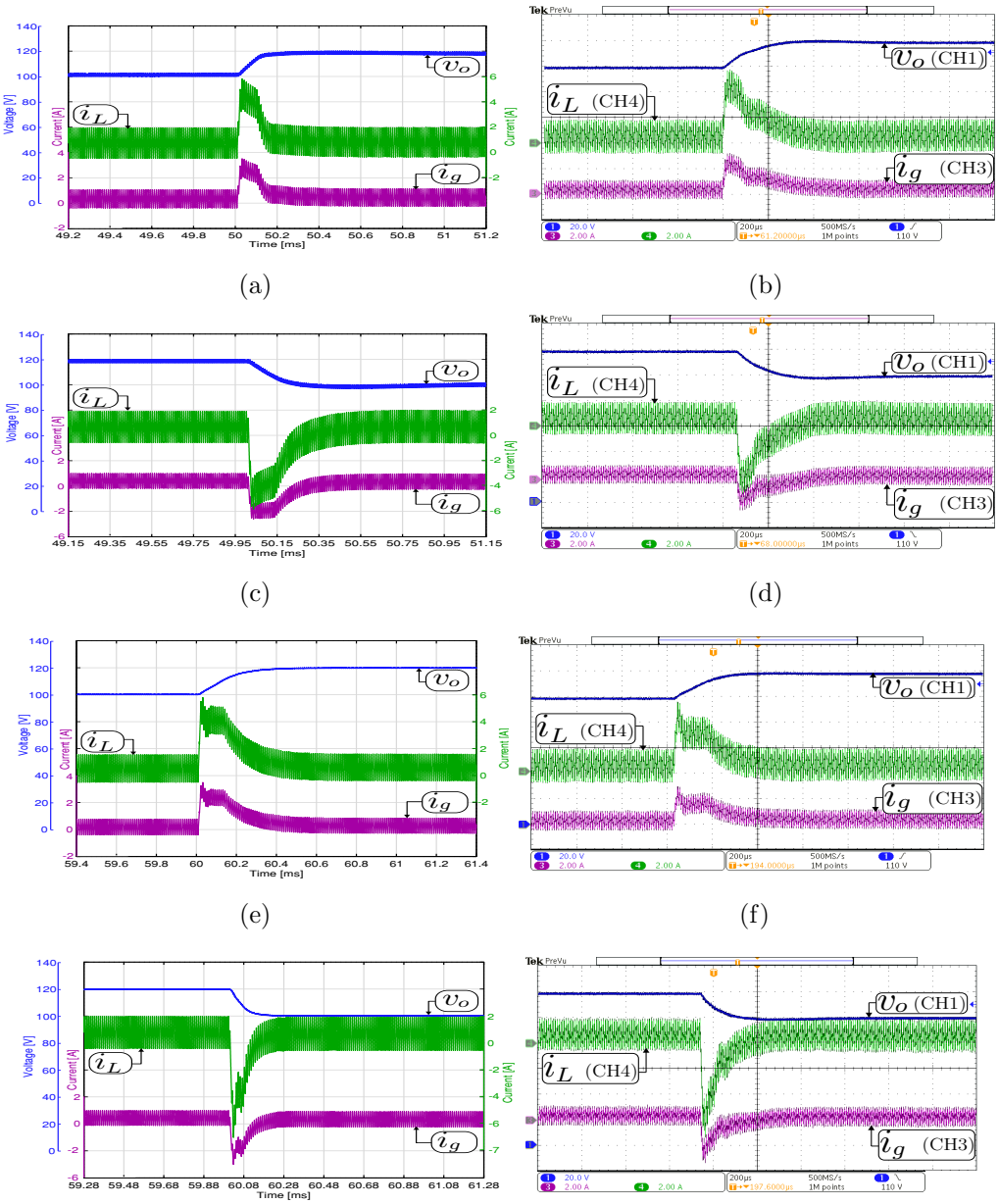

Figure **3-12**: Large signal transient response with a constant resistive load $R_o = 200\ \Omega$ in buck mode ($V_g = 200$ V). Multisample: Simulated (a), (c) and experimental (b), (d) Sliding: Simulated (e), (g) and experimental (f), (h). Transient response when the output voltage reference changes from 100 to 120 V (a), (b), (e), (f), and from 120 to 100 V (c), (d), (g), (h). CH1: v_o (20 V/div), CH3: i_g (2 A/div), CH4: i_L (2 A/div), and time base of 200 μs.

Some experiments are carried out considering a platform that emulates an EV powertrain described in Figure **3-13**. This system is composed of permanent-magnet synchronous mo-

tors (PMSMs). One of them (LSRPM 100 L) is working as a traction motor ($P_m = 4.5$ kW) and the other one (LSRPM 90 SL) is working as a controlled torque load ($P_m = 3$ kW). The traction part is controlled by an universal variable speed ac drive (SP2202) and it is fed by means of the buck-boost converter described in this work. This converter is connected between the dc power supply (AMREL SPS800X13-K02D) and the output filter capacitor C_o (R75PW44704030J). Subsequently, the traction motor is mechanically coupled to the motor that emulates the load (EV behaviour). This traction motor is controlled according to a speed profile provided by a specific driving cycle. On the other hand, the load motor is controlled by an universal variable speed ac drive (SP1405) to follow a torque reference based on the vehicle dynamic. Finally, a third variable speed ac drive (SP1405) allows the injection of power into the grid. An EV powertrain system model has been implemented in PSIM software with the parameters of the PMSMs listed in Table **3-4**. In order to startup the system with an initial voltage to fed the unidrive SP2202, a soft-starting of the dc-dc converter is implemented by algorithm as was previously described in section 3.6.1, and the simulated and experimental results are shown in Figure **3-14**. During the startup, the reference voltage v_{oref} changed from 0 V to the final desired output voltage value with short transient response around 0.9 s. The switching frequency for the inverter (SP2202) is 16 kHz. Figures **3-14** (a) and (b) show the startup response in boost mode with $V_g = 200$ V and steady-state output voltage value of 350 V. In this experiment the currents have an average value of 0 A in steady-state because the motors are not operating during the startup; however, the inverter remains switched because it has a 200 V power supply in terminals. Figures **3-14** (c) and (d) shows the converter steady-state response in buck mode with an input voltage (V_g) of 400 V, and output voltage (v_o) of 300 V. The figures also show good agreement between the experimental data and the simulation results.

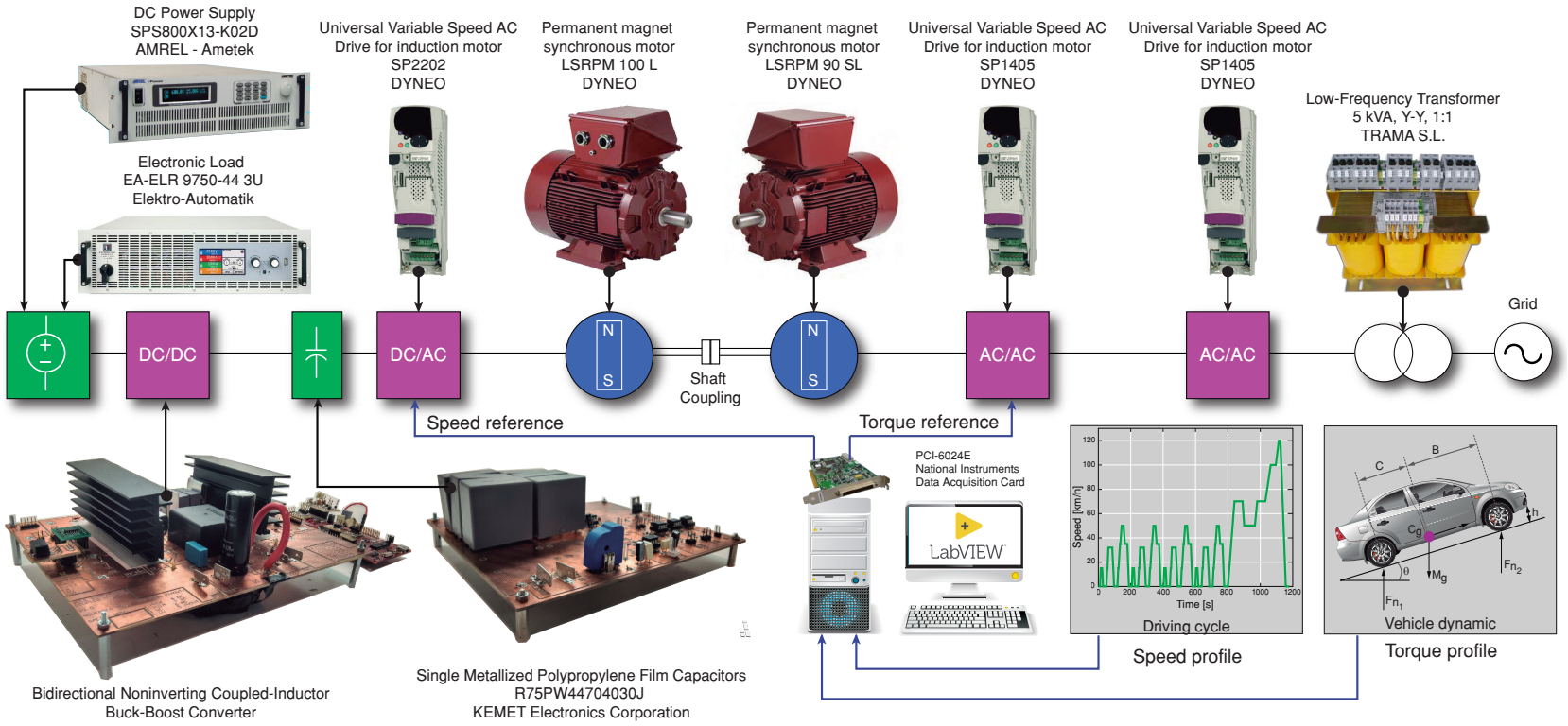

Figure **3-13**: Diagram of the experimental setup: Converter dc-dc and EV powertrain.

Parameter	90SL	100L
Motor rated speed	1500 [rpm]	1500 [rpm]
Number of pole pairs	8	8
d-axis inductance L_d	50.124 mH	29.128 mH
q-axis inductance L_d	29.128 mH	19.295 mH
Moment of inertia J	0.0032 $kg.m^2$	0.0066 $kg.m^2$
Electrical constant k_e	212 V_{kp}/k_{rpm}	223 V_{kp}/k_{rpm}

Table **3-4**: Parameters of the PMSMs.

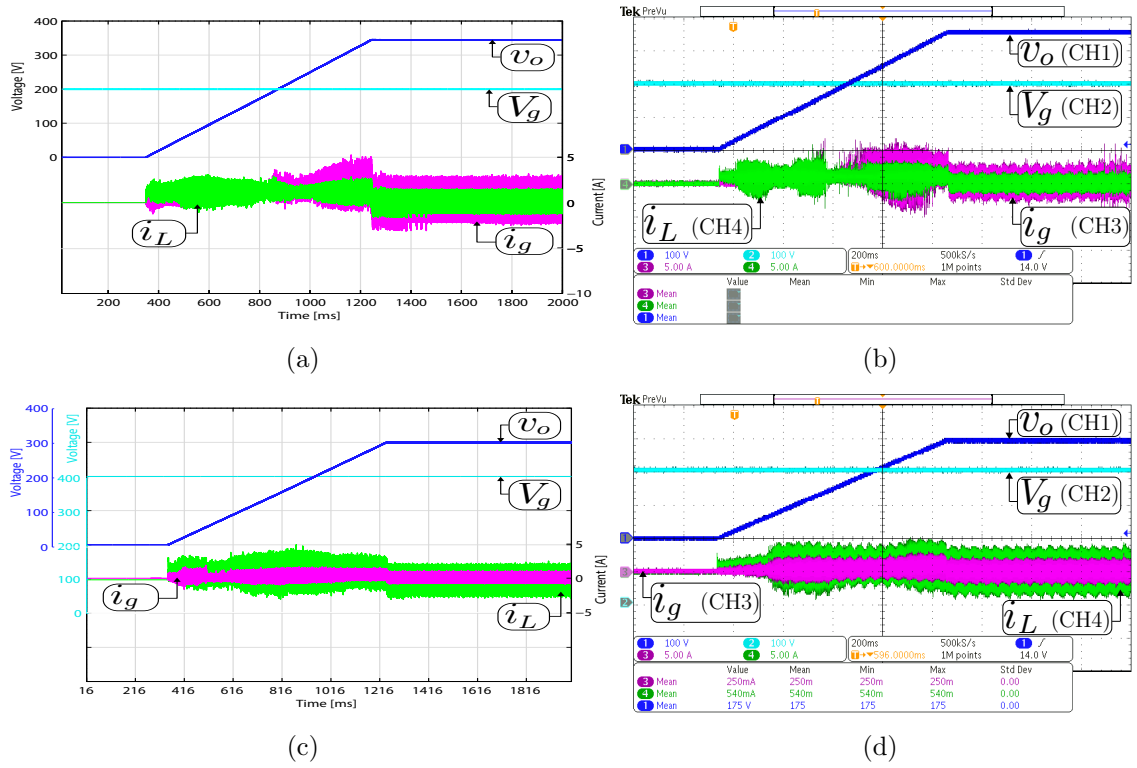

Figure **3-14**: Converter startup with an EV powertrain system emulation. Simulated (a), (c) and experimental (b), (d). Two operation modes in steady-state are shown: (a), (b) boost mode (V_g = 200 V, v_o = 350 V) and (c), (d) buck mode (V_g = 400 V, v_o = 300 V). CH1: v_o (100 V/div), CH2: V_g (100 V/div), CH3: i_g (5 A/div), CH4: i_L (5 A/div), and time base of 200 ms.

Figure **3-15** shows the transient response with a 450 W step change in the load power, setting the speed reference in 500 rpm and the torque value in 3.77 Nm to obtain a dc bus power demand of 300 W, and then change the speed reference to 1250 rpm to obtain a dc

bus power demand of 750 W. As a result, the output current changes from 1 A to 2.5 A gradually while the output voltage is regulated at 300 V. In the experimental and simulated results of Figure **3-16** the converter can be seen working in boost mode with $V_g = 200$ V for bidirectional power flow, the speed of the traction motor is set to 500 rpm, and the torque of the load motor to 7.53 Nm to get a dc bus demand of 600 W. The dc component (300 V) was removed to appreciate the ± 20 V step change in the output voltage reference. Figure **3-16** (a) and (b) show the results when the output voltage is changed from 300 V to 320 V with a step change, the current output i_L quicky goes to 4 A. Figures **3-16** (c) and (d) show the results when the output voltage is changed from 320 V to 300 V with a step change, the current output i_L decreases to -3 A. This current was limited above the rated current (-4 A) due to the limitation of the source is 13 A, and the battery was simulated with a dc source (AMREL SPS800X13-K02D) in parallel with an electronic load (EA-ELR 9750-44 3U) (see Figure **3-13**) in resistance mode to absorb 6 A, and it can absorb the current when the output voltage is decreased. The output voltage has a 20 V step change over 28 ms, and has a -20 V step change at the output voltage over 12 ms. This time is different for each case due to the unidrive SP2202 has an input filter capacitor of 2870 μF. Accordingly, this time depends of the filter capacitor value and the instantaneous current through the capacitor during the charging or discharging due to the output voltage step changes. Finally, there is a qualitative good agreement between the simulated and the experimental results in the case of the EV powertrain system emulation for the proposed control and in all the converter operation modes.

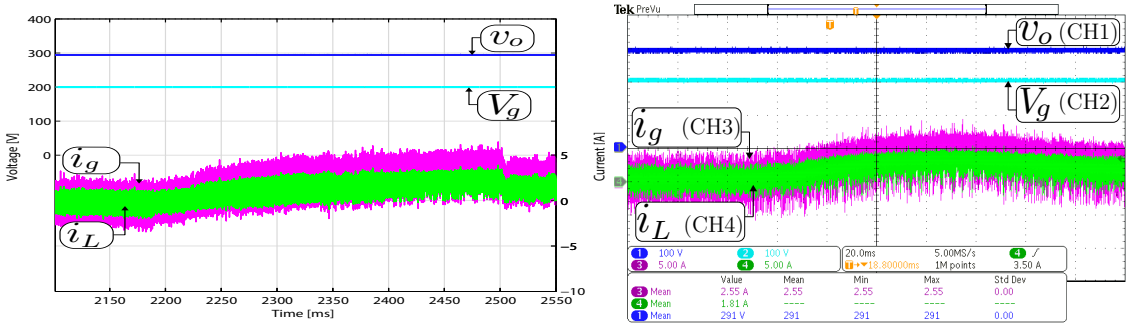

(a) (b)

Figure **3-15**: Boost operation mode in steady-state for a step power transition ($P_o = 300$ to 750 W, $V_g = 200$ V, $V_o = 300$ V) with an EV powertrain system emulation. Simulated (a), and experimental (b). CH1: V_o (100 V/div), CH2: V_g (100 V/div), CH3: i_g (5 A/div), CH4: i_L (5 A/div), and time base of 20 ms.

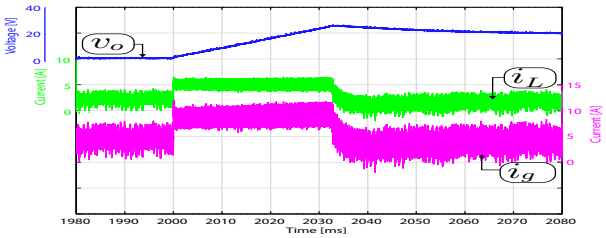

(a)

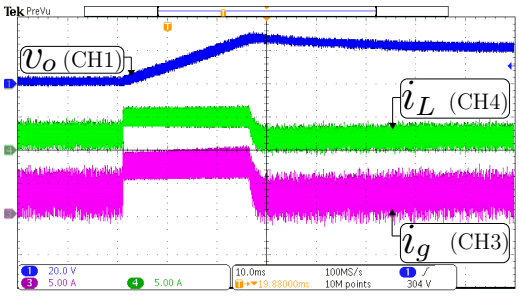

(b)

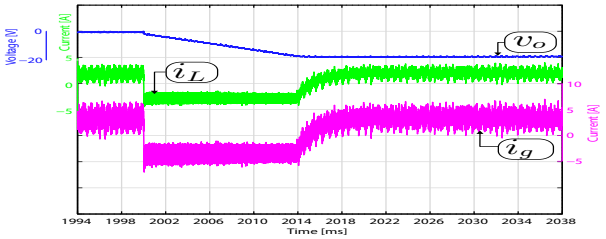

(c)

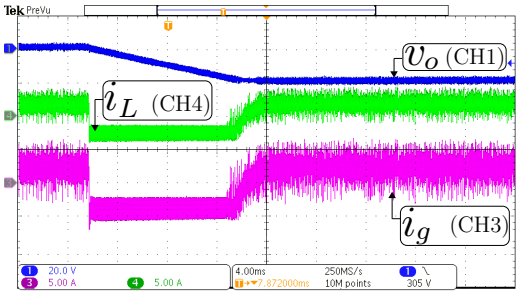

(d)

Figure **3-16**: Boost operation mode in steady-state with an EV powertrain system emulation $V_g = 200$ V. Transient response when the output voltage reference changes from 300 to 320 V. Simulated (a), (c) and experimental (b), (d), time base of 10 ms. (a), (b), and from 320 to 300 V time base of 4 ms. (c), (d). CH1: V_o (20 V/div), CH3: i_g (5 A/div), CH4: i_L (5 A/div).

3.7 Conclusion

In order to have a variable dc bus voltage related to the speed drive profile, the design, simulation and implemented of a dc-dc coupled inductor buck-boost converter between the vehicle battery and the motor traction inverter has been analyzed in the previous chapter. To achieve variable bus voltage regulation, a two-loop digital control strategy composed by an outer voltage control loop and a fast inner programmed controller is proposed. Two different inner current programmed controllers were proposed, which correspond to a sliding-mode current control and a multisampled average current control. The first one works at a sampling frequency of 100 kHz meanwhile the multisampled one is operating at sampling frequency of 200 kHz. A Texas Instruments TMS320F28377S DSC is used to implement the digital control loops. The digital implementation of this current controllers have allowed to include a dead-zone avoidance technique that effectively has suppressed very effectively undesirable non-linear phenomena in the buck-boost mode transitions such as subharmonics or other undesirable nonlinear phenomena. Both implemented digital current control strategies presented similar dynamic behavior.

The theoretical analysis have been validated by means of simulations and experimental tests performed on a 400 V 1.6 kW purpose built-prototype with high efficiency due to the use of SiC devices and the design with a low winding-to-winding parasitic capacitance of the coupled inductor. Both current controllers allow to regulate the traction dc bus during motoring and regeneration (regenerative brake) conditions while ensure fast tracking of the control set-point and low steady state error under demanding tests that include system start-up, dc bus voltage reference with small and large variations and under realistic conditions by means of an EV powertrain system emulation. As well, the prototype has has been tested in wide voltage conversion range. The experimental results are in good agreement with the simulation and the theoretical predictions.

4 ADC quantization effects for a two-loop control in a dc-dc converter

4.1 Abstract

This chapter presents a simple method to reduce undesired quantization-induced perturbations (QIP) in a voltage regulated dc-dc buck-boost converter using a two-loop digital control. The proposed method does not follow the usual approach to avoid limit-cycle oscillations (LCO) by implementing a digitally controlled pulse width modulation (DPWM) with higher resolution than the analog-to-digital converter (ADC) in the voltage-loop. Instead, even when a low resolution DPWM is used, QIP are eliminated by discretizing the voltage error in differential mode and selecting a multisampled average current control (MACC) for the inner current-programmed loop. In addition, the use of MACC allows designing a stable wide-bandwidth voltage loop. A 400 V 1.6 kW proof-of-concept converter has been used to illustrate the presence of QIP and to verify the effectiveness of the proposed scheme to suppress them. The controller is programmed in a digital signal controller (DSC) TMS320F28377S with features as a DPWM with 8.96-bit equivalent resolution, a 12-bit ADC for the current sampling, and a 16-bit ADC for the error sampling.

4.2 Introduction

Digital control in dc-dc converters is of interest since it shows many potential advantages such as low power consumption, and flexibility to program and design different advanced control strategies to improve the system performance [62]. Therefore, digital closed-loops are increasingly being used in dc-dc converters [63]. However, many works report disadvantageous quantization effects related to the existence of limit cycles in digitally controlled pulse width modulation converters. Static and dynamic models taking into account the quantization effects are derived and used to explain the origins of limit-cycle oscillations for voltage single-loop digital control in [64, 65]. A lower resolution of the DPWM than of the ADC usually causes LCO that affect the regulation of the controlled variable [66]. Therefore, DPWM with resolution higher than the ADC is usually implemented in order to reduce the effect of limit-cycle oscillations in voltage single-loop digital control, where the the difference between the voltage reference and the output voltage is quantized to a digital number to

represent the error signal [67, 68].
It is well known that cascade control of dc-dc converters offers generally better performance than single-loop control. Analysis of LCO are given in [69–71] for two-loop digital controls with inner current loop. In these works the resolution of the DPWM is also greater than the ADC resolution in the outer voltage loop. In [69] an estimation algorithm has been applied to the average current control of a buck converter in order to reduce quantization effects in the inductor current loop and, thus, the presence of limit cycle oscillations. A method to design a two-loop digital control is developed in [70], where the current reference is dynamically adjusted to give a solution to the LCO problem. A technique to compute the steady-state duty cycle in real-time when the feedback-loop digital control is working, was considered in [71], where a time-to-digital converter translates the duty ratio information into digital code using a moving average filter and an adjustable current loop sampling frequency. At steady-state, this strategy disables current-loop sampling and the control compute, using a virtual open loop configuration, this technique reduces oscillations of the inductor current in a buck converter.
In order to improve the resolution of the DPWM in voltage single-loop digital controllers some authors use sigma-delta modulation to eliminate the quantization noise and the LCO. In [66] a non-zero error method is used to encode the output voltage error and to improve the low resolution of the DPWM. A sigma delta modulation scheme and the frequency modulation of the switching frequency are combined in [72] to increase the effective resolution of the DPWM.
The sometimes dangerous QIP can be reduced in a coupled-inductor dc-dc buck-boost converter with a MACC inner loop at the expense of limiting the bandwidth of the outer voltage loop, if a conventional approach to obtain the voltage error is implemented and a low-resolution DPWM is used. This chapter proposes the implementation of an improved voltage error block combined with a MACC inner loop to regulate the output voltage with reduced undesired quantization effects even using a low-resolution DPWM. Simulation and experimental results of the conventional design are compared with results obtained using the proposed scheme to verify that the perturbations are suppressed from the current signals while widening the voltage loop bandwidth.

4.3 Digitally controlled buck-boost converter

Considering the dc-dc buck-boost bidirectional converter for voltage regulation application shown in Fig. **4-1**, this topology is introduced as an unidirectional buck-boost converter in [1], the design was described in chapter 2 and the voltage regulation application was detailed in chapter 3. The bidirectional power stage shown in Fig. **4-1** is composed by a coupled inductors with unitary turns ratio and magnetic coupling coefficient $k = 0.5$. Therefore, primary self-inductance L_1 is equal to secondary self-inductance L_2 ($L_1 = L_2 = L$), and their mutual inductance is $M = L/2$. The two-loop digital voltage controller proposed in

Fig. **4-2** consists of a MACC inner current programmed controller and a PI compensator at the outer voltage feedback loop.

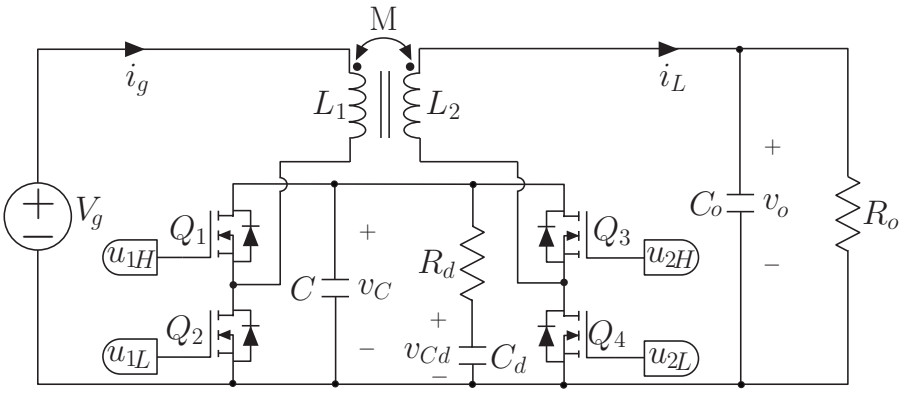

Figure **4-1**: Power stage of a coupled-inductor buck-boost converter.

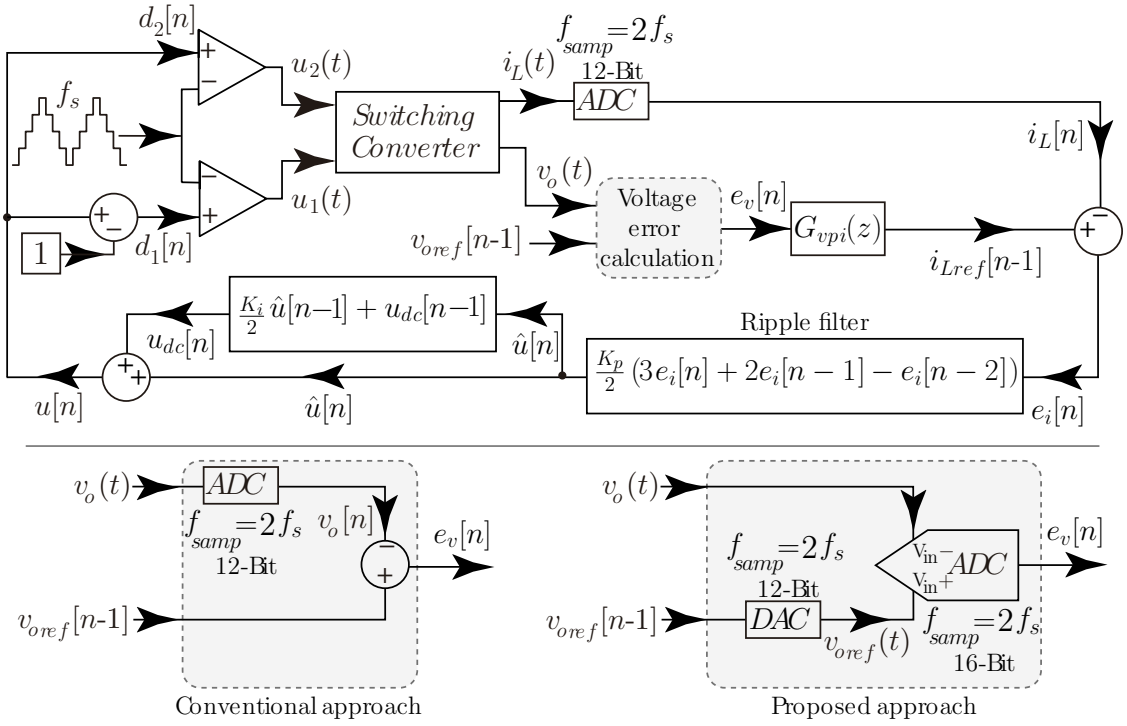

Figure **4-2**: Block diagram of the digital controller for the voltage regulation of the buck-boost converter. Bottom Left: Conventional voltage error subcircuit. Bottom Right: Proposed improved approach subcircuit.

4.3.1 Multisampled average current control

The multisampled average current control for the bidirectional buck-boost converter was presented in [43] and implemented for the proposed converter in chapter 3. The MACC stage generates the control variable (u) that is processed by a dual digital PWM to obtain the discrete control signals (u_1 and u_2) that activate the converter half-bridges. The external loop regulates the output voltage by providing the MACC with the output current reference through a discrete proportional-integral control transfer function $G_{vpi}(z)$ as is seen in Fig. **4-2**. An important element of the MACC loop is the ripple filter processing the error between output current $i_L[n]$ and its desired reference $i_{Lref}[n-1]$. The ripple filter averages two consecutive samples per switching period ($f_{samp} = 2f_s$) of the output current error. This strategy eliminates the switching ripple in the current loop without significant phase loss [73, 74].

4.3.2 Digital Proportional-Integral voltage control

A slower outer voltage loop is added to the inner current loop to feed it with the reference variable i_{Lref}. Its PI control is designed taken into account the value of the output filter capacitor, C_o, and the desired loop-gain crossover frequency f_c. The transfer function of the PI voltage controller can be expressed in the z domain using the forward Euler method as

$$G_{vpi}(z) = K_{pv} + \frac{K_{iv}T_{samp}}{z-1}z^{-1} \tag{4-1}$$

where $K_{pv} = C_o 2\pi f_c$, $K_{iv} = K_{pv}/T_i$, and T_{samp} is the sample period ($1/f_{samp}$). Hence, the bandwidth of the voltage loop depends on the proportional coefficient (K_{pv}), while the phase margin (PM) is adjusted to be greater than 50° by selecting ($T_i = 150\ \mu\text{s} > 1/(2\pi f_c)$) for the integral coefficient (K_{iv}). The forward-Euler method is used to find the recurrence equations for the discrete-time PI controller:

$$\begin{aligned} i_{Lp}[n] &= K_{pv}e_v[n] \\ i_{Li}[n] &= K_{iv}T_{samp}e_v[n] + i_{Li}[n-1] \\ i_{Lref}[n] &= i_{Lp}[n] + i_{Li}[n]. \end{aligned} \tag{4-2}$$

4.4 Two-loop quantization effects

Fig. **4-2** shows two methods to get the voltage error. The conventional approach on the left side uses an ADC for sampling the voltage and then computes the voltage error. On the right side, the proposed method quantizes the voltage error by using an ADC on differential mode. Previously it produces an analog voltage reference form the digital one. Fig. **4-3** shows simulated waveforms of output current i_L and its reference i_{Lref} when the converter operates in steady-state. The converter parameters used in the simulations are: $V_g = 200$ V,

$L_1 = L_2 = 270$ μH, $M = 135$ μH, $C = 1.32$ μF, $C_d = 20$ μF, $R_d = 5$ Ω, $C_o = 28$ μF, $R_o = 200$ Ω, $f_s = 100$ kHz, and the output voltage is regulated to $v_o = 300$ V.

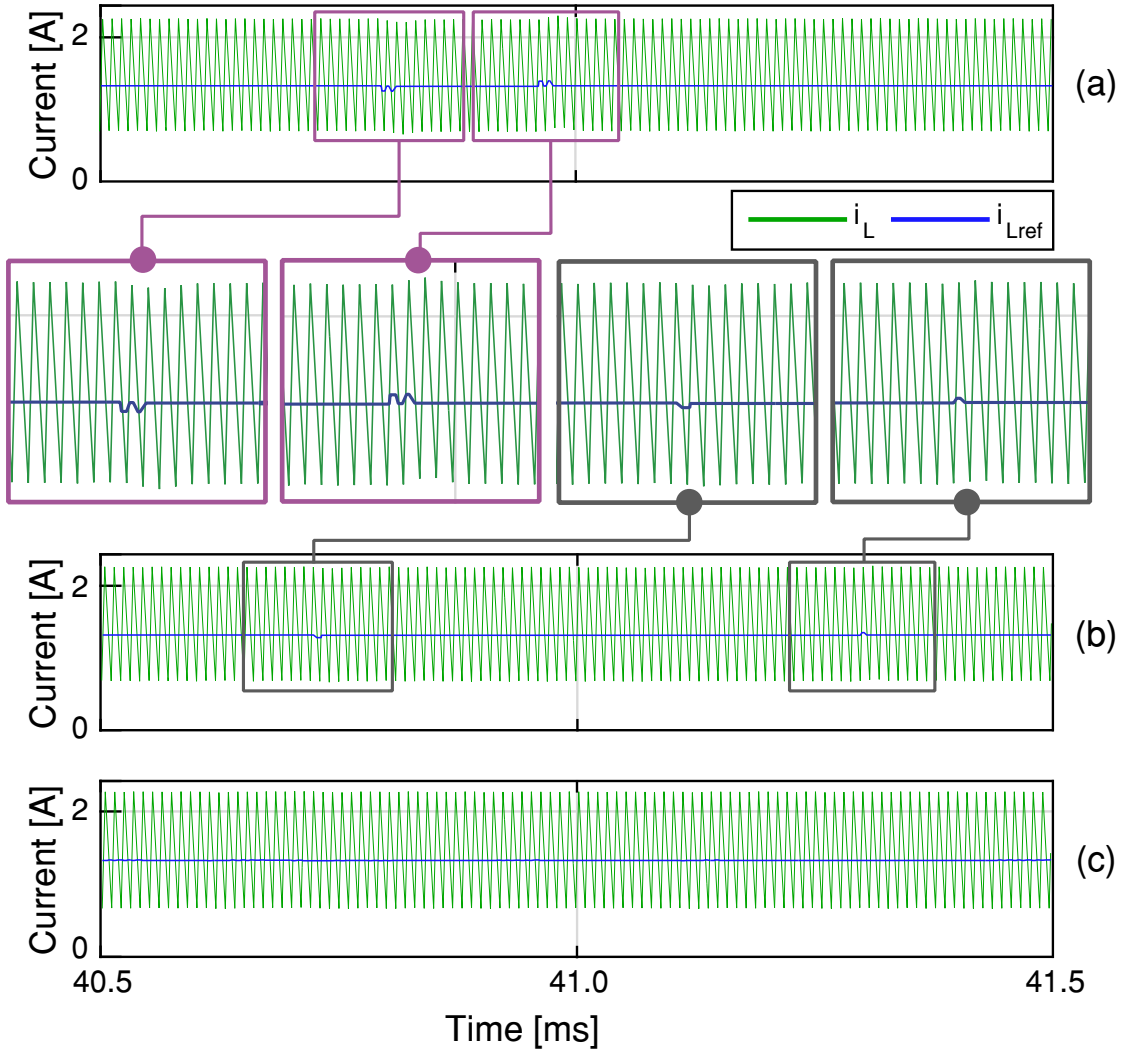

Figure **4-3**: Simulation of output current i_L and its reference i_{Lref} with the converter operating in steady-state: (a) Conventional approach with $K_{pv} = 0.7$. (b) Conventional approach with $K_{pv} = 0.44$. (c) Proposed improved approach with $K_{pv} = 0.7$. Sections depicting quantization-induced perturbations, not present in (c), are enlarged between (a) and (b) simulations.

Figs. **4-3**(a) and **4-3**(b) (see also the magnified sections) show some undesired QIP in both currents, i_L and its reference i_{Lref}, when using the conventional method to compute the voltage error. Since the control bandwidth (crossover frequency) depends on the proportional gain K_{pv} to widen the bandwidth the proportional gain has to be increased. For the case of Fig. **4-3**(a), when $K_{pv} = 0.7$ to obtain a crossover frequency (CF) of 4 kHz, the perturbation

peaks in the current reference are higher that the quantization level of the ADC sampling the output voltage. Using the proposed approach improves the error resolution and avoids the undesired perturbations in i_L, as show the corresponding simulation results shown in Fig. **4-3**(c), where clearly the perturbations have disappeared from both currents. To compare bandwidths and stability margins provided by each of the schemes of computing the voltage error, the corresponding Bode plots of the voltage loop-gains for the converter operating in boost mode (see parameters in next Section) are provided in Fig. **4-4**. Experimental plots in Fig. **4-4**(b) show that the proposed method with $K_{pv} = 0.7$ provides a CF of 4 kHz with a PM of 52° while the conventional method with $K_{pv} = 0.44$, with smaller quantization perturbations (see Fig. **4-3**(b)), yields a CF= 2.16 kHz with PM= 59.58°. These values are in good agreement with the simulated results in Fig. **4-4**(a).

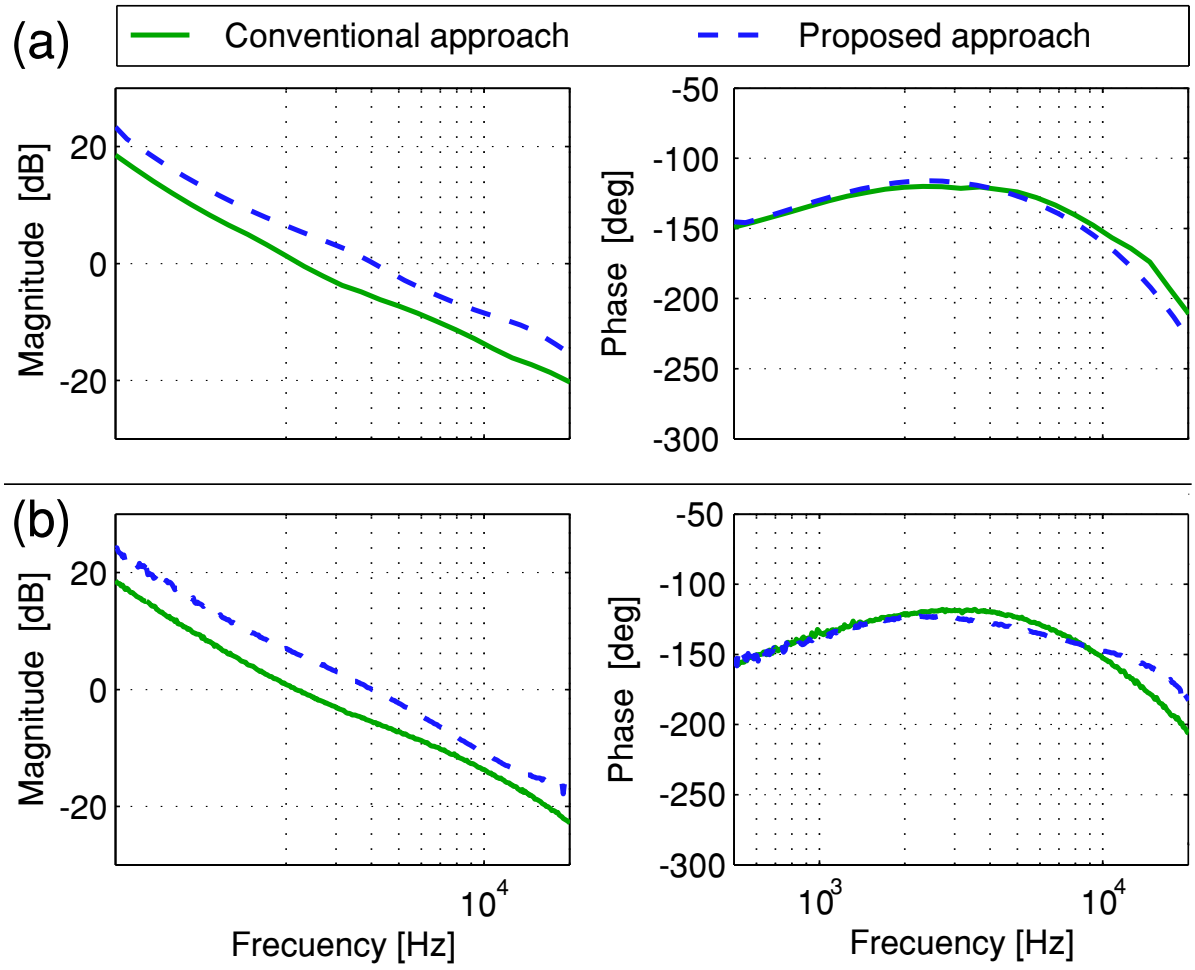

Figure **4-4**: Voltage loop-gain Bode plots: (a) simulated, (b) experimental.

4.5 Simulation and experimental results

The experimental setup used to test the different schemes to compute the voltage error with the MACC-based two-loop digital control is shown in Fig. **4-5**. It is composed of a 400-V 1.6-kW buck-boost test-of-concept converter with the parameters described in the previous Section, and the TMS320F28377S DSC. In addition to the loop-gain measurements in the frequency domain of previous Section, additional experiments and simulations have been performed to observe the current waveforms at start-up together with about 12 ms of steady-state regime.

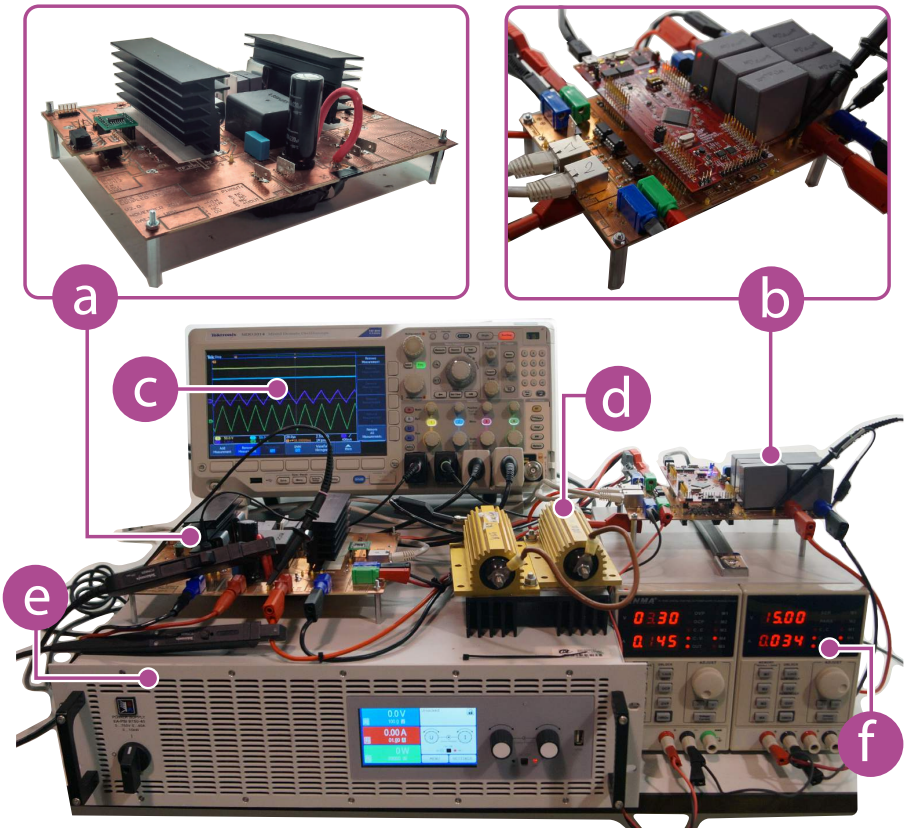

Figure **4-5**: Experimental setup of the buck-boost voltage regulator: (a) coupled-inductor buck-boost power stage, (b) digital signal controller with output capacitor $C_o = 28\ \mu$F, (c) oscilloscope, (d) constant resistive load $R_o = 200\ \Omega$ (e) input dc power supply, (f) auxiliary power supply for DSC and MOSFET drivers.

Fig. **4-6** depicts input (i_g) and output (i_L) current waveforms in the same three cases already simulated in Figs. **4-3**. In this way, Figs. 4.6(a), 4.6(b), 4.6(c), 4.6(d) correspond to the conventional approach, the DPWM was configured for 8.96-bit and the ADCs for sampling the output current and voltage were configured with a 12-bit resolution with an analog

input ranging from 0 V to 3 V. Figs. 4.6(a), 4.6(b) show the simulated and experimental results when the proportional gain of the voltage loop is selected as $K_{pv} = 0.7$ to obtain a large bandwidth. In this case, the current waveforms have perturbations with high current overshoot and undershoot values. Results when the gain K_{pv} is reduced to the more conservative value of 0.44 are plotted in Figs. 4.6(c), 4.6(d) showing that limiting the voltage loop bandwidth using the conventional error-calculation method reduces QIP in both currents and improves the closed-loop stability. The current waveforms with the proposed improved approach in Figs. 4.6(e), 4.6(f) show that there are no significant current perturbations when the proportional gain is again selected to $K_{pv} = 0.7$ to obtain a wide bandwidth voltage loop with a phase margin larger than 50°. For this case, the DPWM was configured with a 8.96-bit resolution, while the ADCs sampling the output current and the voltage error were configured with resolutions of 12-bit and 16-bit-differential-mode, respectively.

Fig. **4-7** compares the large-signal responses of the regulator when the output voltage has a 20 V step change both conventional and proposed methods. The results for the conventional method with $K_{pv} = 0.7$ have not been included because of high current perturbation that damaged the prototype in the experiment. In the experimental and simulation results, dc components have been removed to magnify the 20-V output voltage variation. The waveforms using the proposed method to compute the voltage error with $K_{pv} = 0.7$ of Figs. 4.7(c), 4.7(d) exhibit a significantly shorter transient duration (about 200 μs) than those in Figs. 4.7(a), 4.7(b) (approx. 400 μs) corresponding to the conventional approach with $K_{pv} = 0.44$.

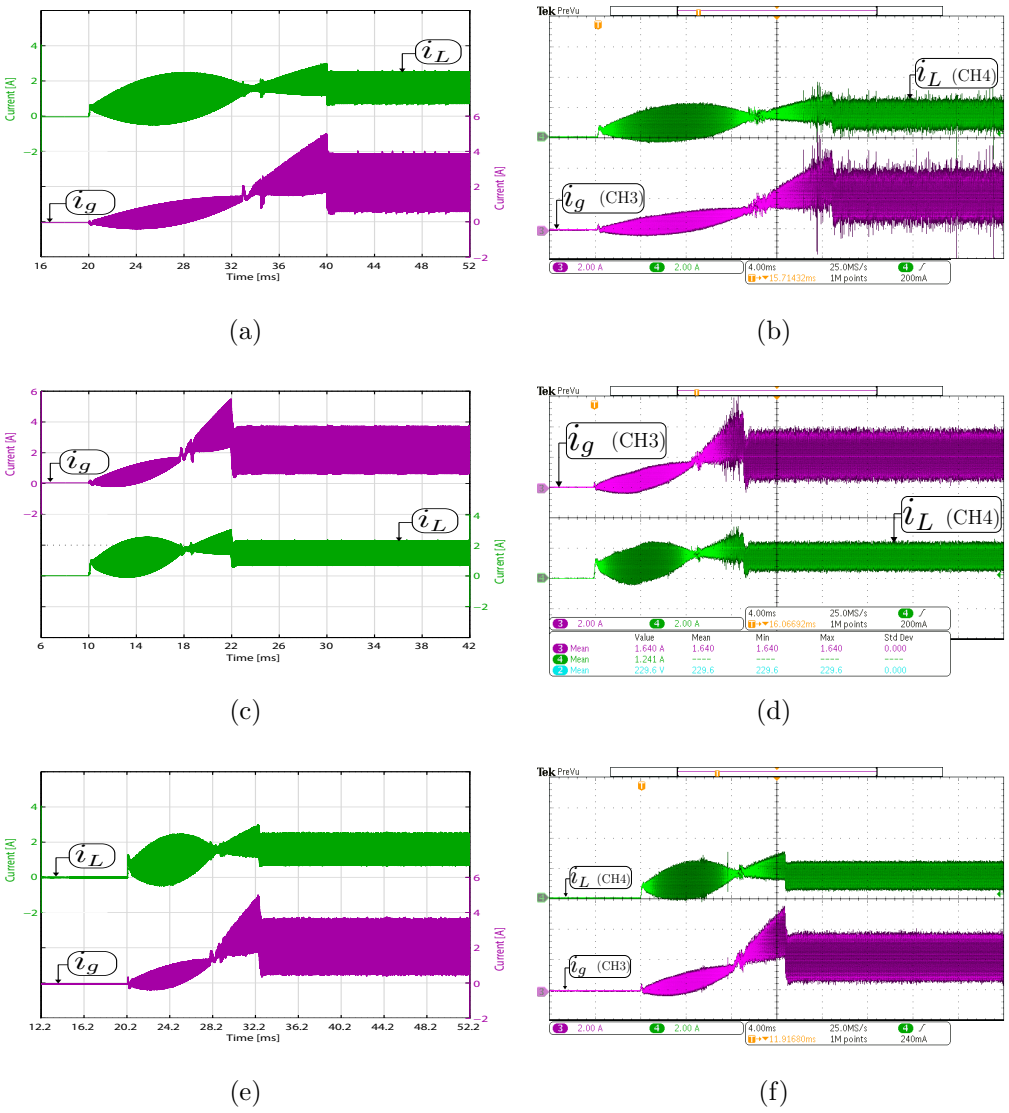

Figure **4-6**: Start-up waveforms of the input and output current: (a), (b), (c) simulated and (d), (e), (f) experimental. (a), (b) conventional approach with $K_{pv} = 0.7$; (c), (d) conventional approach with $K_{pv} = 0.44$; and (e), (f) proposed improved approach with $K_{pv} = 0.7$. ($V_g = 200$ V, $v_o = 293$ V and $R_o = 200\ \Omega$). CH3: i_g (2 A/div), CH4: i_L (2 A/div).

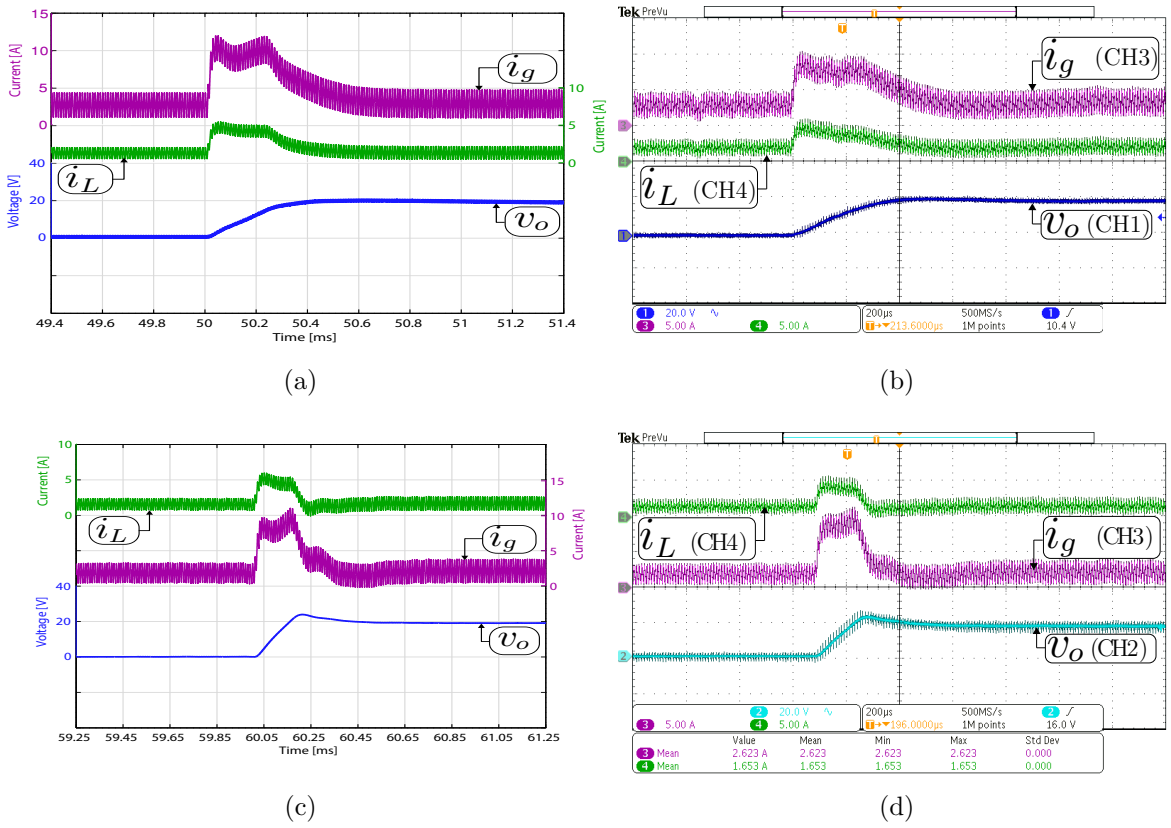

Figure **4-7**: Transient response when the output voltage reference changes from 294 to 314 V: (a), (b) simulated and, (b), (d) experimental with a constant resistive load $R_o = 200\ \Omega$ in boost mode ($V_g = 200$ V). (a), (b) Conventional approach with $K_{pv} = 0.44$, and (c), (d) Proposed approach with $K_{pv} = 0.7$. CH1: v_o (20 Vac/div), CH3: i_g (5 A/div), CH4: i_L (5 A/div), and time base of 200 μs.

4.6 Conclusion

In this chapter some undesired quantization effects in a two-loop digital regulator related to the resolution of the DPWM and ADCs, and the increase of the proportional gain of the voltage loop to have a wide bandwidth, are described. Simulation and experiments developed on a 400-V 1.6-kW coupled-inductor buck-boost purpose-built prototype validate that the current waveforms present perturbations when the bandwidth of voltage loop is increased, in spite of the inner loop being a digital control strategy. The digital control uses a conventional method to compute the voltage error method, which is programmed in a Texas Instruments TMS320F28377S DSC with two 12-bit A/D and a 8.96-bit DPWM. A simple scheme to compute the voltage error without any additional hardware is proposed to achieve significantly improved dynamic responses, reduce the quantization-induced perturbations,

and increase the voltage loop bandwidth with a similar phase margin. The improved method is implemented using a 16-bit ADC in differential-mode and the same low DPWM resolution (8.96-bit) of the DSC. Experimental and simulated results verify the effectiveness of the improved method.

5 Conclusions and future work

Nowadays power electronic converters for EV applications require efficiency optimization in a wide range of speeds instead of optimizing efficiency at the maximum power of the inverter traction. This is especially important for urban driving where the vehicle uses low speeds due to traffic congestion, traffic lights, pedestrian crossings, among other factors. The use of a high-efficiency step-up/step-down converter can improve the performance efficiency of the EV powertrain. This improvement includes an extent range of electric motor speeds which comprises urban and highway driving cycles.

The proposed bidirectional buck-boost converter with coupled inductor has been located between the battery system and the traction inverter to regulate the dc bus in electric vehicle powertrain configurations, as an alternative to conventional topologies based on the boost converter in EV applications. The converter is based on the versatile buck-boost converter which in low voltage and hard-switching applications has shown a great performance in different topologies of fuel cell hybrid systems. Therefore, extending the use of the converter to higher voltage applications such as the electric vehicle based on a battery system is a challenge that was addressed in this work.

Two 1.6 kW prototypes with an input voltage range of 200 V to 400 V, and output voltages between 100 V and 400 V have been built and validated. The first prototype is based on the conventional buck-boost converter proposed in [1] which presented a coupled coefficient $k = 1$ that was implemented with pair of tightly coupled inductors of turns ratio $N_1/N_2 = 1$ and an output inductor. A novel design of the coupled inductor was implemented for the second prototype, with a very low parasitic winding-to-winding capacitance and loose magnetic coupling ($k = 0.5$). Adapting the power stage damping network to the new parameters of the loosely coupled inductors is straightforward, the proposed buck-boost converter has fundamental efficiency improvements over wide ranges of high voltage, it results in a decrease in the total loss by a factor of two to three respect to the conventional buck-boost converter designed.

Two-loop digital control strategy composed by an outer voltage control loop and a fast inner programmed controller was proposed to achieve the dc bus voltage regulation. Two different inner current programmed controllers were proposed, which correspond to a sliding-mode current control and a multisampled average current control. A Texas Instruments TMS320F28377S DSC is used to implement the digital control loops. The digital implementation of this current controllers have allowed to include a dead-zone avoidance technique that effectively has suppressed very effectively undesirable nonlinear phenomena in the buck-

boost mode transitions such as subharmonics or other undesirable nonlinear phenomena. Both control strategies verify the controllability of the proposed bidirectional noninverting coupled-inductor buck-boost converter to regulate the traction dc bus during motoring and regeneration (regenerative brake) conditions while ensure fast tracking of the control set-point and low steady state error under demanding tests that include system start-up, dc bus voltage reference with small and large variations and under realistic conditions by means of an EV powertrain system emulation. As well, the prototype has has been tested in wide voltage conversion range. The experimental results are in good agreement with the simulation and the theoretical predictions.

Also, this work achieved other additional contributions on related topics, which are not among the main topics but still important in the field of digital control in dc-dc converters. The description of some undesired quantization effects in a two-loop digital regulator related to the resolution of the DPWM and ADCs, and the increase of the proportional gain of the voltage loop to have a wide bandwidth, were described. Simulation and experiments developed on a 400-V 1.6-kW coupled-inductor buck-boost purpose-built prototype validate that the current waveforms present perturbations when the bandwidth of voltage loop is increased, in spite of the inner loop being a MACC. The digital control was programmed in a Texas Instruments TMS320F28377S DSC. A simple scheme to compute the voltage error without any additional hardware is proposed to achieve significantly improved dynamic responses, reduce the quantization-induced perturbations, and increase the voltage loop bandwidth with a similar phase margin. The improved method is implemented using a 16-bit ADC in differential-mode of the DSC. Experimental and simulated results verify the effectiveness of the improved method.

The future work will deepen in the design of a powertrain, which include the design of traction inverter based on the versatile buck-boost converter, should be extended into the full powertrain system, and battery pack. It can empower the design of powertrain with better efficiency and power density.

Bibliography

[1] C. Restrepo, J. Calvente, A. Cid-Pastor, A. El Aroudi, and R. Giral, "A noninverting buck–boost dc–dc switching converter with high efficiency and wide bandwidth," *IEEE Transactions on Power Electronics*, vol. 26, no. 9, pp. 2490–2503, 2011.

[2] H. Qiao, Y. Zhang, Y. Yao, and L. Wei, "Analysis of buck-boost converters for fuel cell electric vehicles," in *Vehicular Electronics and Safety, 2006. ICVES 2006. IEEE International Conference on*. IEEE, 2006, pp. 109–113.

[3] E. Schaltz and P. O. Rasmussen, "Design and comparison of power systems for a fuel cell hybrid electric vehicle," in *Industry Applications Society Annual Meeting, 2008. IAS'08. IEEE*. IEEE, 2008, pp. 1–8.

[4] A. Lachichi and N. Schofield, "Comparison of dc-dc converter interfaces for fuel cells in electric vehicle applications," in *Vehicle Power and Propulsion Conference, 2006. VPPC'06. IEEE*. IEEE, 2006, pp. 1–6.

[5] M. Al Sakka, J. Van Mierlo, and H. Gualous, "Dc/dc converters for electric vehicles," in *Electric Vehicles-Modelling and Simulations*. InTech, 2011.

[6] T. Schoenen, M. S. Kunter, M. D. Hennen, and R. W. De Doncker, "Advantages of a variable dc-link voltage by using a dc-dc converter in hybrid-electric vehicles," in *Vehicle Power and Propulsion Conference (VPPC), 2010 IEEE*. IEEE, 2010, pp. 1–5.

[7] D. Han, J. Noppakunkajorn, and B. Sarlioglu, "Comprehensive efficiency, weight, and volume comparison of sic-and si-based bidirectional dc–dc converters for hybrid electric vehicles," *IEEE Transactions on vehicular technology*, vol. 63, no. 7, pp. 3001–3010, 2014.

[8] M. Olszewski *et al.*, "Evaluation of the 2010 toyota prius hybrid synergy drive system," *Oak Ridge Nat. Lab., US Dept. Energy*, 2011.

[9] J. O. Estima and A. J. M. Cardoso, "Efficiency analysis of drive train topologies applied to electric/hybrid vehicles," *IEEE Transactions on Vehicular Technology*, vol. 61, no. 3, pp. 1021–1031, 2012.

[10] H. Chen, K. Sabi, H. Kim, T. Harada, R. Erickson, and D. Maksimovic, "A 98.7% efficient composite converter architecture with application-tailored efficiency characteristic," *IEEE Transactions on Power Electronics*, vol. 31, no. 1, pp. 101–110, 2016.

[11] H. Chen, H. Kim, R. Erickson, and D. Maksimović, "Electrified automotive powertrain architecture using composite dc–dc converters," *IEEE Transactions on Power Electronics*, vol. 32, no. 1, pp. 98–116, 2017.

[12] L. Albiol-Tendillo, E. Vidal-Idiarte, J. Maixe-Altes, S. Mendez-Prince, and L. Martinez-Salamero, "Seamless sliding-mode control for bidirectional boost converter with output filter for electric vehicles applications," *IET Power Electronics*, vol. 8, no. 9, pp. 1808–1816, 2015.

[13] S. Dusmez, A. Hasanzadeh, and A. Khaligh, "Comparative analysis of bidirectional three-level dc–dc converter for automotive applications," *IEEE Transactions on Industrial Electronics*, vol. 62, no. 5, pp. 3305–3315, 2015.

[14] W. Qian, H. Cha, F. Z. Peng, and L. M. Tolbert, "55-kw variable 3x dc-dc converter for plug-in hybrid electric vehicles," *IEEE Transactions on Power Electronics*, vol. 27, no. 4, pp. 1668–1678, 2012.

[15] G. P. Marcilio, J. ao José de Assis Rangel, C. L. M. de Souza, E. Shimoda, F. F. da Silva, and T. A. Peixoto, "Analysis of greenhouse gas emissions in the road freight transportation using simulation," *Journal of Cleaner Production*, vol. 170, pp. 298 – 309, 2018.

[16] "Co2 emissions from fuel combustion 2018." International Energy Agency (IEA), Tech. Rep., 2017.

[17] N. Shaukat, B. Khan, S. Ali, C. Mehmood, J. Khan, U. Farid, M. Majid, S. Anwar, M. Jawad, and Z. Ullah, "A survey on electric vehicle transportation within smart grid system," *Renewable and Sustainable Energy Reviews*, vol. 81, pp. 1329 – 1349, 2018.

[18] J. Y. Yong, V. K. Ramachandaramurthy, K. M. Tan, and N. Mithulananthan, "A review on the state-of-the-art technologies of electric vehicle, its impacts and prospects," *Renewable and Sustainable Energy Reviews*, vol. 49, pp. 365 – 385, 2015.

[19] X. Shi, J. Pan, H. Wang, and H. Cai, "Battery electric vehicles: What is the minimum range required?" *Energy*, vol. 166, pp. 352 – 358, 2019.

[20] A. M. Andwari, A. Pesiridis, S. Rajoo, R. Martinez-Botas, and V. Esfahanian, "A review of battery electric vehicle technology and readiness levels," *Renewable and Sustainable Energy Reviews*, vol. 78, pp. 414 – 430, 2017.

[21] M. Quraan, P. Tricoli, S. D'Arco, and L. Piegari, "Efficiency assessment of modular multilevel converters for battery electric vehicles," *IEEE Transactions on Power Electronics*, vol. 32, no. 3, pp. 2041–2051, March 2017.

[22] M. A. Hannan, M. M. Hoque, A. Hussain, Y. Yusof, and P. J. Ker, "State-of-the-art and energy management system of lithium-ion batteries in electric vehicle applications: Issues and recommendations," *IEEE Access*, vol. 6, pp. 19 362–19 378, 2018.

[23] A. Sewergin, A. H. Wienhausen, K. Oberdieck, and R. W. D. Doncker, "Modular bidirectional full-sic dc-dc converter for automotive applications," in *2017 IEEE 12th International Conference on Power Electronics and Drive Systems (PEDS)*, Dec 2017, pp. 277–281.

[24] S. Rothgang, T. Baumhofer, H. van Hoek, T. Lange, R. W. D. Doncker, and D. U. Sauer, "Modular battery design for reliable, flexible and multi-technology energy storage systems," *Applied Energy*, vol. 137, pp. 931 – 937, 2015.

[25] Z. Q. Zhu and D. Howe, "Electrical machines and drives for electric, hybrid, and fuel cell vehicles," *Proceedings of the IEEE*, vol. 95, no. 4, pp. 746–765, April 2007.

[26] Z. Yang, F. Shang, I. P. Brown, and M. Krishnamurthy, "Comparative study of interior permanent magnet, induction, and switched reluctance motor drives for ev and hev applications," *IEEE Transactions on Transportation Electrification*, vol. 1, no. 3, pp. 245–254, Oct 2015.

[27] M. Cheng, L. Sun, G. Buja, and L. Song, "Advanced electrical machines and machine-based systems for electric and hybrid vehicles," *Energies*, vol. 8, no. 9, pp. 9541–9564, 2015. [Online]. Available: http://www.mdpi.com/1996-1073/8/9/9541

[28] A. A. . Abdallh and M. Witters, "Optimal control and design of hybrid electric vehicles including bi-directional dc-dc converters," in *2017 IEEE Vehicle Power and Propulsion Conference (VPPC)*, Dec 2017, pp. 1–5.

[29] J. O. Estima and A. J. M. Cardoso, "Efficiency analysis of drive train topologies applied to electric/hybrid vehicles," *IEEE Transactions on Vehicular Technology*, vol. 61, no. 3, pp. 1021–1031, March 2012.

[30] Y. Zhang, H. Liu, J. Li, M. Sumner, and C. Xia, "A dc-dc boost converter with a wide input range and high voltage gain for fuel cell vehicles," *IEEE Transactions on Power Electronics*, 2018.

[31] Y. Zhang, Y. Gao, L. Zhou, and M. Sumner, "A switched-capacitor bidirectional dc-dc converter with wide voltage gain range for electric vehicles with hybrid energy sources," *IEEE Transactions on Power Electronics*, 2018.

[32] O. Hegazy, J. V. Mierlo, and P. Lataire, "Analysis, modeling, and implementation of a multidevice interleaved dc/dc converter for fuel cell hybrid electric vehicles," *IEEE Transactions on Power Electronics*, vol. 27, no. 11, pp. 4445–4458, Nov 2012.

[33] O. C. Onar, J. Kobayashi, D. C. Erb, and A. Khaligh, "A bidirectional high-power-quality grid interface with a novel bidirectional noninverted buck boost converter for phevs," *IEEE Transactions on Vehicular Technology*, vol. 61, no. 5, pp. 2018–2032, Jun 2012.

[34] A. K. Singh and M. K. Pathak, "Single-stage zeta-sepic-based multifunctional integrated converter for plug-in electric vehicles," *IET Electrical Systems in Transportation*, vol. 8, no. 2, pp. 101–111, 2018.

[35] C.-M. Lai, Y.-H. Cheng, M.-H. Hsieh, and Y.-C. Lin, "Development of a bidirectional dc/dc converter with dual-battery energy storage for hybrid electric vehicle system," *IEEE Transactions on Vehicular Technology*, vol. 67, no. 2, pp. 1036–1052, 2018.

[36] Y. Zhang, X.-F. Cheng, C. Yin, and S. Cheng, "A soft-switching bidirectional dc-dc converter for the battery super-capacitor hybrid energy storage system," *IEEE Transactions on Industrial Electronics*, 2018.

[37] K. J. Reddy and S. Natarajan, "Energy sources and multi-input dc-dc converters used in hybrid electric vehicle applications–a review," *International Journal of Hydrogen Energy*, 2018.

[38] E. Sanchis, E. Maset, A. Ferreres, J. B. Ejea, V. Esteve, J. Jordan, J. Calvente, A. Garrigos, and J. M. Blanes, "Bidirectional high-efficiency nonisolated step-up battery regulator," *IEEE Transactions on Aerospace and Electronic Systems*, vol. 47, no. 3, pp. 2230–2239, 2011.

[39] F. Mendez-Diaz, B. Pico, E. Vidal-Idiarte, J. Calvente, and R. Giral, "Hm/pwm seamless control of a bidirectional buck–boost converter for a photovoltaic application," *IEEE Transactions on Power Electronics*, vol. 34, no. 3, pp. 2887–2899, 2019.

[40] H. Ramírez-Murillo, C. Restrepo, J. Calvente, A. Romero, and R. Giral, "Energy management of a fuel-cell serial–parallel hybrid system," *IEEE Transactions on Industrial Electronics*, vol. 62, no. 8, pp. 5227–5235, 2015.

[41] C. Restrepo, J. Calvente, A. Romero, E. Vidal-Idiarte, and R. Giral, "Current-mode control of a coupled-inductor buck–boost dc–dc switching converter," *IEEE Transactions on Power Electronics*, vol. 27, no. 5, pp. 2536–2549, May 2012.

[42] C. Restrepo, T. Konjedic, J. Calvente, and R. Giral, "Hysteretic transition method for avoiding the dead-zone effect and subharmonics in a noninverting buck–boost converter," *IEEE Transactions on Power Electronics*, vol. 30, no. 6, pp. 3418–3430, 2015.

[43] C. Restrepo, T. Konjedic, F. Flores-Bahamonde, E. Vidal-Idiarte, J. Calvente, and R. Giral, "Multisampled digital average current controls of the versatile buck-boost converter," *IEEE Journal of Emerging and Selected Topics in Power Electronics*, 2018.

[44] F. Mendez-Diaz, H. Ramirez-Murillo, J. Calvente, B. Pico, and R. Giral, "Input voltage sliding mode control of the versatile buck-boost converter for photovoltaic applications," in *Industrial Technology (ICIT), 2015 IEEE International Conference on*. IEEE, 2015, pp. 1053–1058.

[45] A. M. Rahimi and A. Emadi, "An analytical investigation of dc/dc power electronic converters with constant power loads in vehicular power systems," *IEEE Transactions on vehicular technology*, vol. 58, no. 6, pp. 2689–2702, 2009.

[46] L. A. Tendillo, "Design and control of a bidirectional dc/dc converter for an electric vehicle application," *PhD thesis, URV*, 2015.

[47] H. Ramírez-Murillo, C. Restrepo, J. Calvente, A. Romero, and R. Giral, "Energy management dc system based on current-controlled buck-boost modules," *IEEE Transactions on Smart Grid*, vol. 5, no. 5, pp. 2644–2653, 2014.

[48] L. Kiraly, "Solving noise problems in high power, high frecuency control ic driven power stages," *International Rectifier Design Tips*.

[49] B.-S. Kim, H.-J. Kim, C. Jin, and D.-Y. Huh, "A digital controlled dc-dc converter for electric vehicle applications," in *Electrical Machines and Systems (ICEMS), 2011 International Conference on*. IEEE, 2011, pp. 1–5.

[50] R. Teodorescu, M. Liserre, and P. Rodriguez, *Grid converters for photovoltaic and wind power systems*. John Wiley & Sons, 2011, vol. 29.

[51] J. Calvente, H. Ramirez-Murillo, E. Vidal-Idiarte, R. Giral, and C. Restrepo, "Multisampled average current control of switching power converters," in *Industrial Technology (ICIT), 2015 IEEE International Conference on*. IEEE, 2015, pp. 2120–2124.

[52] E. Vidal-Idiarte, A. Marcos-Pastor, G. Garcia, A. Cid-Pastor, and L. Martinez-Salamero, "Discrete-time sliding-mode-based digital pulse width modulation control of a boost converter," *IET Power Electronics*, vol. 8, no. 5, pp. 708–714, 2015.

[53] E. Vidal-Idiarte, A. Marcos-Pastor, R. Giral, J. Calvente, and L. Martinez-Salamero, "Direct digital design of a sliding mode-based control of a pwm synchronous buck converter," *IET Power Electronics*, vol. 10, no. 13, pp. 1714–1720, 2017.

[54] C. Chan, Y. Wong, A. Bouscayrol, and K. Chen, "Powering sustainable mobility: roadmaps of electric, hybrid, and fuel cell vehicles [point of view]," *Proceedings of the IEEE*, vol. 97, no. 4, pp. 603–607, 2009.

[55] O. P. Jaga, S. K. Maurya *et al.*, "Modeling and control strategies for energy management system in electric vehicles," *Perspectives in Science*, vol. 8, pp. 358–360, 2016.

[56] B. Sakhdari and N. Azad, "An optimal energy management system for battery electric vehicles," *IFAC-PapersOnLine*, vol. 48, no. 15, pp. 86–92, 2015.

[57] M. A. Silva, H. N. de Melo, J. P. Trovao, P. G. Pereirinha, and H. M. Jorge, "Hybrid topologies comparison for electric vehicles with multiple energy storage systems," in *Electric Vehicle Symposium and Exhibition (EVS27), 2013 World*. IEEE, 2013, pp. 1–8.

[58] O. Hegazy, R. Barrero, J. Van Mierlo, P. Lataire, N. Omar, and T. Coosemans, "An advanced power electronics interface for electric vehicles applications," *IEEE transactions on power electronics*, vol. 28, no. 12, pp. 5508–5521, 2013.

[59] M. Thorne and M. Kazerani, "A regenerative controllable dc load for an electric vehicle test station," in *Industrial Electronics, 2009. IECON'09. 35th Annual Conference of IEEE*. IEEE, 2009, pp. 3773–3778.

[60] S. Mohon, A. Venkitakrishnan, B. Ayalew, and P. Pisu, "Development of an electric vehicle hardware-in-the-loop emulation platform," in *ASME 2013 International Design Engineering Technical Conferences and Computers and Information in Engineering Conference*. American Society of Mechanical Engineers, 2013, pp. V001T01A002–V001T01A002.

[61] C. Lin and L. Zhang, "Hardware-in-the-loop simulation and its application in electric vehicle development," in *Vehicle Power and Propulsion Conference, 2008. VPPC'08. IEEE*. IEEE, 2008, pp. 1–6.

[62] B. Hayes, "Nonlinear dynamics of dc-dc converters," Ph.D. dissertation, Dublin City University, 2016.

[63] L. Corradini and P. Mattavelli, "Modeling of multisampled pulse width modulators for digitally controlled dc–dc converters," *IEEE Transactions on Power Electronics*, vol. 23, no. 4, pp. 1839–1847, 2008.

[64] H. Peng, A. Prodic, E. Alarcón, and D. Maksimovic, "Modeling of quantization effects in digitally controlled dc–dc converters," *IEEE Transactions on power electronics*, vol. 22, no. 1, pp. 208–215, 2007.

[65] A. V. Peterchev and S. R. Sanders, "Quantization resolution and limit cycling in digitally controlled pwm converters," *IEEE Transactions on Power Electronics*, vol. 18, no. 1, pp. 301–308, 2003.

[66] Z. Zhao and A. Prodic, "Non-zero error method for improving output voltage regulation of low-resolution digital controllers for smps," in *2008 Twenty-Third Annual IEEE Applied Power Electronics Conference and Exposition*. IEEE, 2008, pp. 1106–1110.

[67] A. E. Syed and A. Patra, "Saturation generated oscillations in voltage-mode digital control of dc–dc converters," *IEEE Transactions on Power Electronics*, vol. 31, no. 6, pp. 4549–4564, 2016.

[68] ——, "Dynamic adc-quantization for oscillation-free performance of digitally controlled converters," in *2017 IEEE International Symposium on Circuits and Systems (ISCAS)*. IEEE, 2017, pp. 1–4.

[69] W. Stefanutti, E. D. Monica, E. Tedeschi, P. Mattavelli, and S. Saggini, "Reduction of quantization effects in digitally controlled dc-dc converters using inductor current estimation," in *Proc. IEEE PESC*, 2006, pp. 1–7.

[70] S. Chattopadhyay, "Analysis of limit cycle oscillations in digital current-mode control," in *Twenty-First Annual IEEE Applied Power Electronics Conference and Exposition, 2006. APEC'06.* IEEE, 2006, pp. 7–pp.

[71] S. Kapat, "Selectively sampled subharmonic-free digital current mode control using direct duty control," *IEEE Transactions on Circuits and Systems II: Express Briefs*, vol. 62, no. 3, pp. 311–315, 2015.

[72] G. Sajitha and T. Kurian, "Reduction in limit cycle oscillation and conducted electromagnetic emissions by switching frequency adjustment in digitally controlled dc-dc converters," *EPE JOURNAL*, vol. 26, no. 3, pp. 96–103, 2016.

[73] L. Corradini, W. Stefanutti, and P. Mattavelli, "Analysis of multisampled current control for active filters," *IEEE Transactions on Industry Applications*, vol. 44, no. 6, pp. 1785–1794, 2008.

[74] L. Corradini, D. Maksimovic, P. Mattavelli, and R. Zane, *Digital control of high-frequency switched-mode power converters*. John Wiley & Sons, 2015, vol. 48.